INFORMATION TO USERS

The negative microfilm of this dissertation was prepared and inspected by the school granting the degree. We are using this film without further inspection or change. If there are any questions about the content, please write directly to the school. The quality of this reproduction is heavily dependent upon the quality of the original material

The following explanation of techniques is provided to help clarify notations which may appear on this reproduction.

1. Manuscripts may not always be complete. When it is not possible to obtain missing pages, a note appears to indicate this.

2. When copyrighted materials are removed from the manuscript, a note appears to indicate this.

3. Oversize materials (maps, drawings, and charts) are photographed by sectioning the original, beginning at the upper left hand corner and continuing from left to right in equal sections with small overlaps.

UMI Dissertation
Information Service

A Bell & Howell Information Company
300 N. Zeeb Road, Ann Arbor, Michigan 48106

DETAILED INVESTIGATION OF SPACECRAFT GLOW

A Dissertation

Presented to the Faculty of the Graduate School

of Cornell University

in Partial Fulfillment of the Requirements for the Degree of

Doctor of Philosophy

by

Daniel Paul Karipides

May 1999

Biographical Sketch

The author grew up in a small town in southern Ohio and was very happy that the town did not grow up around him. He discovered the wonders of life under a mantle of love from two very dedicated parents and at the side of an older brother. Should the details of the exploits of these two brothers ever become widely known, there would be, without doubt, no end to the amazement that they managed to survive them relatively unscathed. For a short while, the Karipides family was joined by a happy-go-luck beagle name PT. During this time, the origin of the the term "man's best friend" became apparent to the author.

At a very young age, he found himself fascinated with all things fantastic, be it the detailed interworkings of an intergalatic navy or the chivalric code of white knights and the fire-breathing dragons that oppose them. Countless hours of playing catch in the backyard with his father while listening to the sounds of Cincinnati Reds cemented the foundations of a love of the game of baseball. A brief desire to become a writer led him to dictate a short, yet complete, mystery novel to his aforementioned dedicated mother. Her patience and support during this experience showed him that as well as being a parent, she was also a good friend. The author is happy that this continues to be true throughout his life. Also at a young age, he began to suspect that nice guys finish last. Lacking the experience to know if his

suspicions were correct, the author decided that further investigation was warranted.

High school came and did not leave soon enough. If awkward experiences and feelings are typical of young people of this age, then the author was extremely typical. It was also during this time that the author became convinced that nice guys do, indeed, finish last. Nevertheless, some lasting friendships were made during this time and for that the author is eternally grateful. The end of the high school experience culminated with a trip to the then crumbling Soviet Union. This adventure remains the author's singular voyage overseas and proved to be an amazing experience. Also present on the trip was a life-long friend, with whom numerous Thanksgivings and summer jobs had already been shared. It was during this trip that he realized that the mutual bond between these two would with certainty outlast distance, time and any other other barriers.

Showing his adventurous spirit, the author chose to attend Miami University in Oxford, Ohio and traveled at least a couple of miles to find his freshman dorm. As no surprise to friends and family, physics was chosen a focus for his undergraduate work. Determined to shake the mantle of nerd, or even worse appellations, he quickly joined a martial arts club. While the possibility of starring in the latest action movie remains astronomically low, the author considers the attainment of his black belt to be one of his most significant achievements to date. Two years were spent in chaos of college dormitories. In an effort to regain his sanity, a single apartment was found for the remaining two years. Some very special friends were discovered during these years and the author is thankful for laughter that was given and shared. The author also spent a significant portion of time gathering evidence concerning the failed efforts of nice guys and finish lines.

An interest in aerospace was evident from an early age—the author's mother would like it noted that his first word was "airplane". This interest led him to the Finger Lakes of central New York and Cornell University. Two events early in his time there shaped his future and his outlook. On a very snowy spring day, the likes of which are all too common in the area, the author managed to spin his car out of control, thereby presenting the driver's side door to an ominous, eighteen-wheeled, loaded-to-the-brim logging truck. Under the protection of what surely must have been divine fortune, he survived the incident with a remarkably low number of injuries. His time at Cornell was also marked by the loss of his father. The author cannot convey the profound effect this has had on him, and only wishes to say that he hopes that no one ever be forced to undergo such an experience at such a young age. Both of these events left him with the unshakeable desire to live each day to its fullest and this is the attitude that the author takes with him as he moves forward into the next stage of his grand adventure. The author notes that the benefits of this approach may already be apparent. In his final year at Cornell, he had the good fortune of meeting a wondrously special soul, who, through much cajoling and convincing, has the author thinking that maybe nice guys can, indeed, finish first.

"Dr. Karipides?"

"Yes?"

"This is Dr. Karipides..."

More than anything in this world, I am my father's son.

Acknowledgements

The funding for the work presented in this dissertation was provided by Ballistic Missile Defense Organization under AASERT award DAAH04-95-1-0204. Computational resources were provided on an IBM SP-2 at the Cornell Theory Center.

I would to thank the following people for the support they have provided during my investigation of the welkin.

I would especially like to acknowledge my advisor Iain Boyd, for his guidance and advice over the past six years. Specifically I would like to thank him for being a daily example of dedicated, talented researcher.

Additional recognition is given to my special committee members David Caughey and Paul Kintner. Also, P.C.T. de Boer is thanked for serving as a proxy for David when needed.

A tip of the hat is given to my former officemates, namely Shankar, Tom, Walt and Wyatt for a multitude of classic conversations and memories.

Special thanks to the current cast and crew in 139 Upson. To Doug, for classic observations and debates over the failings of the English language and for generally being a good friend. To Jitendra, for assuring that I wasn't the craziest person in the office. To Bill, for immediately accepting and joining the insanity as well as reminding me of the wonders of self-deprecating humor. To Elizabeth, for enlivening

the office with genuine laughter and some really, really silly jokes.

To Mike, for being a good sport and a willing participant in the madness.

To Jamal, Cyril, Manish and many others, for speaking their minds and showing me different points of view.

Thanks are given to the many amazing people that I have had the pleasure of meeting high above Cayuga's waters:

To Carol, for leading me to Cornell in the first place.

To Sharon, for being my surrogate mother when I needed it the most, which was often. For introducing me to the wonders of snowmobiling. And, most of all, for welcoming me as part of your family. Thanks Sharon, Ed, Tiffany and Mike.

To Tobe, for listening without judging and giving honest advice.

To Cris, Annie, Chris, Amy, Robert, and all those involved in the graduate student assembly.

Special thanks are given to some very unique people that mean far more to me than they know:

To Andy, for sharing the vision of worlds unvisited and places unseen.

To Evelyn, for surprising me by inviting me to her birthday party and for the years of friendship since then.

To Brian, for being a partner in crime and all around good person.

To Dana, who gave me the most precious of gifts–the gift of laughter. Thank you, Dana, for everything.

To Tammy, for being my willing cooking guinea pig.

To Aislynn, for being a welcome voice in the night.

To Colleen, for sharing both friendship and forgiveness.

To Keith, for so many things, too numerous to list. To steal a line from one of the greatest shows of all time, "Thanks, Keith, you made it bearable."

To Jennifer, for allowing me the honor of considering you my sister. For countless hours of listening when there was no one else to listen. For the genuine excitement and desire you show in sharing the adventures of your life with me. For, quite simply, defining friendship, now and forever.

To Dave, for being an ideal brother. For blades, for rocket-powered, frog-piloted Tonka trucks, for TV's turned into bug zappers, for exploding army men, for water-powered bottle rockets, and for a thousand other adventures. For living your life in a way that would make Dad proud.

To Mom, who has dedicated her life to being a wonderful mother, a debt I cannot even being to repay. The knowledge that I have your love and support unconditionally gives me strength to undertake any challenge. For being my friend above all else.

And to Tammie. Words cannot do my feelings justice, yet I feel compelled to try. Thank you for your unconditional love and support. For sharing with me a piece of your truly wondrous and loving soul. For letting me be a white knight. You fire for life, your passion, your hopes and dreams, your laughter, your love—they all mean more to me than you can possible realize. Thank you Tams.

Table of Contents

List of Tables

List of Figures

List of Symbols

N	Number of species
X	Free surface site
A_i	Species i $(1 \leq i \leq \mathrm{N})$
$\vec{A}$	Species A moving towards the surface
$\overleftarrow{A}$	Species A moving away the surface
A^a	Species A adsorbed on the surface
n_i	Surface number density of species i
n_s	Surface number density of surface sites
Θ_i	Surface coverage of species i $(\Theta_i \equiv n_i/n_s)$
F_i	Flux of species i to the surface, [particles/$(m^2 s)$]
S_i	Sticking coefficient for species i
τ_i	Thermal desorption time for species i, $[s]$
σ_{ij}^d	Desorption cross-section for species i and j, $[m^2]$
σ_{ij}^{er}	Eley-Rideal cross-section for species i and j, $[m^2]$
ϵ_{ij}^{er}	Probability of ejection after Eley-Rideal reaction
K_{ij}^{lh}	Langmuir-Hinshelwood reaction rate for species i and j, $[m^2/\text{particles}]$
ϵ_{ij}^{lh}	Probability of ejection after Langmuir-Hinshelwood reaction
Q	Species of interest

Chapter 1

Introduction

1.1 Spacecraft Glow

Ram surfaces in low earth orbit are known to exhibit a visible orange-red luminescence, which is known as spacecraft glow. Such glows have been observed around satellites[1], around the space shuttle[2], and in laboratory experiments reproducing low earth orbit conditions[3]. A large number of investigations have been performed to understand the interaction of a spacecraft with the ambient atmosphere and these are reviewed by Murad[4]. The present work focuses on glow production in the altitude range of 140 km to 300 km. A preponderance of the available glow data have been taken in this altitude range.

One fundamental characteristic of spacecraft glow is a variation of glow brightness with altitude. Original investigations of spacecraft glow suggest a variety of mechanisms for glow production[1, 5, 6]. Many of the models described in these investigations attempt to correlate the brightness variations to density variations of common atmospheric species. Specifically, the densities of molecular nitrogen and

atomic oxygen are targeted. This is a logical first approach, as these two species are the dominant species in the altitude range of interest.

There are difficulties in applying such simple models. Atmospheric species exhibit an exponential decrease of density with altitude, with the rate of decrease depending on the molecular weight of the gas. In the target altitude range, there is not a sufficient number of collisions to allow for mixing, so in essence the atmosphere is a collection of separate single-species gases. Consequently, each species has a separate rate of decrease based on its molecular weight. Experimental measurements of spacecraft glow do not have such a simple variation with altitude. In particular, at an altitude of approximately 165 km, the rate of decrease changes abruptly[1]. Therefore, glow brightness cannot correlate exactly with one species throughout the entire altitude range of interest. This is a strong indication that the production of spacecraft glow is a complex phenomenon. Later models correlate the brightness variations to different species at different altitudes[5].

Examination of the measured spectrum of spacecraft glow is consistent with the spontaneous emission of electrically excited nitrogen dioxide[3]. Nitrogen dioxide does not exist in quantity in the atmosphere[7], indicating that it must be produced chemically at some point in the glow production mechanism. The measured spectrum was red-shifted in comparison with the spectrum of gaseous nitrogen dioxide, NO_2^*[2]. This is expected of the emission spectra of molecules created chemically with surface catalysis. Thus, it is expected that the nitrogen dioxide is created on the ram surface itself.

1.2 Motivation and Goals

There are a variety of reasons why an understanding of the glow production mechanisms is beneficial. These benefits serve as a motivation for the work presented here. A statement defining the primary goal of the work is also included.

Experiments relying on optical measurements can experience interference from glow created in front of the ram surfaces of the space vehicle carrying the experimental apparatus[8]. Detailed knowledge of the mechanisms leading to spacecraft glow can allow for experiments to be designed to avoid this interference. Alternatively, the predicted glow spectrum could be subtracted from the experimental measurements.

The production of glow by ram surfaces provides a known signature that can be used by detection schemes. The ram surface created by the tip of a missile would produce a glow signature that is separate and distinct from radiation emitted during re-entry. Along with an understanding of the shock created from rocket exhaust-atmosphere interactions, spacecraft glow is a likely candidate for the basis of systems designed to counter ballistic missiles.

Finally, the nature of glow measurements indicate that the production method is a complex one. Investigation of glow production requires an understanding of atmospheric structure, of rarefied, non-equilibrium aerothermochemistry, of molecular surface chemistry, as well as many other areas of scientific interest. It is hoped that the study of glow will help to contribute to a better understanding of these areas. Thus, the detailed simulation and study of spacecraft glow is attractive from a purely scientific standpoint.

The primary goal of this work is to simulate in detail the processes leading to the

production of spacecraft glow. This includes maintaining a level of understanding at the microscopic level from the initial disturbance of the ambient atmosphere by the ram surface to the actual emission of the glow luminescence. Particular attention is given to the identification of the primary reactions leading to glow production, to the important precursor reactions, and to the importance of rare species in the ambient atmosphere. It is a further goal to analyze the results from the simulations and validate them against both theoretical analyses and experimental measurements.

1.3 Overview of the Solution Procedure

A three step procedure is used to investigate computationally the spacecraft glow phenomenon. Each step is relatively self-contained, with results from the previous step providing the input conditions for the next. The processes simulated by each step are themselves largely independent of one another. Thus, a non-unified solution procedure is valid. Instances where a unified procedure would give a theoretical improvement in accuracy will be identified as the procedure is outlined in subsequent chapters. In most, if not all, of these instances, the actual gain in accuracy would be negligible. The structure of the solution procedure is illustrated in Figure 1.1.

The first step involves a simulation of the flow field around the spacecraft exhibiting the glow. Low earth orbit conditions are highly rarefied. Under such low densities, the continuum hypothesis breaks down and the traditional fluid dynamics equations cannot be applied. A well developed particle method, the direct simulation Monte Carlo (DSMC) method[9], is used to simulate the flow field. This method is ideal for simulating the non-equilibrium effects that are common in rarefied flow fields. There exists an inherent difficulty in simulating trace species with the DSMC

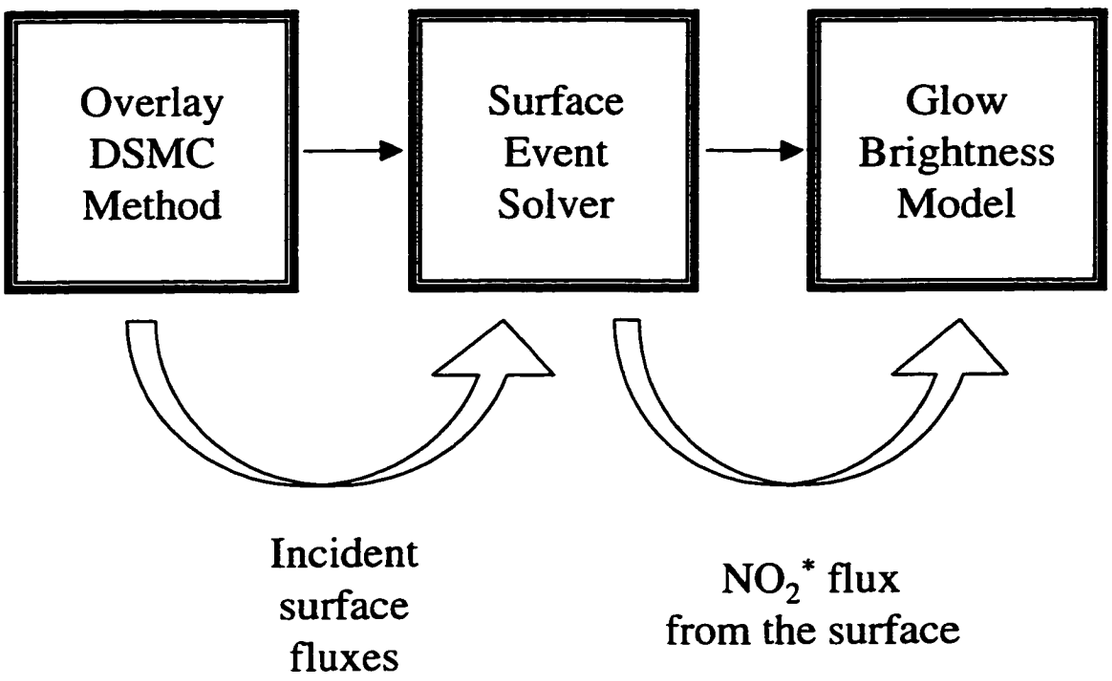

Figure 1.1. A Three Step Solution Procedure

method[10]. A modification is developed to enable all of the important species to be simulated with acceptable accuracy. The DSMC method enables a large number of both macroscopic and microscopic behaviors of the flow field to be calculated. These quantities are studied to gain insight into the nature of glow-producing flow fields. Most important to the solution procedure, however, is the calculation of the incident fluxes of the different chemical species to the ram surface.

The incident fluxes from the DSMC computation are used as input to the second step of the solution procedure–a detailed simulation of the surface-catalyzed events. Simulated phenomena include both non-reacting events and chemical reactions. Each event is modeled in differential form and the resulting set of equations is solved using a standard numerical approach. The set of events included is capable of

representing complex, realistic, and interdependent behavior of surface phenomena. It should be noted that the parameters controlling many of the events are not well known through experimental or analytical means. Thus, a strong variability of values from independent sources for the controlling parameters is expected. Solution of the set of equations gives time-accurate surface concentrations of each species. Furthermore, the rate at which electrically excited nitrogen dioxide is emitted into the flow field is also calculated.

As a final step, the actual glow brightness is calculated. A straightforward model is used to relate the emitted nitrogen dioxide flux to the glow brightness. While limited in scope, this model is sufficient to give calculated values of glow brightness that can be compared with experimental measurements. In addition, several simplifying assumptions are made to facilitate the conversion. A much more sophisticated model could be used to remove some of the assumptions, but is left for future consideration.

1.4 Dissertation Structure

The structure of this dissertation is as follows. Chapter 1 provides an introduction to spacecraft glow, a discussion of the motivations and goals of the work, an overview of the solution method used, and this description of the structure of the document. A more in depth look at the glow phenomenon is given in Chapter 2. Attention is paid to the Atmosphere Explorer satellite and the Space Shuttle–the two vehicles from which experimental measurements are later used for comparison with the simulated values. Chapter 3 describes the DSMC method and illuminates some common resolution difficulties. A detailed description of the DSMC method

is beyond the scope of the dissertation. Many detailed treatments are available in the quoted citations. A key resolution issue is the inherent difficulty of the DSMC method to track rare particles. Solutions that overcome this problem are discussed in Chapter 4. Specifically, overlay methods are explained, with a focus on the DSMC overlay technique. The surface event modeling is presented in Chapter 5. A steady state analysis of the resulting system of equations is included. Chapter 6 contains discussions of the determination of the many input parameters required by the solution procedure. Computational costs are summarized. Additionally, a summary of the uncertainties and assumptions is included. Selected results are given in Chapters 7–9. Flow field results are presented in Chapter 7. Both macroscopic and microscopic details of the flow are examined. Chapter 8 presents surface coverage results. A focus is given to the time-varying behavior. A comparison of the analytical steady-state analysis is included. Chapter 9 presents glow brightness results. The sensitivity of the brightness to some of the input parameters is examined. Temporal variations in glow production are shown. Comparisons with experimental data are presented and discussed. Conclusions and ideas for future work are given in Chapter 10. The chapter ends with some final thoughts on the present work.

Chapter 2

The Glow Phenomenon

Spacecraft glow has been observed on a variety of different vehicles. Two of the best sources of glow measurements are flights of the Atmosphere Explorer satellites[1, 5] and the space shuttle[11, 12]. Details of the experiments that measured the glow are given in this chapter. An additional section contains an overview of the nature of the flow fields relevant to glow production.

2.1 Atmosphere Explorer Glow

This section briefly describes the Atmosphere Explorer (AE) satellites[13, 14]; both historical and physical details are included. Of the many on-board experiments carried by the AE satellites, the relevant ones are described and referenced. Finally, a discussion of the nature of AE glow measurements is included.

2.1.1 The Atmosphere Explorer Satellite

To provide a source for comparison of the numerical predictions, data are taken from flights of the Atmosphere Explorer satellite. A number of vehicles have flown under the Atmosphere Explorer program and it is important to identify from which vehicles and missions data are taken. The Atmosphere Explorers A and B were launched in the early and middle 1960's. While a wealth of useful data concerning the general atmospheric phenomena was obtained during these flights, direct measurements of glow were not taken. As a result, they are not under consideration here. The three successive flights (C, D and E) of the Atmosphere Explorer had a different geometry and carried different instruments. Of these, the lifetime of the D mission was drastically shortened due to a failure of the power system. Therefore, the C and E flights serve as the sources for data.

For the later missions, the satellite body is approximately a cylinder of radius 0.7 m and length 1.0 m. The AE satellite typically flew spin stabilized with the axis of spin perpendicular to the velocity vector. It also flew in a despun mode for particular orbits. Orbits were either circular or elliptical. The elliptical orbits allowed the satellite to pass through a wide range of altitude and thus to experience a variety of atmospheric conditions. Apogee for these orbits was about 4000 km, and perigee was approximately 150 km. Occasionally, excursions down to altitudes as low as 135 km were performed. The depth of the penetration was limited by thermal heating due to the increased atmospheric density. Figure 2.1 (taken from Ref. [13], page 49) shows a typical orbit with a perigee in the lower thermosphere and gives an indication of the time taken to change altitudes.

The spin stabilization has a dramatic effect on the overall behavior of surface

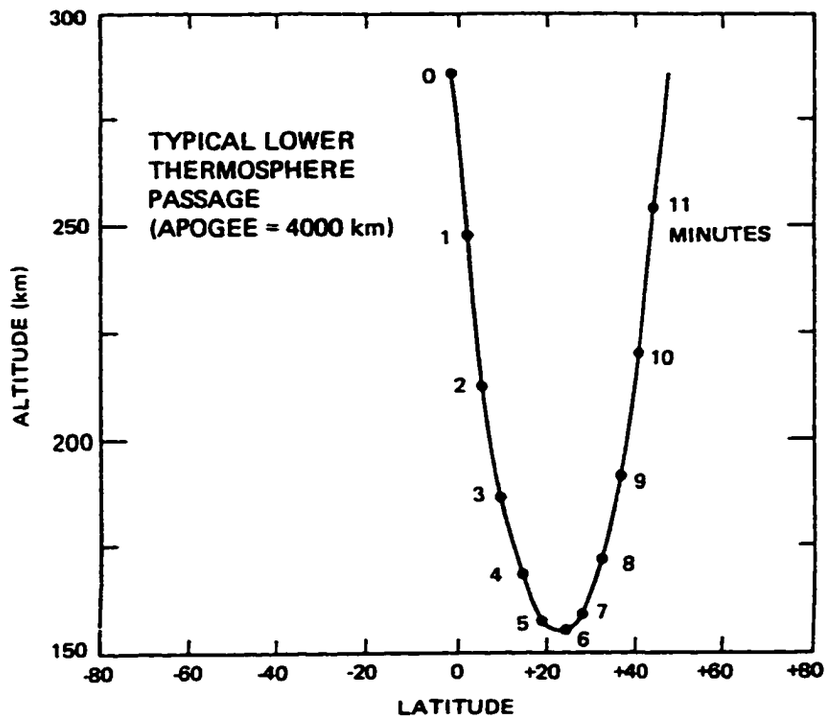

Figure 2.1. Typical Elliptical Orbit

phenomenon as well as experimental measurements. The period of the spin was 15 s. The surfaces of the satellite, and thus the scientific instruments carried on-board, experience a cyclic variation in the magnitude of the incident flux of particles. This is illustrated in Figure 2.2. Many of the measurements and calculations considered here focus on the forward-looking glow values; that is, when the normal of the surface through which the instrument looks is parallel with the velocity vector. Note that for almost half of the rotational period, a particular instrument is in the shadow of the satellite body. This causes a significant variation in the environment experienced by an individual surface during one revolution of the satellite.

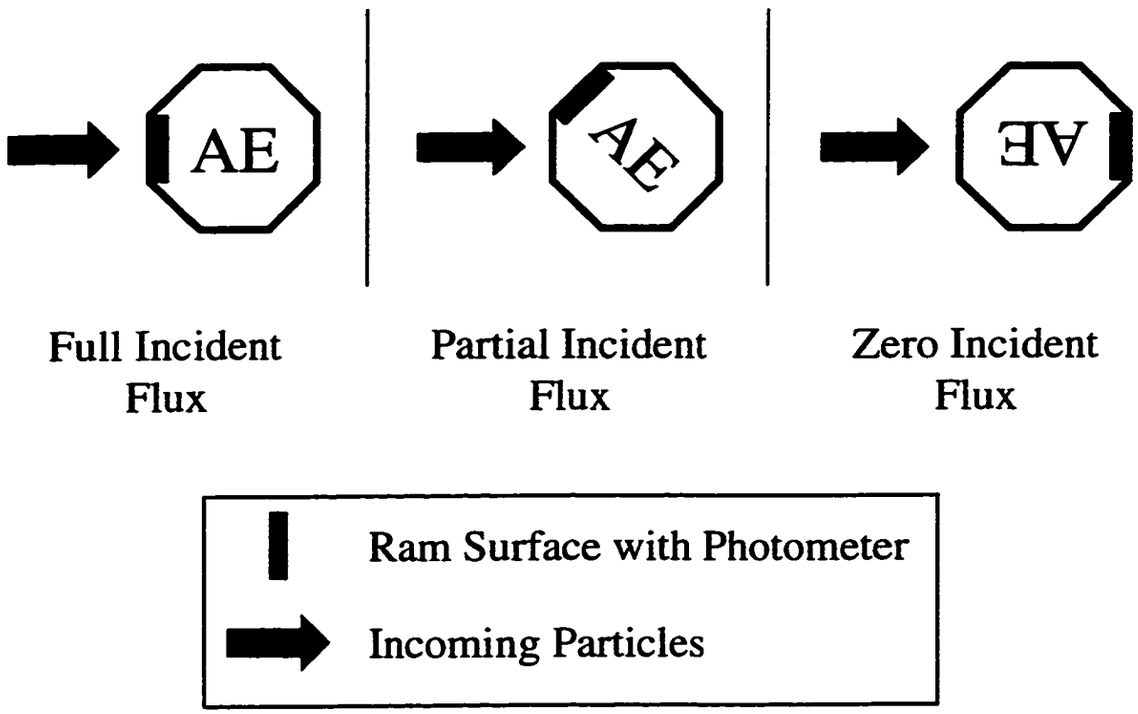

Figure 2.2. Importance of Satellite Rotation on Incident Flux

2.1.2 On-Board Experiments

While a wide variety of instruments were carried on board, two experiments are of particular interest here. The first of these is the Visible Airglow Experiment (VAE)[15]. This experiment used filter photometers to monitor emmisions in the range 280.0 nm to 732.0 nm. This range was chosen so that airglow[16] and auroral emissions could be studied. The wavelengths considered cover the spectra of electrically excited nitrogen dioxide. From analysis of shuttle and laboratory measurements, the spectrum of NO_2^* is considered the source for spacecraft glow[2]. Thus, fortuitously, the photometers captured the spacecraft glow emissions as well. Measurements of glow were recorded for several wavelengths. This report focuses on glow measurements at 656.3 nm and 732.0 nm for the altitude range of 140–

300 km. Only the forward-looking glow values are considered here. These particular wavelengths and direction were chosen to match the availability of experimental measurements at these conditions. It is difficult to discern the spacecraft glow from other atmospheric emissions at the other wavelenghts measured by the VAE. Thus data for these other wavelengths do not serve as as a good basis for comparison for calculated glow brightness. In this range, the magnitude of the glow varies from $\mathcal{O}(100)$ to $\mathcal{O}(1)$ Rayleighs.

The second AE experiment of interest is the Neutral Atmosphere Composition Experiment (NACE)[17]. This experiment measured the ambient concentration of several air species, including nitric oxide. The actual experiment involved several instruments, including an open-source and a closed-source neutral mass spectrometer. In general, the open-source instrument is better at detecting reactive species, but is limited to strict forward-looking measurements[18]. The closed-source instrument can take measurements over the entire forward-looking hemisphere. Measurement of nitric oxide concentration is important, because its value varies greatly in the Earth's atmosphere and therefore the prediction of the ambient concentration of NO using analytical models is difficult. Indeed, the density values recorded by the NACE show a large scatter at each of the altitudes of interest. This variation provides lower and upper bounds for the NO concentrations which are used as an input condition for the simulations.

2.1.3 Characteristics of AE Glow

A well known feature of these data is a change in the slope of the glow brightness at an altitude of about 165 km[1]. Given that atmospheric species densities exhibit

a log-linear variation with altitude, the non-linear nature of glow data is evidence of a more complicated production mechanism. This bend has been attributed to the importance of gas-gas chemical reactions at the lower, more dense altitudes[10]. At these lower altitudes, a substantial accumulation of particles occurs in front of the ram surface. Furthermore, chemical reactions in the weak shock create elevated numbers of molecules critical to glow precursor reactions. Combined, these two effects cause a relatively greater increase in glow production at the lower altitudes.

Excluding apogee and perigee, the AE satellite passes through a particular altitude twice during an elliptical orbit–once while descending and once while ascending. The portion of the orbit where altitude is decreasing is termed the downleg, the opposite portion is the upleg. Differences are seen in glow brightness measurements for the same altitude between the upleg and the downleg[19, 20]. There are a number of possible factors that could explain this difference. A primary consideration is the effects of the cloud of accumulated particles in front of the ram surface. These particles are trapped before the body of the satellite, allowing some of the denser gases of the lower atmosphere to be dragged to higher altitudes during the upleg. This increased density could account for the higher upleg brightness measurements. Another possibility is that the difference in glow is due to the effects of the lifetime of surface adsorbed particles. These particles, adsorbed in the lower altitudes, could affect glow production during the upleg.

Similar to the upleg-downleg differences, a difference in glow brightness is also seen depending on the rotational direction of the satellite spin[21]. The difference is observed in measurements taken perpendicular to the velocity vector. Brightness is found to be greater when the ram surface housing the photometer rotates a quarter-

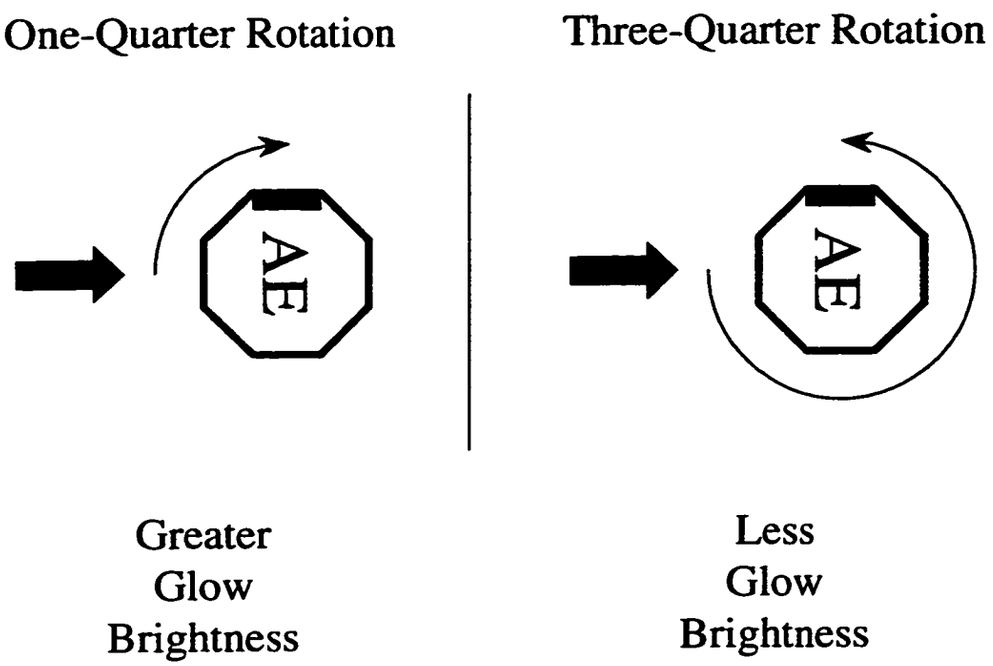

Figure 2.3. Variation of Brightness with Spin Direction

turn away from the velocity vector as compared to a three-quarter rotation. This is illustrated in Figure 2.3. Again, the lifetime of adsorbed molecules is the most likely explanation for the difference.

2.2 Space Shuttle Glow

Flights of the space shuttle provide an additional source of glow data. Indeed, shuttle glow is the most well-known example of spacecraft glow. An overview of shuttle glow measurements is given here, with an emphasis on the differences observed when compared to Atmosphere Explorer glow data.

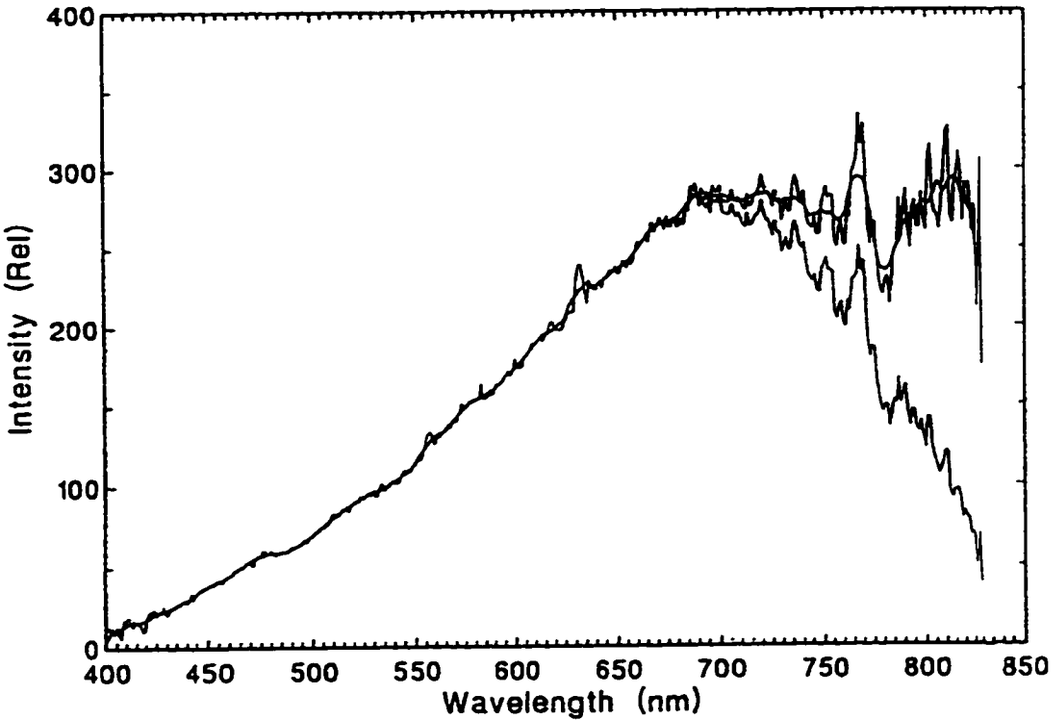

Figure 2.4. Measured Space Shuttle Glow Spectrum

2.2.1 Characteristics of Shuttle Glow

From the first flights of a space shuttle, astronauts observed a distinct orange halo from the leading edges of the shuttle. A spectrum of the now familiar glow was obtained during space transportation system flight 3 (STS-3), shown in Figure 2.4, which was taken from Ref. [22]. The upper curve represents the correctly calibrated and interpreted spectrum. The lower curve represents the spectrum before calibration. Since then, shuttle glow has received a large amount of attention. Measurements taken during flight STS-62 are specifically targeted in this work[12].

The spectrum of shuttle glow is consistent with the spectrum of NO_2^*[2]. It is suggested that the nitrogen dioxide is created via collisions of gaseous atomic oxygen with surface adsorbed nitric oxide. As with AE glow, a variation of glow intensity

with altitude is observed. It is important to note that shuttle glow measurements are taken at altitudes greater than 165 km. Therefore, the bend in glow brightness cannot be observed as with AE glow. Furthermore, shuttle glow is often cataloged through comparison of relative intensities. Thus, a quantitative comparison against simulation predictions is not possible.

The behavior of shuttle glow under a variety of conditions has been studied. Particular attention has been given to the variation of glow intensity with ram angle[11, 23]. The intensity varies with the cosine of the ram angle, which is expected from a simple consideration of the effect on the effective incident flux. As a result, simulating shuttle glow with a varying ram angle does not provide a useful test of the simulation method. The dependence of glow intensity on surface temperature has been used to estimate an activation energy for the glow phenomenon[24]. Detailed simulation of the effects of surface temperature is beyond the scope of the work presented here.

2.2.2 Extinction of Glow

Another specific behavior of shuttle glow is of interest. It has been observed that the release of nitrogen gas upstream of the ram surface results in a virtual extinction of shuttle glow[25, 12]. One suggestion for this effect is the shielding potential of the N_2 plume in which a field of increased density results in more collisions with free-stream molecules and therefore a reduction in the incident flux. It should be noted that the firing of a control thruster resulted in an increase in glow intensity as opposed to a reduction[12]. The exhaust plume of this thruster is primarily molecular nitrogen. In this case, a significant fraction of the N_2 released from the

thruster has high internal energy. This nitrogen is more likely to undergo chemical reactions via collisions with ambient molecules. These reactions lead to increased production of species critical to glow precursor reactions.

2.3 Skipper Flight Experiment

In addition to the Atmosphere Explorer satellites and the Space Shuttle, there are other flight experiments that are relevant to a study of the glow phenomenon. The Skipper Flight Experiment[26] is one such example vehicle designed in part to investigate spacecraft glow. The flight of the Skipper spacecraft was a continuation of early flight experiments known as the Bow Shock Ultraviolet (BSUV) flights. The first of these, BSUV-1, operated at a velocity of about 3.5 km/s and covered an altitude range of 40 km to 70 km[27]. The second flight, BSUV-2, operated at a velocity of 5.1 km/s over the altitude range of 65 km to 100 km[28]. During the flights of these vehicles, radiation measurements were taken of several atmospheric species, including NO, N and OH. Data from these missions has served as a useful source for calibration and validation of existing air radiation models[29]. Simulation of the flow fields around the BSUV vehicles requires the ability to track trace species. This ability is a focus of the present work.

The Skipper flight is, in essence, the third BSUV flight, although the scope of the mission is somewhat larger than the first two flights. The mission is composed of two distinct stages. The first stage consists of a number of elliptical, low-earth orbits during which spacecraft glow measurements are taken. In the second stage, the satellite takes radiation measurements during reentry. Specifically, radiation due to NO and O is targeted. Unlike the Atmosphere Explorer satellites, a full

spectrophotometer is carried on-board. This allows complete spectra to be measured as opposed to the intensity at a few discrete bands.

Unfortunately, mechanical complications resulted in a complete failure of the Skipper mission; no data was recorded by the satellite. The lack of data from the mission represents a substantial loss. Data from the missions would have provided a wealth of information relating to air radiation in general and spacecraft glow in particular.

2.4 Laboratory Investigations

A discussion of the glow phenomenon is not complete without a treatment of ground-based laboratory investigations of glow[3, 30, 31, 32, 33, 34]. Although a variety of experiments has been performed, most have focused on the reaction of fast atomic oxygen with surface adsorbed nitric oxide. This focus is due primarily to the fact that atomic oxygen is the dominant atmospheric species in the altitude range where Atmosphere Explorer and shuttle glow is observed. As with some of the shuttle glow experiments, the details of these laboratory investigations are not directly relevant to this work. However, one of the primary conclusions from these investigations is very relevant. The reaction of O with adsorbed NO leads to the production of NO_2^* and the familiar orange-red glow. An example laboratory-based spectrum is given in Figure 2.5, taken from Ref. [3]. The solid line corresponds to measurements taken near the sample; the dashed line represents data taken several centimeters from the sample. Thus, these experiments serve to verify independently that spacecraft glow is most likely due to the spectrum of excited nitrogen dioxide.

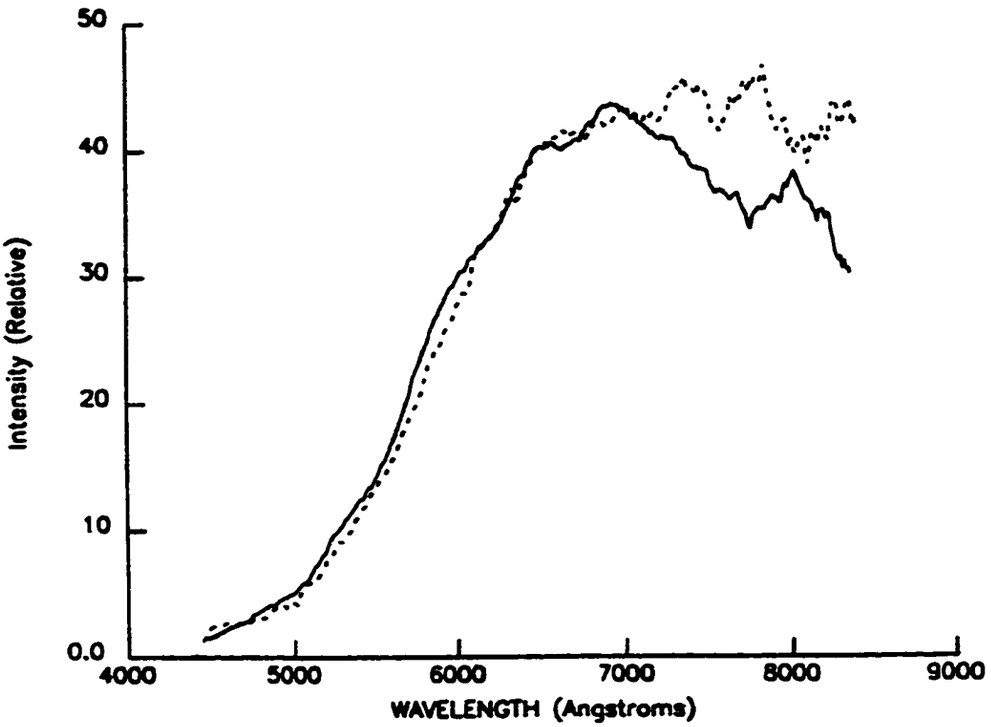

Figure 2.5. Measured Laboratory Glow Spectrum

2.5 Flow Field Characteristics

As has been indicated previously, this work focuses on an altitude range of 140 km to 300 km. Over this range, ambient conditions vary greatly. Conditions vary for many other reasons as well, including latitudinal and longitudinal location[35], local time of day[36], solar activity[37], and strength of the Earth's magnetic field[38]. Accordingly, it is difficult to quantify exactly many of the atmospheric parameters. However, the range is relatively small in comparison to the extent of the atmosphere of the Earth, so some approximations can be made about the conditions in general. This section describes both the differences and commonalities in order to better understand the characteristics of glow-producing flow fields.

2.5.1 Macroscopic Variations

The entire altitude range of interest here falls within the thermosphere, with a general increase in ambient temperature with altitude. The temperature varies from approximately 618 K at 140 km to 938 K at 300 km and an example temperature distribution is given in Table 2.1[39]. The table also show typical values for the number density and for the mean free path. The range of mean free paths is very illustrative. In all cases, the mean free path is above 10 m, indicating a rarefied flow field over the entire altitude range. At the higher altitudes, the mean free path is extremely large, which suggests a nearly collisionless flow field. While certainly true for conditions near ambient, there is a build up of particles in front of the ram surface. In this region, the local mean free path can be substantially smaller and the assumption of a collisionless flow field is incorrect. In general, though, the atmosphere may be characterized by increasing temperature and decreasing number of collisions with altitude.

A further consequence of the extremely low densities is the effect on equilibrium. The effect is visible in two forms. The first is the extreme degree of non-equilibrium in the flow field. The different temperature modes—translational, rotational, vibrational—typically all exhibit non-equilibrium behaviors. Given the low number of collisions, chemical non-equilibrium is also to be expected. There simply are not enough collisions to have recombination reactions balance dissociation. The second form of the effect is that thermodynamic concepts such as temperature lose their standard meanings. The reason for this is straightforward; the velocity distributions are often non-Maxwellian. In fact, the rarefied nature of the flow field can often lead to bimodal velocity distributions. Collisions of a group of particles mov-

Table 2.1. Sample Atmospheric Quantities

Altitude [km]	Temperature [K]	Number Density [m^{-3}]	λ [m]
140	618.2	7.3×10^{16}	19
150	697.9	4.2×10^{16}	33
160	757.8	2.6×10^{16}	54
170	803.0	1.8×10^{16}	78
180	837.0	1.2×10^{16}	120
190	862.6	8.7×10^{15}	160
200	882.0	6.4×10^{15}	220
250	927.1	1.6×10^{15}	880
300	938.4	5.2×10^{14}	2700

ing towards the ram surface at orbital speeds with the surface reflect the particles at much lower speeds in the opposite direction. The density of the flow field is low enough that very few particles from these two groups collide. Thus, the velocity distribution consists of two sharp peaks. With temperature being based on the width of velocity distribution, the definition breaks down under these conditions. It still can be a useful quantity, as a local temperature can indicate the amount of energy in an area of the field. However, the thermodynamic definition of temperature is of little importance. An additional effect of the bimodal velocity distribution is that the particles that do collide predominately have a very large relative velocity. Interactions with such a high collision energy have a higher probability of leading to chemical reactions. A comparison of typical collision energies with the activation energies of critical reactions is given in Section 6.1.2.

2.5.2 Atmospheric Composition

As was discussed in the introduction, in the unmixed upper thermosphere, the density of each species varies exponentially with altitude with a separate scale height[40]. The pressure scale height for a particular species is given by:

$$H \equiv \frac{kT}{Mg}. \tag{2.1}$$

The scale height is an e-folding distance in a model atmosphere; thus, when at an altitude which is a distance H above some reference altitude, the pressure will be $1/e$ times the pressure at the reference altitude. A similar scale height can be determined for density. In the Earth's atmosphere the density and pressure scale heights differ from each other by only a few percent.

The atmospheric composition over the range of interest exhibits both variations and general trends. As is typically done for simulations of high altitude air, a five species mixture is assumed: N_2, O_2, NO, N, and O. Atomic nitrogen and oxygen are formed though photodissociation of their molecular counterparts as well as through chemical means[41, 40]. At the lower end of the altitude range, the dominant species are N_2, O_2, and O. Molecular oxygen has a lower bonding energy than molecular nitrogen, so it dissociates more readily. Furthermore, nitrogen is lighter than oxygen, so oxygen is more predominant at lower altitudes. At the upper end of the range, the composition changes noticeably. There is a substantial increase in the concentration of atomic nitrogen, again due to the lower molecular weight and therefore greater scale height of nitrogen. Also apparent is that atomic oxygen is the dominant species, whereas molecular nitrogen dominated the lower range. Differences in composition are shown pictorially in Figure 2.6.

Despite the change in atmospheric composition with altitude, it is observed that

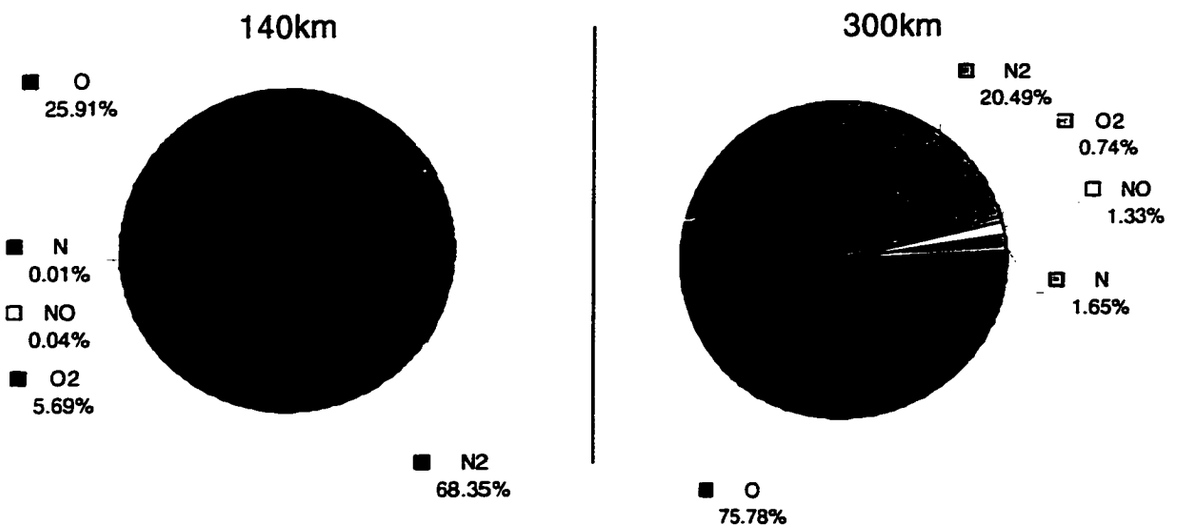

Figure 2.6. Change in Relative Concentrations with Altitude

some species are often present in relatively low quantities over a range of altitudes. For all following discussions, a species whose relative concentration at a particular altitude is 10^{-2} or less is considered a *rare* species. A complementary definition is made, with the other species being considered *common*. For reasons that will become apparent in the discussion of the particle method used to simulate the flow field, a species is considered rare only if it is also not created in quantity in the flow field. A species that is created easily through chemical reactions of the common species will not have a low concentration in the steady state solution of the flow field. It is noted that for a vast majority of the altitude range considered here, nitric oxide is a rare species. For the lower altitudes, atomic nitrogen is a rare species as well.

Of particular interest is the number density of nitric oxide, which has an imporant role in glow production. Unfortunately, the density of NO is very difficult to determine analytically. The density is sensitive to a variety of parameters, including solar radiation and ionic activity in the atmosphere. As a result, variations are seen in the density of NO with altitude[38, 42], local time of day and time of year[36, 43], latitudinal and logitudinal position[35, 44, 45], solar activity[37, 46, 47, 48, 49], and auroral activity[50]. In addition to measurements by satellites such as the Atmosphere Explorer, rockets have been used to gather experimental data on the structure of NO density in the thermosphere[51, 52]. The difficulty of determining nitric oxide concentrations is evidence of complicated chemical and dynamic behavior of the thermosphere.[53, 54]

Chapter 3

DSMC and Resolution Issues

For this work, the direct simulation Monte Carlo (DSMC)[9] method is chosen to simulate the glow production flows. In this chapter, the method is outlined, some fundamental resolution problems are discussed, and standard resolution enhancements are described.

3.1 The Direct Simulation Monte Carlo Method

The DSMC technique is a particle method that has been successfully applied to a wide variety of engineering applications. The method is well suited to simulate rarefied flows where non-equilibrium effects dominate. Examples include flows involving hypersonic shocks[55], radiative emissions[56], and aerothermochemistry in general[57]. In combination with other methods that handle electromagnetic effects, the DSMC technique has been applied to a number electric propulsion devices, including ion engines[58], Hall thrusters[59], and arcjets[60], as well as plasma etching of silicon devices[61]. In addition, the method has been used to simulate thin film

deposition[62] and micro-electro-mechanical systems[63].

In general, the DSMC technique is applicable to dilute gas flows where binary collisions dominate. The computational domain is divided into cells of arbitrary, polygonal shape and these cells hold a number of computational particles. The DSMC method can resolve spatial gradients only on the scale of the cell size, due to the technique employed to simulate collisions. The collision algorithm is discussed in greater detail later in this section. Thus, cells are ideally sized based on a fraction of the local mean free path in the flow so that gradients are resolved. Each particle in the simulation represents a large number of real molecules of a particular species and has a unique mass, velocity and internal energy. The ratio of the number of real particles to the number of simulated particles is termed the reference particle weight (W_p). This reference particle weight may be varied for the different chemical species[9] or for each computational particle[64]. The applicability of species and particle weighting in simulations of glow producing flows is discussed below. The reference particle weight can also be varied across the domain, with each computational cell having a distinct weight. Use of this sort of weighting also requires some consideration when employed in the rarefied flows under consideration and is addressed below.

In the DSMC technique, the time step is chosen to be a fraction of the mean collision time of the flow, in order to decouple the particle motion from the collision mechanics. As with the particle weight, the local time step may be varied in each cell. This is valid only for steady state solutions of the flow field; time accurate solutions would restrict the time-step to a globally uniform value. Varying the time step also indirectly affects the effective particle weight[65]. This is discussed more

fully in Section 3.3.2.

Particle motion can be limited to any number of dimensions—from fully three-dimensional flows to zero-dimensional flows where no actual motion occurs. Three-dimensional simulations are often necessary to accurately model complex, engineering geometries. One-dimensional simulations are useful to study the behavior of simpler phenomena such as rarefied shocks. A zero-dimensional simulation focuses directly on particle interactions, be it an exchange of internal energy or a chemical reaction. Such simulations are helpful in the validation of new particle interaction models. It is also common to consider an axisymmetric simulation, where particles moving in a three-dimensional domain are rotated each time step into a plane. Particle motions in an axisymmetric simulation follow hyperbolic paths[66]. For flow exhibiting an axial symmetry, this is much more computationally efficient than simulating a full three-dimensional flow field. All of the DSMC results considered in this work are the output of axisymmetric simulations.

Collision probabilities in the DSMC technique are determined for pairs of particles in the same cell. These probabilities are chosen so that the overall collision rate agrees with the results of kinetic theory. A variety of schemes can be used to calculate the collision probabilities. One such scheme is given in Ref. [67]. Parameters controlling the collision model are chosen so that during the course of the simulation the instantaneous probabilities lead to a physically valid collision rate. A particle may collide with any other particle in the same cell; the distance between the individual particles does not affect the probability. Therefore, as mentioned above, gradients in flow field properties are resolved only down to the scale of cell size. Note that the DSMC method is not a molecular dynamics calculation, where

the actual intersections of particle paths are used to determine collisions.

Each collision exchanges linear momentum and kinetic energy, with conservation of both properties being enforced in the standard implementation of the method. Some variant schemes exist that do not allow for momentum and energy both to be conserved in an individual collision; an example is found in Ref. [64]. The scattering angle of the particles after a collision is determined via the collision model employed. The most common model is the variable hard sphere model where the scattering angle is sampled from an isotropic distribution[9]. An alternative model is the variable soft sphere model, which uses a weighted random distribution, with the weighting depending on the pre-collision properties of the collision pair[68]. Neither of these schemes conserves angular momentum. A lack of conservation could indicate a potential difficulty in simulating high vorticity flows with the DSMC method[69]. However, it is found that, if the cells are scaled properly to a fraction of the mean free path, the rotational features of flows can be captured[70]. Additionally, for collisions involving at least one molecular species, internal energy modes, including rotational and vibrational energy, may be affected by the collision. A variety of exchange models may be used to determine the probability of internal energy transfer[71, 72, 73]. Parameters in a particular exchange model are chosen to match known relaxation rates. Finally, each collision may lead to a chemical reaction. Both exothermic and endothermic reactions are allowed, with the change in energy being accounted for in the post-reaction velocity and internal energy of the products. The energy of the reaction is combined with the total collision energy of the pair. The internal energies and velocities of the products are determined based on this total energy and the state of the reactants before the collision[9, 74]. Recombination

reactions are also allowed. Such reactions require a third body to conserve linear momentum and energy simultaneously. Typically, a small portion of the particles in a cell are reserved as potential third bodies in recombination reactions.

Interactions between the particles and physical surfaces are also included in the DSMC method. The nature of the interaction depends on the surface model employed. In general, the particle may undergo a specular or diffuse reflection. Under a specular reflection, the angle of incidence is equal to the angle of departure and there is no change in the energy of the particle. With a diffuse reflection, the particle is accommodated to the temperature of the surface. The particle is reflected with a velocity and energy that are sampled from equilibrium distributions based on the wall temperature. Real engineering surfaces usually lie somewhere in between fully specular and fully diffuse. To represent these types of surfaces, an accommodation coefficient is used. The accommodation coefficient indicates what fraction of particle-surface interactions are diffuse; the remainder of the reflections are treated as specular.

Experimental results, continuum numerical computations and theoretical predictions are usually represented by macroscopic variables. It is necessary to be able to extract macroscopic quantities from the microscopic details of a DSMC simulation. To accomplish this, the aggregate properties of particles in each cell are sampled, summed, and averaged over time. These values are used, along with results from statistical mechanics, to obtain macroscopic quantities. There exists a certain amount of statistical error in any of these calculated values. Thus, DSMC results are often less smooth than those of comparable continuum calculations. Statistical accuracy has been shown to be directly related to the number of particles

in the cell and the number of time steps over which sampling is performed[75]. In a steady state calculation, sampling may begin after the transient portion of flow has relaxed. In a time accurate simulation, the sampling period must be significantly shorter than that for a steady state calculation. Otherwise, variations of properties that fluctuate with a short time scale would be lost in the average sampled values. In order to retain low statistical error, the requirements on particle count are often much more severe.

The DSMC technique lends itself to parallelization on computers with multiple processors[66]. The natural choice for domain decomposition is a spatial one, with each processor holding a fraction of the cells. A decomposition among particles is also possible. The advantages of parallelization include an increase in the possible particle count given constant memory restrictions per processor and a decrease in the real time requirements of the calculation. As with most parallel applications, the main disadvantage is a loss in efficiency due to interprocessor communication. Schemes to balance the number of particles are often used to achieve an optimal division between computation and communication[65].

3.2 Resolution Difficulties

A key consideration in any DSMC simulation is to resolve the flow accurately throughout the domain. In flows involving glow production, there are two specific characteristics that make resolution extremely difficult, namely rare chemical species and rare events. These are addressed in the following sections.

3.2.1 Rare Species

For purposes of this work, a chemical species is considered rare if it has a concentration that is a factor of 10^{-2} or less than that of the bulk gas. The simulation of rare species using the DSMC technique causes a number of resolution difficulties. When simulating a flow field with one or more rare species, there is often no single acceptable choice for the value of the particle weight. A relatively low value of W_p is required in order for a statistically significant number of particles representing the rare species to be generated. However, with the particle weight set at such a value, inordinate numbers of particles representing the common species will also be generated. This results in unacceptably high numbers of simulated particles in each cell, requiring excessive amounts of computational effort to calculate the flow field. Alternatively, the value of W_p can be set relatively high, so that reasonable numbers of common species particles are produced. In this case, however, very few, if any, rare species particles are produced and the simulation no longer generates meaningful statistics for the rare species. This fundamental limitation is illustrated in Figure 3.1. Prior experience with rare species and resolution difficulties are discussed in Refs.[76] and [77].

3.2.2 Rare Events

Rare events are also fundamentally difficult to capture using the DSMC method. Two specific types of rare events produce these difficulties. The first type occurs in a flow where the density is low enough that collisions themselves become rare. It is also possible to have one particular class of collisions that is rare. Given the limited number of computational particles in a cell, there are not enough simulated

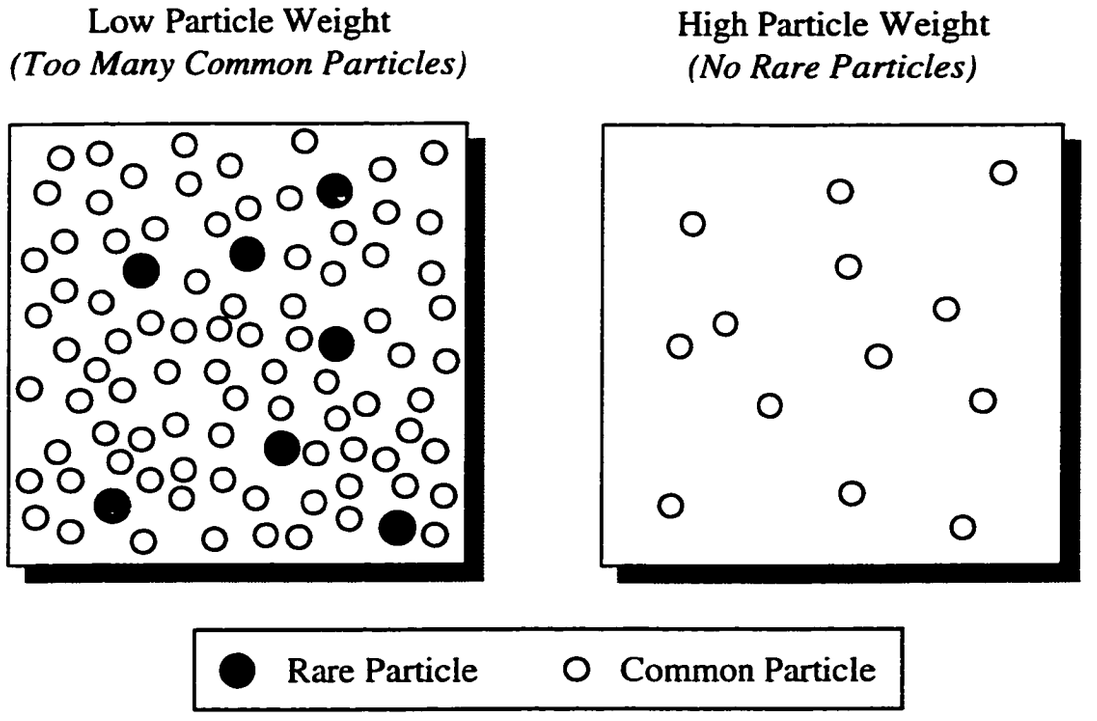

Figure 3.1. No Appropriate Choice for W_p

collisions to accurately represent the true collision rate. If these rare collisions have a significant effect on the structure of the flow field, the DSMC method will fail to produce an accurate simulation. The second type occurs when reaction parameters and particle properties cause the probability of a chemical reaction to be very low. Despite a significant number of collisions of potential reactants, very few product particles will be created and thus will be underrepresented in the simulation. These products, although rare in the real flow, could still be significant in a variety of circumstances. For example, experimental measurements of the flow field may focus on a unique signature of the rare products. A lack of resolution in calculating this signature inhibits the ability to compare the simulation results with experimental measurements. Furthermore, the products of the rare events, while insignificant

to the bulk gas, could drastically affect the densities and distributions of the rare species.

3.3 Resolution Enhancement

A variety of enhancements and modifications have been attempted to deal with particle resolution issues in general and rare species and event modeling in particular. A subset of these potential changes is discussed in the following sections, with an emphasis placed on the applicability to flows involving glow production. Most of these modifications are unrelated and a combination of them is often applied in a particular engineering simulation.

3.3.1 Weighting

As was mentioned in previous sections, several variable weighting techniques are possible in the DSMC method. Although different in approach, each technique essentially results in a change in the effective weight of an individual particle, that is, the number of real particles represented by the single computational particle.

Perhaps the most common weighting technique is a spatial variation in weights, with each cell or group of cells having a different weight. All particles within a cell are assigned the weight of that cell. The modified weight is used in most calculations of macroscopic quantities; the common exceptions are the calculation of temperature and velocity. An increase in weight in cells of large volume, specifically cells far from the axis in an axisymmetric simulation, reduces the particle count and allows a concentration of particles in the smaller cells. Even with the assumption of

constant density, smaller cells would normally contain fewer particles. Furthermore, it has been shown that as density increases the particle count actually decreases. This is a consequence of the the DSMC cells being sized to the local mean free path in the flow. Details are contained in Ref. [65]. Weighting by cell can directly help counteract this resolution problem. The movement of a particle between cells of differing weights requires additional considerations. When moving from a cell of lower weight to a cell of higher weight, there is a probability based on the ratio of the cell weights that the particle is destroyed as it crosses the edge between the cells. This destruction is required, because in cells with a higher particle weight, fewer simulated particles are needed to represent the same real density. The opposite effect is required when moving from a cell having a higher to a cell having a lower weight; there is a probability that the particle is cloned or duplicated. Since there is no basis other than the particle properties of the crossing particle to generate new particle properties, the new particle is typically identical to the crossing particle. The cloning of particles introduces additional statistical error into the simulation. In particular, cloned particles result in spikes in the distribution of particle properties. In flows with a suitable number of collisions, these initially identical particles quickly attain different properties. However, in extremely rarefied flows, the collision rate is too low to significantly separate the properties of duplicate pairs. Thus, a decrease in cell weights, especially in the primary flow direction, is to be avoided in such flows. The atmospheric conditions around the Atmosphere Explorer satellite and the space shuttle in the altitude ranges of interest are sufficiently rarefied that spatial weights indeed need to be avoided.

Another manner in which weights may be varied is to assign a different weight to

each chemical species. Initial implementations of this technique conserved momentum and energy only on the average; individual collisions were non-conservative[9]. Alternative techniques show that it is not possible to conserve both momentum and energy in a collision involving particles of different weights[64]. Momentum is typically conserved, with a correction of energy being collected as a remainder in the cell. This energy is redistributed among future collision pairs. In such collisions, the particle with the higher weight is split into two particles, one of which undergoes the collision and then the particle is recombined. In chemically inert flows, species weighting can significantly improve the resolution of rare particles. It is not clear how to simulate reactions between particles whose species have different weights. Thus, species weighting is unable to handle flows with chemical reactions, which play a dominant role in glow production flows. Thus, species weighting is not applicable for these flows.

A slight modification of the species weighting technique is particle weighting, where each particle carries with it a weight[78]. These weights are initially set to the same value for all particles of the same species; this is identical to species weighting. If nothing else is modified, all limitations and comments from the previous discussion of species weighting concerning collisions of disparate weight particles hold. With each chemical reaction, the individual weights of the products are modified and the split particle is not recombined. Thus, each reaction creates a new particle. Such a scheme is able to conserve both momentum and energy on a per collision basis. Conceivably, this could be applied to momentum transfer collisions as well as reacting collisions. While able to simulate chemically active flows, the bookkeeping involved with chemical reactions is sufficiently complex to make particle weighting

unattractive. Since each chemical reaction results in a new particle being created, a significant number of chemical reactions can reduce the effectiveness of particle weighting to resolve rare particle resolution difficulties. Growth of the particle count in an implementation where all collisions create a third computational particle could result in the computation quickly becoming intractable.

3.3.2 Variable Time Steps

Time steps may be varied by cell in much the same way that particle weights may be varied. The local time step is used to calculate particle motion and to determine collision probabilities. Use of variable time steps is often necessary in flows where the inherent time scale in the flow varies by several orders of magnitude throughout the domain. A typical example of such a flow would be expansion of a thruster plume into a vacuum. Use of the smallest required time step in the large cells far from the high density, thruster exit would require a large number of time steps in order to reach steady state. When sampling and macroscopic variables are considered, a modification to the time step is equivalent to a change in the effective particle weight. No cloning or destruction of particles passing between cells of different time steps is necessary. Therefore, judicious use of variable time steps may be used to simulate spatial weighting without any of the statistical drawbacks.

Unfortunately, variable time steps do nothing to address the resolution difficulties due to either rare species or rare events. The corresponding idea to more specific particle weighting of species time steps or individual particle time steps is nonsensical. Thus, while variable time steps may be used effectively in glow production flows, this does not solve the resolution difficulties inherent in these flows.

Chapter 4

Overlay Methods

A number of resolution difficulties are discussed in Chapter 3 (see Section 3.2) and common techniques used to overcome these difficulties are offered. Unfortunately, none of these techniques allows the simulation of glow production flows with the desired accuracy. A more effective approach is that of an overlay method. With an overlay method, two simulations are performed. The first simulation calculates the common species flow field, and the second simulation tracks the rare species behavior.

4.1 Continuum Overlay

One approach that addresses rare species and event resolution difficulties is to use a continuum overlay method[76, 77]. A two step procedure is used to calculate the flow field. In the first step, a standard DSMC simulation is performed to determine the properties of the common species throughout the flow domain. The particle weight in this simulation is set so that essentially no rare species particles are created.

The second step involves a continuum-based calculation, where mass conservation equations are solved for the rare species using the underlying DSMC flow field solution as a background. The assumption is made that the behavior of the rare species does not have an appreciable effect on the common species flow field.

Given the assumption that the trace species are present in such small amounts that they do not affect the overall flow field, the DSMC calculated flow field serves as the unvarying flow field. Mass conservation is then invoked leading to the following conservation equation:

$$\frac{\partial \rho_s}{\partial t} + \frac{\partial}{\partial x_j}(\rho_s u_j + \rho_s v_{sj}) = w_s, \quad \text{for } s = 1, \ldots, n, \tag{4.1}$$

for each of the n trace species ,where ρ_s is the trace species density, v_{sj} is the diffusion velocity and w_s is the chemical source term for species s. The mass-averaged velocity, u_j, is determined from the DSMC solution.

This continuum-based approach has two problems. By definition, the use of a continuum-based overlay results in a loss of microscopic detail. In particular detailed knowledge of the rare species is unattainable via a continuum method. Such detail, particularly velocity distributions, may have a significant impact on chemical rates and glow production. It is important that this microscopic information is retained throughout the simulation if glow production is to be accurately modeled. Furthermore, the procedure used to solve the mass conservation equations makes use of the temperature calculated for the common species in each computational cell. However, in the range of altitudes relevant for spacecraft glow, the flow field is sufficiently rarefied and in such a degree of non-equilibrium that thermodynamic variables such as temperature are not valid representations of the state of the gas. The velocity distribution of the molecules is very often bimodal and certainly not

Maxwellian. It is therefore inappropriate to use thermodynamic temperature to characterize the underlying flow field.

It is beneficial to examine in more depth why the thermodynamic concept of temperature is misleading under glow production conditions. Fick's law[79] is used to determine the diffusion velocity in the overlay method, Eq. 4.1, which states that for a binary mixture of species A and B:

$$\mathbf{j}_A = -\rho \mathcal{D}_{AB} \nabla c_A, \tag{4.2}$$

$$\mathcal{D}_{AB} = 0.0018583 \frac{\sqrt{T^3 \left(\frac{1}{\mathcal{M}_A} + \frac{1}{\mathcal{M}_B}\right)}}{p d_{AB}^2 \Omega_{d,AB}}, \tag{4.3}$$

where $\mathbf{j}_A$ is the mass flux of species A, c_A is the mass fraction of A, $\mathcal{D}_{AB}$ is the diffusion coefficient in units of $\mathrm{cm^2 s^{-1}}$, $\mathcal{M}$ represents the molecular weight, T is the temperature in K, p is the pressure in atm, d_{AB} is an average of the reference diameters for the two species in Å. Values for $\Omega_{d,AB}$, which represents a collision integral that gives the variation of the effective collision diameter with temperature, are given in Anderson[79]. Examination of Fick's law shows that the diffusion velocity is dependent on the temperature. As was previously mentioned, care must be taken in determining what temperature to use. The cells in front of the body are populated by two distinct families of particles. One family is simply a sample of the incoming particles, with thermal velocities determined by a distribution based on the free-stream temperature. These thermal velocities are distributed about a large free-stream velocity of around 8 km/s in the axial direction. The other family consists of particles that have collided with the blunt front surface of the satellite and are traveling in an opposite direction to the first family. Due to the fact that the flow is nearly collisionless, these two sets of particles can pass by one another

with little interaction. The DSMC formulation calculates a very high temperature in such a cell. While this high temperature is appropriate for characterizing the reaction probability for the few collisions that do occur, it is not an appropriate temperature to use in Fick's law. Using such a high temperature in the overlay calculation results in a correspondingly high diffusion velocity. Particles created along or near the axis diffuse away at rates that much greater than to the actual rate of diffusion. A more appropriate diffusion velocity would be one on the order of the radial velocity of the free-stream molecules. Therefore, a radial temperature calculated by the DSMC method is used in Fick's law to evaluate the diffusion velocities. Since the particles rebounding from the surface have roughly the same radial velocity of the incoming particles, the radial temperature is much smaller in comparison to the total temperature. In general, the radial temperature will be higher near the body than in the free-stream. This rise in temperature is the result of collisions between the two families of species described above; the rare collisions between representatives of these two families collide with a large amount of energy. The collisions allow the transfer of kinetic energy from the axial direction to the radial direction.

Despite these drawbacks inherent to a continuum method applied to such rarefied flows, useful results can still be obtained from using the method. Ref. [77] presents results from the continuum-overlay method applied to the problem of the prediction of re-entry emissions of a test vehicle. As stated in the paper, the use of an overlay method in general allowed for useful results to be calculated; work prior to that of Ref. [77] provided completely unsatisfactory predictions.

4.2 DSMC Overlay

Conceptually, the DSMC overlay is very similar to the continuum overlay approach, where two separate simulations are performed. In this case, however, both simulations use the DSMC technique. In the first (*base*) simulation, the particle weight is set so that the common species are represented at an appropriate level. In the second (*overlay*) simulation, the particle weight is reduced so that the rare species are represented. Generation of the common species is suppressed during the overlay simulation. In essence, the overlay simulation can be considered as a magnified simulation, focusing only on the rare species. As a particle method, the DSMC technique is ideal for handling the non-equilibrium nature of the flow field and for determining the microscopic behavior of the particles. Thus, the DSMC overlay approach overcomes the two main disadvantages of the continuum overlay method.

4.2.1 Coupling Between Rare and Common Species

The main challenge of performing a DSMC overlay simulation lies in achieving a detailed coupling between the two distinct simulations. This is not a concern in the base simulation, as it is assumed that the flow field of the common particles is unaffected by the behavior of the rare particles. It is a significant concern, however, when performing the overlay simulation. The overlay simulation cannot simply be assumed to be a regular DSMC simulation at a lower density. The rare particles are moving through and colliding with a background of much denser common species. In addition, rare chemical events in the base simulation that did not noticeably affect the common species flow field may have a pronounced effect on the rare species flow field.

In order to achieve this coupling, the particle properties are binned in every cell during the sampling period of the base simulation. Five different properties for each species are binned: the three components of velocity, the rotational energy and the vibrational energy. During the overlay simulation, a temporary common particle is created to act as a collision partner for each rare particle in every cell. These temporary particles have their properties determined through sampling of the bins stored during the base simulation. The binned properties are taken to be statistically independent for this sampling. From these pairs, the appropriate number of common-rare collisions is determined. After standard DSMC collision mechanics are performed, the temporary particles are discarded. The procedure is illustrated in Figure 4.1. Thus, the particles of the overlay simulation interact with the background flow field at the microscopic level. It is important to note that given the assumption that the rare species have a number density that is several orders of magnitude lower than the common species, the probability of common-rare collisions is much greater than rare-rare collisions. In the cases considered here, rare-rare collisions are neglected in the overlay simulation.

4.2.2 Chemistry in DSMC Overlay

Applying the DSMC overlay procedure outlined above to chemically reacting flows is somewhat more involved. It is important to determine which classes of collisions will lead to chemical reactions that affect the rare species. The three possible candidates are common-common collisions, common-rare collisions and rare-rare collisions. As was previously mentioned, rare-rare collisions are neglected, so no reactions stemming from these types of collision are considered. Common-rare col-

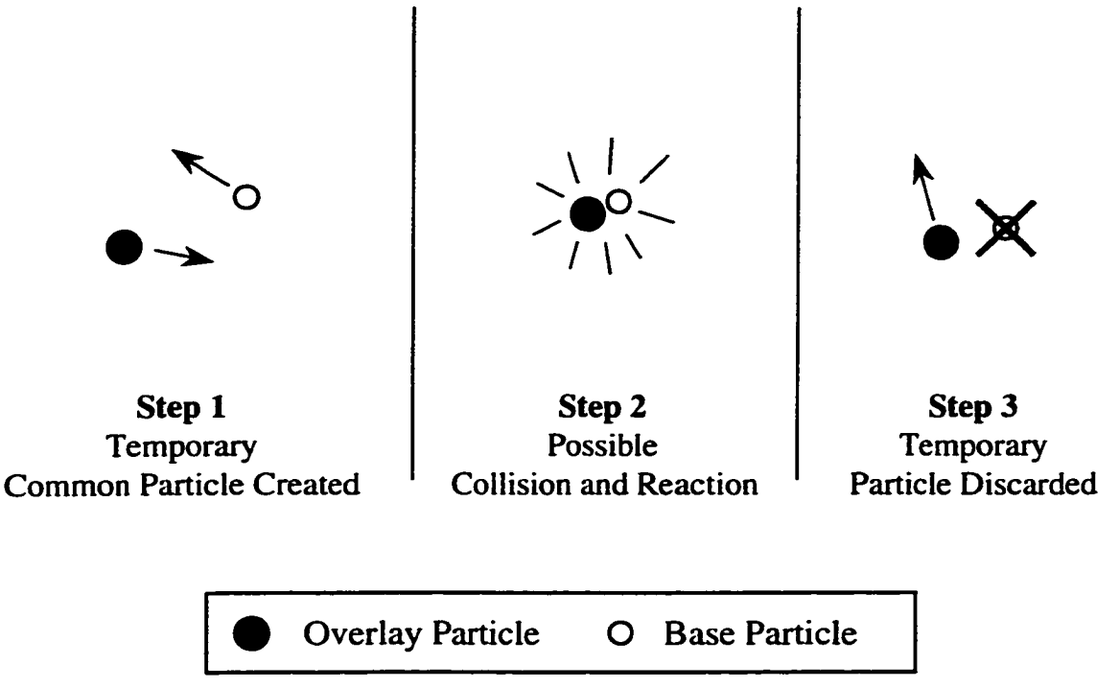

Figure 4.1. Interaction Between Base and Overlay Simulations

lisions are handled using the bins and temporary particles. Standard DSMC reaction routines are used to calculate the probability and mechanics of common-rare reactions. After any such reaction, only rare particles remain in the simulation. However, consideration must be given to the relative importance of common-rare reactions compared to the common-common reactions. Since the probability of a common-rare collision is several orders of magnitude lower than a common-common collision, the reaction probability must be very high in order for the common-rare reaction to be important relative to the common-common reaction. In the cases considered here, the reaction probabilities for the reactions of interest are not sufficiently high, and the inclusion of common-rare reactions has no quantitative effect on the rare species flow field. This leaves only common-common reactions as the

important reactions in terms of the production of rare species.

Common-common reactions cannot be handled during the overlay simulation using standard DSMC techniques, because no common-common collision pairs are processed. These reactions are of course simulated in the base simulation. However, by assumption, the rate of production of rare species through these reactions must be low. If it were not, the rare species would be produced in quantity and would no longer be rare. The production can be low for two reasons; either there are very few collisions or the reaction probabilities are low. Thus, fundamentally, the DSMC method will have difficulty representing these reactions. Regardless of the technique used to determine the concentration and properties of the rare particles created via these reactions, their introduction into the overlay simulation will take the form of a source term for each rare species in every cell. A more general scheme for accomplishing this would require binning more detailed information, such as velocity distributions of the population of reacting particles, during the base simulation. For this work, an approximate method of determining both the rate of production and the properties of the rare species due to common-common reactions is used. The predominant reaction considered is:

$$N_2 + O \rightarrow NO + N. \tag{4.4}$$

It is assumed that only the most energetic collisions lead to chemical reaction. In the Atmosphere Explorer flows, these occur when a free stream particle collides with a particle that has rebounded from the ram surface of the satellite. Thus, there are two different types of collisions leading to the formation of nitric oxide:

$$\vec{N_2} + \overleftarrow{O} \rightarrow \vec{NO} + \vec{N}, \tag{4.5}$$

$$\overleftarrow{N_2} + \vec{O} \rightarrow \vec{NO} + \vec{N}, \tag{4.6}$$

where the arrows indicate the direction in which the particle is moving. Arrows to the right indicate motion towards the surface. Thus, reaction (4.5) represents a free stream nitrogen molecule, moving at orbital speed, colliding with an atomic oxygen molecule that has reflected from the surface. Reaction (4.6) represents free stream atomic oxygen reacting with reflected N_2.

Data on the velocity distributions of O and N_2 scattered from a surface at orbital speeds are limited. Examination of the collision of 8 km/s oxygen atoms with engineering surfaces indicates that the scattering is largely diffuse, although the scattered atoms have a broad velocity distribution centered around 1 km/s[30]. Limited measurements of high velocity N_2 scattering suggest that the mean scattered velocity is approximately 2 km/s[80]. Using a value of 8 km/s for orbital speed, this results in a relative velocity of 9 km/s or 10 km/s for Reactions (4.5) and (4.6), respectively. Using these approximations and appropriate values for the cross-section of the reaction at these speeds, the rate of production of NO and N can be determined in each cell using the equation:

$$\frac{\mathrm{dn(NO)}}{\mathrm{dt}} = \frac{\mathrm{dn(N)}}{\mathrm{dt}} = \mathrm{n}(\vec{\mathrm{N}_2})\mathrm{n}(\overleftarrow{\mathrm{O}})g_{4.5}\sigma_{4.5} + \mathrm{n}(\overleftarrow{\mathrm{N}_2})\mathrm{n}(\vec{\mathrm{O}})g_{4.6}\sigma_{4.6}, \tag{4.7}$$

where $\mathrm{n}(\vec{\mathrm{X}})$ represents the number density of species X moving in the direction indicated by the arrow, g is the estimated relative velocity and σ is the reaction cross-section. Values for σ are obtained from a molecular dynamics trajectory analysis[81] and are presented in Section 6.1.2.

Given the high relative velocity of the reactants, a comparison of collision energy with chemical activation energy is useful. Reaction (4.4) has an activation energy of approximately 5.2×10^{-19} J. A collision between molecular nitrogen and atomic oxygen with an assumed relative velocity of 10 km/s has a collision energy of ap-

proximately 8.5×10^{-19} J, which is greater than the activation energy. Thus, a high probability of reaction is expected under these conditions.

In each cell at each time step, a number of NO and N particles are generated according to the production terms evaluated using number densities and velocity distributions from the base simulation. For components of velocity perpendicular to the flow direction, the properties of the NO and N particles created can be approximated from the velocity distributions of N_2 and O, respectively. The velocity component in the direction of the flow for the newly formed NO and N is approximated by the center of mass velocity of the collision pair, with a thermal spread obtained by sampling the azimuthal velocity distribution in that cell.

Another exchange reaction becomes important in the upper portion of the altitude range of interest. This reaction is:

$$O_2 + N \rightarrow NO + O. \tag{4.8}$$

This reaction is less important at the lower altitudes because atomic nitrogen is not available in sufficient quantities at these altitudes. Again, collisions where the reactants move in both directions are considered:

$$\vec{O_2} + \overleftarrow{N} \rightarrow \vec{NO} + \vec{O}, \tag{4.9}$$

$$\overleftarrow{O_2} + \vec{N} \rightarrow \vec{NO} + \vec{O}, \tag{4.10}$$

As with the first exchange reaction, values of a reaction cross-section must be determined. These are given in Section 6.1.2. A comparison of collision energy with activation energy is again useful. Reaction (4.8) has an activation energy of approximately 5.0×10^{-20} J. The energy of a 10 km/s O_2-N collision is approximately

8.1×10^{-19} J. Thus, high reaction probabilities for the second exchange reaction are to be expected as well.

Chapter 5

Surface Event Modeling

In Chapters 3 and 4, the DSMC method and overlay techniques are described. As is discussed, this method is well suited to simulate the rarefied flow field in which glow is produced. Use of this method alone ignores any details of the surface events and chemistry that may effect glow production. Prior work shows that exclusion of surface phenomena and the reliance on an oversimplified model leads to a vast overprediction of glow brightness[10]. More detailed modeling of surface phenomena is therefore required. This chapter describes the types of surface events that are considered in this work. Mathematical models of each reaction type are given. The numerical solution procedure is discussed. Finally, a steady state analysis of the resulting set of equations is presented.

5.1 Surface Event Modeling

Glow measurements from the shuttle, the Atmosphere Explorer satellite, and ground-based laboratory experiments are consistent with the spectrum of NO_2^*. Nitrogen

dioxide does not appear naturally in any appreciable quantities in the Earth's atmosphere. Furthermore, there are not enough collisions in the rarefied flow field to create nitrogen dioxide in quantity in the gas phase. This leads to the conclusion that the excited nitrogen dioxide must be created on the ram surface.

In order to capture the behavior of the processes leading to the creation of NO_2^*, and therefore the creation of glow, a variety of surface events are modeled. Five types of surface events are considered: physical adsorption, thermal desorption, collisional desorption, gas-surface (Eley-Rideal) reactions, and surface-surface (Langmuir-Hinshelwood) reactions. In this section, each event is classified and described in terms of a general chemical representation. The parameters characterizing the events are then defined. Finally, the effect on the rate of change of surface number density is expressed in differential form.

For the purpose of discussion, the phenomena are divided into two categories: non-reacting and reacting events. These events are shown schematically in Figs. 5.1 and 5.2. The scheme used to solve for the surface concentrations depends solely on the differential description of the event and thus does not distinguish between the two categories. The solution procedure is detailed in section 5.1.3.

5.1.1 Non-Reacting Events

An adsorption event occurs when a molecule impacting the surface does not reflect, but rather is trapped on the surface. There are several ways in which a molecule may be adsorbed, physical and chemical adsorption being the two primary forms. Any molecule that chemically adsorbs to the surface is tightly bound and much less likely to participate in other surface events. Thus, the only type of adsorption

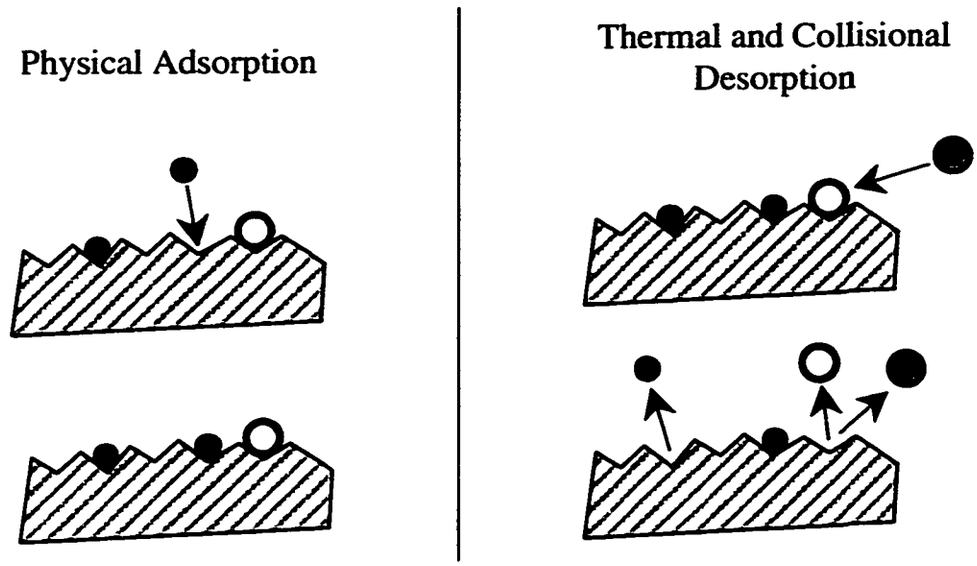

Figure 5.1. Non-Reacting Events

considered in this model is physical adsorption, where the physisorbed species are assumed to form a monolayer on top of the chemisorbed species[82]. A physical adsorption event is represented by:

$$\vec{Q} + X \rightarrow Q^a,$$

where X symbolizes a free surface site. Each event can be characterized by a sticking coefficient, which is simply the probability that a molecule striking the surface becomes adsorbed. The rate of change of surface number density for species Q is:

$$\frac{dn_Q}{dt} = S_Q F_Q \left(1 - \sum_{i=1}^{N} \frac{n_i}{n_s}\right). \tag{5.1}$$

The term in parentheses represents the fraction of adsorption sites that are uncovered and available.

Spontaneous desorption of a physisorbed molecule is termed thermal desorption. Such events occur when the thermal energy of the surface is large enough to overcome the bonding energy of the physisorbed molecule. Symbolically, this is:

$$Q^a \rightarrow \overleftarrow{Q} + X.$$

In this model, thermal desorption events are characterized by a time constant. This characteristic time combines the effect of binding energy and surface temperature. The rate of change of surface number density for species Q is:

$$\frac{dn_Q}{dt} = -\frac{n_Q}{\tau_Q}. \tag{5.2}$$

Collisional desorption is desorption that is initiated from the surface through a direct collision with an incident gas-phase molecule. An event of this type can be written:

$$\vec{A}_i + Q^a \rightarrow \overleftarrow{A}_i + \overleftarrow{Q} + X.$$

A collision cross-section characterizes collisional desorption events. Theoretically, this cross-section varies for each type of collision pair. In the present study, this parameter is varied depending only on the adsorbed species. The rate of change of surface number density for species Q due to species i is:

$$\frac{dn_Q}{dt} = -F_i n_Q \sigma_{iq}^d. \tag{5.3}$$

5.1.2 Reacting Events

Chemical reactions involving an incident gas-phase molecule and an adsorbed molecule are termed Eley-Rideal reactions. The product may stay adsorbed to the

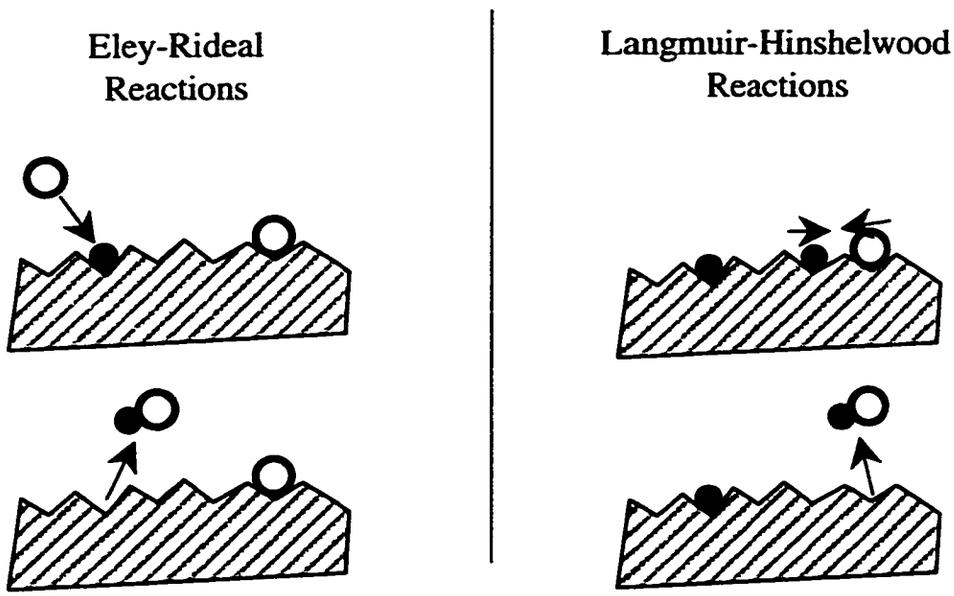

Figure 5.2. Chemically Reacting Events

surface or may be ejected into the flow field. Shown symbolically, these reactions are, respectively:

$$\begin{aligned} \vec{A}_i + A_j^a &\rightarrow Q^a, \\ \vec{A}_i + A_j^a &\rightarrow \overleftarrow{Q} + X. \end{aligned}$$

As with a collisional desorption event, an Eley-Rideal reaction is characterized by a cross-section. Each Eley-Rideal reaction results in a reduction of the surface concentration of species A_j. The surface concentration of species Q will increase if the particle remains adsorbed on the surface. Defining ϵ_{ij}^{er} as this probability of ejection into the gas phase of the species Q created from species i and j, the rates

of change may be expressed as:

$$\frac{dn_Q}{dt} = \left(1 - \epsilon_{ij}^{er}\right) \sigma_{ij}^{er} F_i n_j, \quad \frac{dn_j}{dt} = -\sigma_{ij}^{er} F_i n_j. \tag{5.4}$$

The final type of surface events considered is Langmuir-Hinshelwood reactions, involving two surface adsorbed molecules. Similar to gas-surface reactions, the resultant product may stay adsorbed on the surface or may be ejected into the flow field, or:

$$\begin{aligned} A_i^a + A_j^a &\rightarrow Q^a + X, \\ A_i^a + A_j^a &\rightarrow \overleftarrow{Q} + 2X. \end{aligned}$$

Noting that surface-surface reactions are described through a reaction rate as opposed to a cross-section, the rates of change become:

$$\frac{dn_Q}{dt} = \left(1 - \epsilon_{ij}^{lh}\right) K_{ij}^{lh} n_i n_j, \quad \frac{dn_i}{dt} = \frac{dn_j}{dt} = -K_{ij}^{lh} n_i n_j. \tag{5.5}$$

5.1.3 Complete Set of Equations

It is useful to define a species surface coverage, $\Theta_i \equiv n_i/n_s$, where n_s is the surface number density of available sites. Dividing Eqs. 5.1–5.5 by n_s and combining them, the overall rate of change of surface coverage for species Q can be written collectively as:

$$\begin{aligned} \frac{d\Theta_Q}{dt} &= \frac{S_Q F_Q}{n_s}\left(1 - \sum_{i=1}^{N}\Theta_i\right) - \frac{\Theta_Q}{\tau_Q} - \sum_{i=1}^{N} F_i \Theta_Q \sigma_{iq}^d \\ &+ \sum_{i=1}^{N}\sum_{j=1}^{N}\left(1 - \epsilon_{ij}^{er}\right)\sigma_{ij}^{er} F_i \Theta_j - \sum_{i=1}^{N} \sigma_{iq}^{er} F_i \Theta_Q \\ &+ \sum_{i=1}^{N}\sum_{j=i}^{N}\left(1 - \epsilon_{ij}^{lh}\right) n_s K_{ij}^{lh} \Theta_i \Theta_j - \sum_{i=1}^{N} n_s K_{iq}^{lh} \Theta_i \Theta_Q. \end{aligned} \tag{5.6}$$

Values for the fluxes are determined from the Monte Carlo simulations. A listing of all the events considered is given in Tables 6.3 and 6.4. Baseline values for the parameters in all the surface events are taken from the report by Gorelev, et. al[83]. These baseline values represent a collection of values from the literature as well as estimates and approximations. To complement the Gorelev report, values for the parameters of important events are taken from additional sources. In particular, sources were found for nitric oxide adsorption[84, 85, 86] and thermal desorption,[87] for molecular oxygen adsorption[88], [89], [90], [91], [92], [93] and thermal desorption[94], and for molecular nitrogen adsorption[95]. In general, for the above sources whose experimental conditions closely match ram-surface satellite conditions, these additional values support the values of the Gorelev report. Therefore, as a baseline case, the Gorelev values are used.

For many of the parameters of the important events, values are not available in the literature. This is especially true for some of the less commonly considered Eley-Rideal reactions and collisional desorption cross-sections. In other cases, the studies are for different surface conditions, different temperatures, and include different reaction phenomena than considered here. In particular, many studies deal with chemisorption and dissociative adsorption, while the main adsorption mechanism in this study is physisorption onto an atomic oxygen monolayer. Regardless of these differences, these values are useful for bounding the parameters used. It is important to note that the significance of the surface event modeling described above to the present work is that it represents a substantial increase in detail from previous work in Ref. [10].

The set of equations is solved using a standard implementation of a fourth order

Runge-Kutta method[96]. As the system is relatively simple in comparison to the types of systems often solved with the Runge-Kutta method, a constant time step is used. An exact quantification of the error of the Runge-Kutta method is not possible[97]. A standard method for choosing the size of the time step is applied. A series of simulations at identical conditions is performed, with the time step being reduced in each subsequent simulation. At a sufficiently small value of the time step, the results of the simulation are insensitive to further reductions. This values is chosen as the appropriate value of the time step. Surface concentration of six species are tracked: N_2, O_2, NO, N, O, and NO_2. Production of gaseous NO_2^* is calculated as well. The required input parameters, which are detailed above, are: incident fluxes, sticking coefficients, thermal desorption times, collisional desorption cross-sections, Eley-Rideal reaction cross-sections and probabilities of product ejection, Langmuir-Hinshelwood reaction rates and probabilities of product ejection, and the density of free surface sites on a clean surface. In simulations including the effects of satellite rotation, the period of rotation is an additional input parameter.

5.1.4 Conversion from Surface Flux to Glow Brightness

In order to make a direct comparison with the VAE data, the emitted flux of NO_2^* must be converted into a glow brightness. The measured glow brightness is given in units of Rayleighs, which is defined as:

$$1 \text{ Rayleigh} \equiv \frac{10^6 \text{ photons}}{\text{cm}^2 \cdot \text{s}}. \tag{5.7}$$

Dimensional considerations suggest a form for the conversion model. First, the simplifying assumption is made that each NO_2^* molecule decays to the ground state and emits a photon within a very short time scale. The lifetime of NO_2^* is reported

to vary with the wavelength of the emission; for the wavelength on the order of 700 nm, the lifetime is approximately 100 μs[98]. Given typical velocities of particles exiting a diffuse surface of about 1000–2000 m/s, this indicates an average distance traveled of 0.1–0.2 m before emission. This distance agrees well with the reported characteristic length of shuttle glow[99]. Since this length is relatively short in comparison to the scale of the ram surfaces in question, a direct conversion from molecules to photons can be made. Second, the probability that an emitted photon has a wavelength within a particular range is given by the ratio of line width area to the total NO_2^* spectrum area (see Figure 5.3). The spectrum used is that of a red-shifted air-glow NO_2^* spectrum. The spectrum of nitrogen dioxide created on the surface and then released into the gas phase is known to be shifted compared to the spectrum of nitrogen dioxide created via a gas-gas collision of NO and O[100, 101, 102]. In the present study, the glow at 656.3 nm and 732.0 nm is considered. The photometer in the VAE experiment has a line width of 2 nm. For these wavelengths, the area ratios are approximately 1/162 and 1/150, respectively. Thus the final conversion is:

$$\text{Flux}\left[\frac{\text{particles}}{\text{m}^2 \cdot \text{s}}\right] \times \left(\frac{\text{Area}}{\text{Ratio}}\right) \times \left(\frac{1}{10^{10}}\right) = \text{Flux [Rayleighs]}. \tag{5.8}$$

5.2 Steady State Analysis

The set of equations used to implement the surface event modeling is given in Eq. 5.6. While this system is non-linear and best solved numerically, as detailed in section 5.1.3, it is advantageous to consider a steady state analysis of a limited

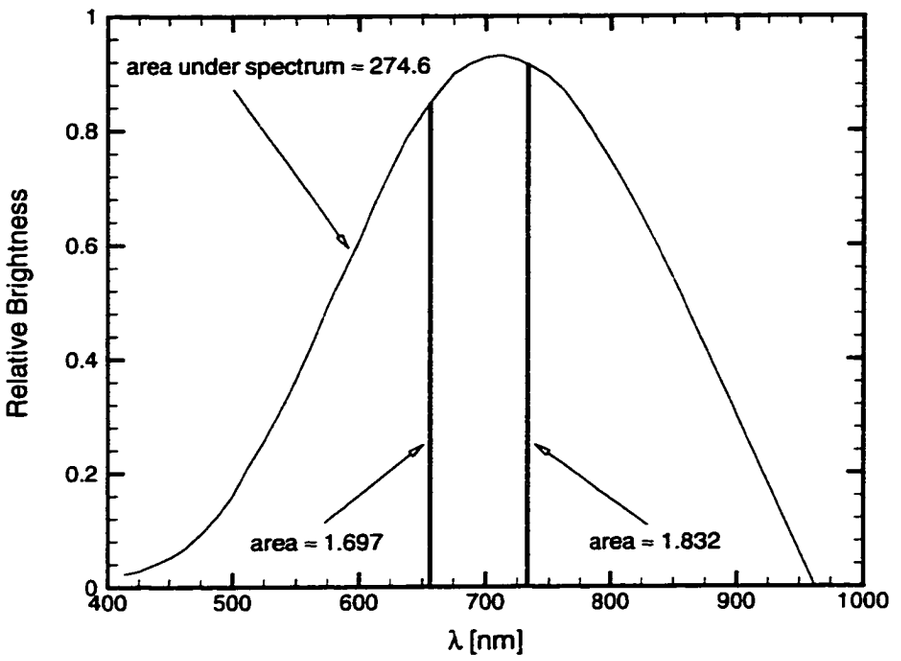

Figure 5.3. NO_2^* Spectrum and Photometer Linewidths

number of terms. For this analysis, all chemical reactions are neglected. The justification is that these reactions are seen as secondary effects that do not dominate the behavior of the species' surface coverages. Two different analyses are considered, one excluding thermal desorption and one with its inclusion.

5.2.1 Balance of Adsorption and Desorption

The first system considered is one with only physical adsorption and collisional desorption. Including the relevant terms from Eq. 5.6 and considering the effects on a single species gives:

$$\frac{d\Theta_A}{dt} = \frac{S_A F_A}{n_s}\left(1 - \sum_{i=1}^{N}\Theta_i\right) - \sum_{i=1}^{N} F_i \Theta_A \sigma_{iq}^{d} \tag{5.9}$$

To further the analysis, this is expressed without the use of summations:

$$\frac{d\Theta_A}{dt} = \frac{S_A F_A}{n_s}(1 - \Theta_A - \Theta_B - \ldots) - \sigma_A F_T \Theta_A, \tag{5.10}$$

where the individual species are labeled A, B, C, etc. The term F_T represents the total flux and is defined as:

$$F_T \equiv F_A + F_B + \ldots, \tag{5.11}$$

and σ_A is short-hand notation for the collisional desorption cross-section for species A.

By definition, at steady state the rate of change of the surface coverage is zero. Therefore:

$$\frac{S_A F_A}{n_s}(1 - \Theta_A - \Theta_B - \ldots) = \sigma_A F_T \Theta_A, \tag{5.12}$$

$$\frac{S_A F_A}{n_s \sigma_A F_T}(1 - \Theta_A - \Theta_B - \ldots) = \Theta_A. \tag{5.13}$$

It is helpful to make two definitions:

$$C_A \equiv \frac{S_A}{n_s \sigma_A} \text{ and } \mathcal{F}_A \equiv \frac{F_A}{F_T}. \tag{5.14}$$

Here, C_A is simply a collection of input parameters relating to species A, while $\mathcal{F}_A$ represents the fractional contribution of species A to the total flux of incident particles. Using these definitions:

$$C_A \mathcal{F}_A(1 - \Theta_A - \Theta_B - \ldots) = \Theta_A, \tag{5.15}$$

$$C_A \mathcal{F}_A(1 - \Theta_B - \Theta_C - \ldots) = \Theta_A(1 + C_A \mathcal{F}_A), \tag{5.16}$$

$$\Theta_A = \frac{C_A \mathcal{F}_A}{1 + C_A \mathcal{F}_A}(1 - \Theta_B - \Theta_C - \ldots). \tag{5.17}$$

To further simplify:

$$K_A \equiv \frac{C_A \mathcal{F}_A}{1 + C_A \mathcal{F}_A}. \tag{5.18}$$

Equation 5.17 becomes:

$$\Theta_A = K_A(1 - \Theta_B - \Theta_C - \ldots), \tag{5.19}$$

and, similarly for the other species,

$$\Theta_B = K_B(1 - \Theta_A - \Theta_C - \ldots), \tag{5.20}$$

$$\Theta_C = K_C(1 - \Theta_A - \Theta_B - \ldots), \tag{5.21}$$

$$\vdots$$

Expressed as a system of equations, this is:

$$\Theta_A + K_A\Theta_B + K_A\Theta_C + \ldots = K_A, \tag{5.22}$$

$$K_B\Theta_A + \Theta_B + K_B\Theta_C + \ldots = K_B, \tag{5.23}$$

$$K_C\Theta_A + K_C\Theta_B + \Theta_C + \ldots = K_C. \tag{5.24}$$

$$\vdots$$

Or, in matrix form:

$$\begin{bmatrix} 1 & K_A & K_A & K_A & K_A \\ K_B & 1 & K_B & K_B & K_B \\ K_C & K_C & 1 & K_C & K_C \\ K_D & K_D & K_D & 1 & K_D \\ K_E & K_E & K_E & K_E & 1 \end{bmatrix} \begin{bmatrix} \Theta_A \\ \Theta_B \\ \Theta_C \\ \Theta_D \\ \Theta_E \end{bmatrix} = \begin{bmatrix} K_A \\ K_B \\ K_C \\ K_D \\ K_E \end{bmatrix}. \tag{5.25}$$

Inverting the coefficient matrix allows for the steady state fractional concentrations of the species to be determined. Such an inversion is trivial using a standard algebraic manipulation software package. The actual numeric values for these concentrations are dependent on the input parameters comprising K_A. Calculated steady state values corresponding to the baseline case are presented in section 8.3.

The analysis here focuses on the analytic nature of the steady state behavior. The coefficients K_X depend on the relative flux, $\mathcal{F}_X$. Furthermore, there is an absence of a direct dependence on the total flux. Thus, the steady state fractional concentrations are directly affected by the relative fluxes of the species, not by the total flux. This has a significant impact on the behavior of the steady state concentrations with altitude. As altitude increases, overall ambient density decreases, accompanied by an decrease in incident flux. Without this analysis, it is reasonable to assume that as the incident flux decreases so will the overall surface coverage. The analysis shows that this is not necessarily the case; it is the relative fluxes that are important. The overall coverage could increase, decrease or remain constant with altitude, depending on the physical parameters.

This perhaps counterintuitive behavior can be viewed as a general balance between adsorption and collisional desorption. As flux increases, the rate of adsorption increases. Counteracting this, as flux increases, the rate of collisional desorption also increases. In effect, the two phenomena compete and as a result the coverages become insensitive to the total incident flux.

5.2.2 Time Scale Analysis

The prior examination of the governing system of equations addressed the steady state surface concentrations. It did not address the time required to reach steady state and hence the inherent time scale of the system. Again, numeric values for this time scale are not important here; it is more useful to consider to which of the input parameters the time scale is sensitive. To this end, the analysis starts with Eq. 5.9 and assumes that the sticking coefficients and collisional desorption cross-sections

are the same for all species. The rate of change of total surface coverage, obtained by adding the respective equations for each species, is:

$$\frac{d\Theta_T}{dt} = \frac{SF_T}{n_s}(1-\Theta_T) - F_T\Theta_T\sigma^d. \tag{5.26}$$

The assumption of identical event parameters for each species allows the equation to be separated. While the subsequent integration is still complicated and will not be included here, examination of the first step is insightful:

$$\frac{d\Theta_T}{\left(\frac{S}{n_s}(1-\Theta_T) - \Theta_T\sigma^d\right)} = F_T dt. \tag{5.27}$$

The right-hand side shows that the time scale of the system depends directly on the total incident flux. The more molecules that strike the surface, the faster the surface concentration builds up and the faster adsorption comes into balance with collisional desorption. This is an important distinction; the steady state values depend on the relative flux, while the time scale of the system depends on the total flux.

5.2.3 Effects of Thermal Desorption

Exclusion of the chemical events in a steady state analysis is defensible. An examination of the terms and baseline input conditions show the chemical effects to be several orders of magnitude less than physical effects. Neglecting thermal desorption is less justifiable. Further insight is gained from a steady state analysis including thermal desorption.

Analogous to Eq. 5.9, an equation describing the rate of change of surface coverage is written for a system with physical adsorption, thermal desorption and

collisional desorption:

$$\frac{d\Theta_A}{dt} = \frac{S_A F_A}{n_s}\left(1 - \sum_{i=1}^{N}\Theta_i\right) - \frac{\Theta_A}{\tau_A} - \sum_{i=1}^{N} F_i \Theta_A \sigma_{iq}^{d} \tag{5.28}$$

Once again, this is expressed without the use of summations:

$$\frac{d\Theta_A}{dt} = \frac{S_A F_A}{n_s}(1 - \Theta_A - \Theta_B - \ldots) - \frac{\Theta_A}{\tau_A} - \sigma_A F_T \Theta_A. \tag{5.29}$$

As before, the derivative is zero under the assumption of steady state and the terms are rearranged:

$$\frac{S_A F_A}{n_s}(1 - \Theta_A - \Theta_B - \ldots) = \sigma_A F_T \Theta_A + \frac{\Theta_A}{\tau_A}, \tag{5.30}$$

$$\frac{S_A F_A}{n_s}[1 - \Theta_A - \Theta_B - \ldots) = \Theta_A\left[\sigma_A F_T + \frac{1}{\tau_A}\right]. \tag{5.31}$$

It is not possible to separate the coefficients into two constants, one comprised solely of fluxes and one expressed in terms of other input parameters. Defining a single coefficient term does simplify the analysis:

$$D_A \equiv \frac{S_A F_A}{n_s\left[\sigma_A(F_A + F_B + \ldots) + \frac{1}{\tau_A}\right]}. \tag{5.32}$$

Equation 5.31 becomes:

$$D_A(1 - \Theta_A - \Theta_B - \ldots) = \Theta_A, \tag{5.33}$$

$$\Theta_A = \frac{D_A}{1 + D_A}(1 - \Theta_B - \Theta_C - \ldots). \tag{5.34}$$

Similar to the previous analysis, another coefficient term is defined:

$$K_A \equiv \frac{D_A}{1 + D_A}. \tag{5.35}$$

Consideration of all the species results in a matrix equation of the exact same form as Eq. 5.25. The identical solution method is of course valid.

The differences in the solution lie in the definitions of K_X and, ultimately, D_X. To gain physical insight into the behavior, D_X is expressed in a different form:

$$\begin{aligned} D_X &= \frac{S_X F_X \tau_X}{n_s[\tau_X \sigma_X F_T + 1]}, \\ &= \frac{S_X \tau_X \mathcal{F}_X}{n_s[\tau_X \sigma_X + \frac{1}{F_T}]}, \qquad (5.36) \\ &\propto \frac{\alpha \mathcal{F}_X}{\beta + \frac{1}{F_T}}. \qquad (5.37) \end{aligned}$$

Constants of proportionality α and β are used to focus on the key characteristics of the relation. From Eq. 5.37, the matrix elements, and hence the surface coverage, are shown to depend on both the relative flux and the total flux.

Unlike the case without thermal desorption, the steady steady surface concentrations are dependent on the total flux. This effect also has a physical explanation. The initial analysis shows that regardless of the total flux, the surface concentrations approach the same values. The rate of thermal desorption varies directly with the surface concentrations and is unaffected by the flux. Replacing these thermally desorbed particles occurs with a greater frequency with a greater flux. An alternative way of thinking of this is that the time scale of the system is shorter with a greater flux, and thus the system can more readily adapt to the perturbation caused by thermal desorption.

Chapter 6

Computational Considerations

An overview of the solution method is given in Section 1.3. Individual treatments of the numerical techniques employed in the solution procedure are presented in Chapters 3–5. Use of these techniques requires a number of issues to be considered. These issues include determining both input and control parameters and efficiently using computational resources. A discussion of these issues forms a basis for this chapter.

6.1 DSMC Simulations

As is discussed previously, the DSMC method is chosen to simulate the flow field around glow-producing surfaces. Given the rarefied nature of these flow fields, it is expected that a large spatial domain is necessary to resolve the relevant features. Coupled with the added difficulty of tracking rare species, the spatial scope of the simulations dictates that the DSMC method requires the greatest computational effort of all the techniques of the solution procedure. This section deals with the

determination of the input parameters for the DSMC simulations, a description of the decomposition of the spatial domain, and computational efficiency issues as they relate to the DSMC method.

6.1.1 Atmospheric Composition and Temperature

Section 2.5.2 gives an overview of the nature of the atmospheric composition in the altitude range considered here. The concentration of a majority of the atmospheric constituents is determined using the Mass Spectrometer Incoherent Scatter (MSIS) neutral atmosphere model[39]. The MSIS model describes the overall temperature and the number densities of N_2, N, O_2, O, He, Ar, and H. Of these species, nitrogen and oxygen are present in significant quantity to be important in this study. The other species have a lower relative concentration and are not involved in the chemical path leading to glow production.

The MSIS model uses a number of parameters as input, including latitude, longitude, time of year, local time of day, solar activity and the magnetic activity of the Earth. It is difficult to correlate any of these parameters with conditions experienced by an orbiting vehicle. For example, data from the Atmosphere Explorer satellite were taken over a period of several years. During this time, the satellite clearly changed geographic position. Furthermore, solar and magnetic activity varied significantly over this time period. It is not practical, therefore, to attempt to match the input conditions to the MSIS model to the actual conditions experienced by the satellite. Instead, the model is used to generate a reasonable sample atmosphere. For reference, the input conditions to the MSIS model are given in Table 6.1. These conditions match the planned re-entry point of the Skipper satel-

Table 6.1. Input Parameters to the MSIS Model

Day	196
Year	1995
Local Time	12 hours
Latitude	23°N
Longitude	164°E
3 Month Average of $F_{10.7}$ Flux	101.69
Daily $F_{10.7}$ Flux	101.69
Daily Magnetic Index, Ap	14.33

lite. Figure 6.1 shows variation of number densities of both molecular and atomic nitrogen and oxygen in the MSIS-generated atmosphere. There is an increase in relative concentration of atomic nitrogen with altitude. Conversely, there is a decrease of molecular oxygen. At lower altitudes, molecular nitrogen is the dominant species; at the higher altitudes atomic oxygen dominates. Characteristics of the atmospheric structure are examined in Section 2.5.2 with discussions of Figure 2.6.

Nitric oxide is the one species critical to glow production whose ambient concentration is not predicted by the MSIS model. As explained in Section 2.5.2, NO is part of the odd-nitrogen cycle in the atmosphere. Its concentration is very sensitive to atmospheric and other conditions; prediction by an analytic model is correspondingly very difficult. However, for the accurate calculation of glow production, some reliable estimate of ambient NO concentration must be made. Values are taken from measurements of the Neutral Atmosphere Composition Experiment (see Section 2.1.2). As is expected, the measurements of NO density from NACE show a

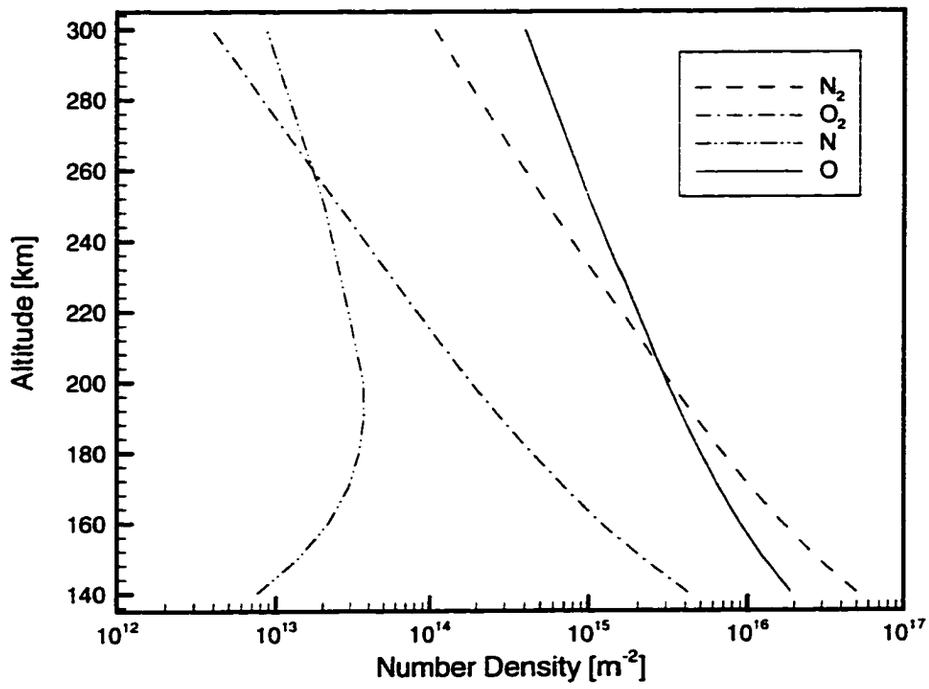

Figure 6.1. Variation of Species Number Densities with Altitude

large amount of variation. At each altitude of interest, a lower and upper bound is determined from the NACE data. Thus, two DSMC simulations are performed at each altitude; one uses the lower NO concentration, the other the higher concentration. These values are presented in Figure 6.2. Also presented in the figure is an estimation of the variation of NO number density based on an analysis of the theoretical scale height. While only an approximation, comparison of the the scale height estimate with the NACE data shows that at the upper altitudes the measured values are greater than what is predicted by theory.

The ambient temperature at each altitude is taken directly from the MSIS model. Values for these temperatures are given in Table 2.1. There is a direct increase in temperature with altitude, as is expected in the thermosphere. Together, the

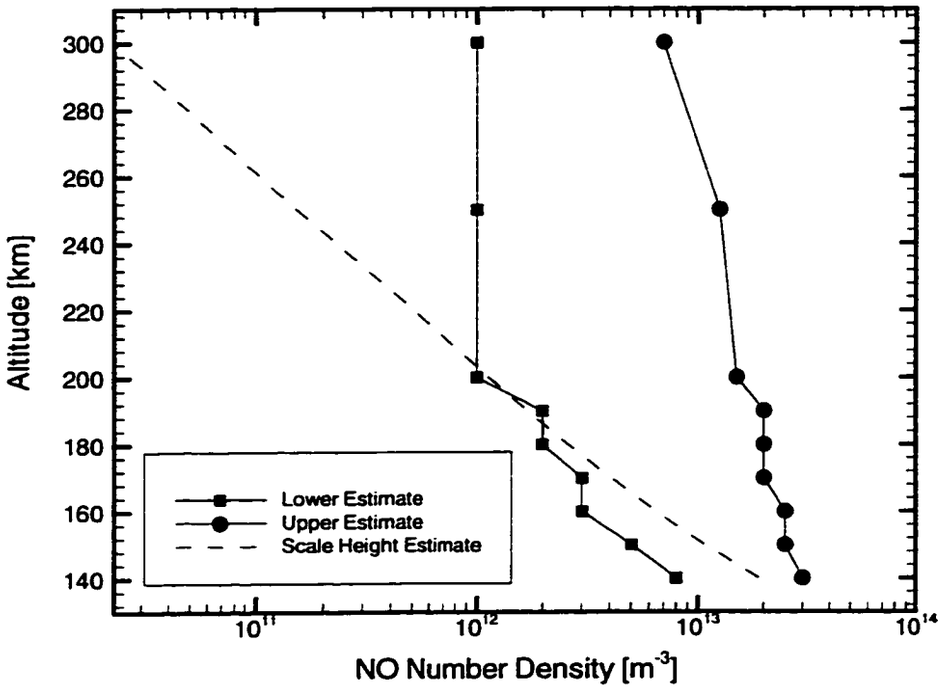

Figure 6.2. Ambient NO Concentrations Measured by NACE

temperature and individual number densities serve as the input parameters to the DSMC simulations.

6.1.2 Source-Term Chemistry Reaction Cross-Sections

Section 4.2.2 describes the method of including the effects of common species chemical reaction in the overlay simulations. The formulation used requires the determination of collision cross-sections for the reactants in question. Two different means are used to determine the cross-sections. With the first approach, the values are approximated from experimental measurements[103]. In the second approach, the cross-sections are obtained from a molecular dynamics trajectory analysis[81]. The trajectory analysis is considered to give more accurate cross-sections. Thus the first

Table 6.2. Source-Term Chemistry Reaction Cross-Sections

Reaction Number	Experimental Estimate 10^{-22} m^2	Trajectory Estimate 10^{-22} m^2
4.5	4.0	10.25
4.6	6.0	33.9
4.9	n/a	381
4.10	n/a	390

approach was not used for all source-term reactions. Cross-sections determined for all source term reactions are given in Table 6.2.

6.1.3 Domain Decomposition

As dictated by the DSMC method, the spatial domain is decomposed into a number of individual cells. Typically, these cells are sized based on the local mean free path in the flow. An examination of the mean free path values in Table 2.1 shows that this a partially unacceptable choice. The mean free paths are too large to form a useful basis for the cell size in all areas of the domain. Near the satellite body, the local mean path is shorter as the gas molecules build up in front of the ram surface. These values are used in determining the cell size. Away from the body, the cell size is set to a constant value. This size is chosen to give reasonable resolution without unacceptable computational costs. Two different grids are used–one for the altitudes below 200 km and one for 200 km and above altitudes. The two grids are shown in Figures 6.3 and 6.4, respectively. The lower altitude grid has 215 cells and the upper altitude grid contains 86 cells. In both cases the advancing front

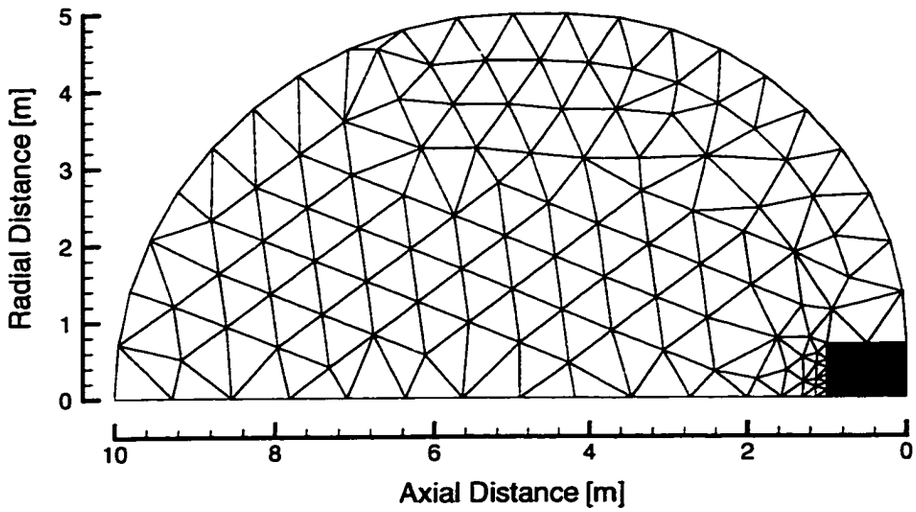

Figure 6.3. Computational Grid for Altitudes Below 200 km

method[104] is used to calculate the actual location of the cell nodes to generate the grids.

All of the simulations performed using the two grids are axisymmetric, with the x-axis used as the axis of symmetry. The actual geometry of the AE flow field is not axisymmetric—it is fully three-dimensional. This is due to the fact that the spin axis of the satellite is perpendicular to the velocity vector. For the simulations of the AE satellite, a cylindrical body is used to represent the satellite. The cylinder has an area chosen to match the area of the actual satellite as seen by the incident flow. While obviously an approximation, it is a necessary and acceptable one. A fully three-dimensional calculation would carry a significantly higher computational cost. The rarefied nature of the flow field suggests that the differences in glow

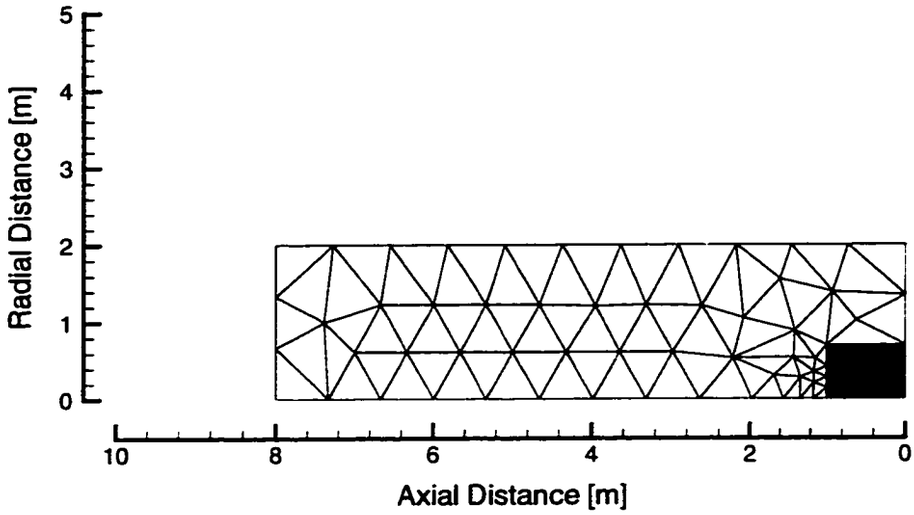

Figure 6.4. Computational Grid for Altitudes At 200km or Greater

brightness between an axisymmetric and three-dimensional simulation would be insignificant. The flow field around the space shuttle is also three-dimensional in nature. Simulation of this complex geometry is beyond the scope of the present work. The same axisymmetric grid is used for the shuttle simulations. In essence, the conditions around the shuttle tail are simulated using a cylindrical test plate. The flow field around the shuttle is nearly collisionless, thus this approximation is again acceptable.

Two different grids are used because the overall number density drops significantly with altitude. At the lower altitudes, the density is high enough that the flow is collisional. The relatively large domain is used to capture the flow structure that develops from the collisions. A comparatively smaller domain is used for the

higher altitudes. Under these conditions, the flow is nearly collisionless and there is not much of a discernible structure. The most important spatial constraint at the upper altitudes is that the region with significant source term chemistry (see Section 4.2.2) is included. This chemistry occurs in a region in front of the ram surface, where the bimodal nature of the velocity distribution is most severe. A more complete discussion of this is found in Section 7.2.

6.1.4 Computational Performance

The DSMC simulations are performed using a scalar-optimized, parallelized code (MONACO)[105]. The base MONACO code is modified to perform a DSMC overlay as described in Chapter 4. The code is capable of running on an arbitrary number of processors. Details of the design and implementation of the MONACO code are to be found in the listed reference, and the modifications made to allow for the overlay do not significantly impact the optimization schemes of the code.

The main impact on the code performance is a vastly increased memory requirement. The velocity and energy distributions that are stored in each cell for every species (see Section 4.2.1) require a large amount of memory. Efforts are made to store the distributions in an efficient manner. Despite this, the increase in the memory usage is very significant. In the worst case, an overlay simulation requires five times the memory of a comparable, standard DSMC simulation. This puts a stronger constraint on the hardware that can be used to perform an overlay calculation. Furthermore, saving the distribution data to disk has a noticeable effect on the simulation time. Because the distributions are maintained for each cell, the increase in memory usage scales directly with the number of cells in the domain.

The reduction in the number of cells in the upper altitude grid thus results in a large savings in the memory used by the simulations.

For most of the cases, the code is run on an IBM SP-2 parallel super computer. Four nodes are used to track approximately 250,000 particles. Typically, more particles can be assigned to each processor. The memory overhead of the overlay method requires that the cells be divided among the individual processors. In base simulations a performance of 5.8 μs/particle/timestep during the transient phase and of 7.5 μs/particle/timestep during sampling is achieved. In overlay simulations, the performance is 12.0 μs/particle/timestep and 14.5 μs/particle/timestep during the transient and sampling phases, respectively. The increased time per particle during the overlay simulation indicates the computational overhead of creating temporary particles from the recorded distributions. Overall, the wall clock time for each simulation is on the order of a few hours.

6.2 Surface Event Modeling

The set of surface events is described in differential form in Section 5.1. The Runge-Kutta method is employed to solve the system of equations; the details of the implementation are given in Section 5.1.3. This section provides a listing of all the parameters controlling the surface events. A discussion of the issues involved to model the effects of satellite rotation is also included.

6.2.1 Event Parameters

The model of the surface events is controlled by a large number of parameters. In particular, adsorption is described by a sticking coefficient, thermal desorption by a characteristic time, collisional desorption and gas-surface reactions by cross-sections and surface-surface reactions by a reaction rate. Values for these parameters are taken from a report by Gorelev[83]. Independent sources for these values are presented in Section 5.1.3. Numerical values for these parameters are given in Table 6.3 for non-reacting events, and Table 6.4 for reacting events. All of the events are numbered and labeled for reference in the following chapters.

6.2.2 Satellite Rotation

Aside from the the input parameters detailed above, the Runge-Kutta simulation requires as input incident fluxes for each of the species. Values for these fluxes are determined from the overlay DSMC simulations. Accounting for the spin of the Atmosphere Explorer satellite requires a small modification to the solution procedure. These base fluxes are modified by a piece-wise function consisting of a sinusoidal term for the forward half of the rotation and a null term for the back half of the rotation. This has the overall effect of reducing the total flux to the surface in comparison to the despun case. The sinusoidal term represents the increase in flux as the ram surface rotates into the direction of the velocity vector and an equal decrease as it rotates away. The null term represents the half period that the ram surface spends in the shadow of the satellite body. A visual representation of this, is found in Figure 2.2. The period of the rotation is fixed at 15 s to match the actual rotational period of the AE satellite (see Section 2.1.1).

6.3 Uncertainties and Assumptions

Throughout the discussion of the methods used to calculate spacecraft glow a number of simplifying assumptions are made. Furthermore, some fundamental uncertainties in the process are indicated. It is insightful to restate these uncertainties and assumptions. From this, a better understanding of the relationship between the real world phenomena and the simulation method is gained.

A primary uncertainty exists in determining the ambient atmospheric conditions experienced by the ram surface. This is a two-fold problem. First, the atmospheric model predicts different conditions based on a variety of parameters. Given that the available experimental glow data has been taken over a long period of time and in a multitude of locations, it is impossible to exactly recreate the ambient conditions using an analytical model. Furthermore, experimental measurements of the ambient conditions taken concurrently with the glow measurements are rarely exhaustive enough to provide a profile of the required detail. Second, the concentration of nitric oxide is highly sensitive to many atmospheric parameters. Thus, it is fundamentally difficult to model the nitric oxide density analytically. For this work, direct measurements of the NO density are used. The measurements themselves have a large scatter and are taken as only bounds on the likely nitric oxide concentration.

In flow fields leading to glow production, some of the chemical species are present only in low quantities. These rare species are difficult to simulate accurately. The method developed here is the DSMC overlay method and, as implemented, relies on several assumptions. First and foremost is the assumption that the general nature of the flow field is determined exclusively by the common species. This allows for the

base simulation to be performed while disregarding the rare species. Second, three independent velocity distributions are recorded for each common species during the base simulation. It is assumed that these distributions are uncorrelated. This prevents the complexity of the stored distributions from becoming unmanageable. A third assumption is made in the mechanics of the common-rare collisions. In these collisions, a common particle is created from the stored distributions, affects the momentum and energy of the rare particle and is then destroyed. This mechanism does not conserve momentum or energy. It is assumed that effects of these collisions represents the common-rare interactions in the real flow. Finally, production from rare chemical events is modeled via a source term. An average value for the reactant energy is used in these reactions. While this is obviously an approximation, the source term production is a key element in the overall solution procedure.

An axisymmetric domain is used, despite the fact that the actual domain includes three-dimensional effects. The rarefied nature of the flow field presumably justifies such an assumption. The glow predictions from a full three-dimensional simulation would not differ from the axisymmetric prediction to a large enough extent to justify the increased computational cost.

All of the surface events are assumed to occur on top of a monolayer of chemically adsorbed atomic oxygen. This dictates that all adsorption events are physical, as the chemically adsorbed oxygen is not available for further reactions. Parameters taken from experiments for each and every event are not available. Quite simply, each of the events has not been studied in detail. The parameters that are used are taken from experiments with different conditions, such as clean surfaces, and that allow for additional types of events such as chemical or dissociative adsorption.

Furthermore, the temperature of the surface is implicitly assumed in the parameters as used. Many of the experimental measurements of these parameters are taken at varying surface temperatures. The parameters used, while not identical to the conditions of the simulation, are taken from experiments that most closely match the simulation conditions.

A simple analytical model is used to convert between emitted nitrogen dioxide flux and glow brightness. This model assumes that the excited nitrogen dioxide emits a photon instantaneously. In reality, the excited molecule has a finite lifetime before it emits. Given the reported short lifetime of NO_2^*, the effects of this assumption are minimal. The model neglects any effects of the spatial distribution of the emitting molecules and the geometry of the photometer. Finally, the frequency of the glow is determined probabilistically from measured spectra of glow. These spectra, as measured quantities, have there own inherent sources of error.

Despite the large number of assumptions and uncertainties described here, the solution procedure is a very detailed treatment of spacecraft glow. Particle properties are tracked down to the molecular level, which is a necessity in such rarefied flows. Rare, yet important, chemical species are also simulated with good statistical accuracy. A complex set of surface events is time-accurately modeled. The effects of satellite rotation are included. The frequency of the simulated glow is matched to experimental spectra. Overall, this represents a highly detailed procedure that is necessary to capture the behavior of spacecraft flow.

Table 6.3. Non-Reacting Events

Physical Adsorption Events	**S**	
$\vec{N}_2 + X \rightarrow N_2^a$	0.03	(e1)
$\vec{O}_2 + X \rightarrow O_2^a$	0.03	(e2)
$\vec{NO} + X \rightarrow NO^a$	0.3	(e3)
$\vec{N} + X \rightarrow N^a$	0.3	(e4)
$\vec{O} + X \rightarrow O^a$	0.3	(e5)
Thermal Desorption Events	τ_d [s]	
$N_2^a \rightarrow \overleftarrow{N}_2 + X$	0.25	(e6)
$O_2^a \rightarrow \overleftarrow{O}_2 + X$	0.25	(e7)
$NO^a \rightarrow \overleftarrow{NO} + X$	25.00	(e8)
$N^a \rightarrow \overleftarrow{N} + X$	25.00	(e9)
$O^a \rightarrow \overleftarrow{O} + X$	25.00	(e10)
$NO_2^a \rightarrow \overleftarrow{NO}_2 + X$	25.00	(e11)
Collisional Desorption Events	σ^d [m^2]	
$\vec{M} + N_2^a \rightarrow \overleftarrow{N}_2 + \overleftarrow{M} + X$	1.0×10^{-19}	(e12)
$\vec{M} + O_2^a \rightarrow \overleftarrow{O}_2 + \overleftarrow{M} + X$	1.0×10^{-19}	(e13)
$\vec{M} + NO^a \rightarrow \overleftarrow{NO} + \overleftarrow{M} + X$	4.5×10^{-20}	(e14)
$\vec{M} + N^a \rightarrow \overleftarrow{N} + \overleftarrow{M} + X$	4.5×10^{-20}	(e15)
$\vec{M} + O^a \rightarrow \overleftarrow{O} + \overleftarrow{M} + X$	4.5×10^{-20}	(e16)
$\vec{M} + NO_2^a \rightarrow \overleftarrow{NO}_2 + \overleftarrow{M} + X$	4.5×10^{-20}	(e17)

Table 6.4. Reacting Events

Eley-Rideal Reactions	σ^{er} [m^2]	
$\vec{N}_2 + O^a + X \rightarrow NO^a + N^a$	2.7×10^{-22}	(e18)
$\vec{O} + N^a \rightarrow NO^a$	3.6×10^{-20}	(e19)
$\vec{N} + O^a \rightarrow NO^a$	3.6×10^{-20}	(e20)
$\vec{O} + NO_2^a \rightarrow NO^a + \overleftarrow{O}_2$	1.0×10^{-20}	(e21)
$\vec{N} + O^a \rightarrow \overleftarrow{NO}^* + X$	2.5×10^{-21}	(e22)
$\vec{O} + N^a \rightarrow \overleftarrow{NO}^* + X$	2.5×10^{-21}	(e23)
$\vec{O} + NO^a \rightarrow NO_2^a$	1.0×10^{-21}	(e24)
$\vec{NO} + O^a \rightarrow NO_2^a$	1.0×10^{-21}	(e25)
$\vec{NO} + O^a \rightarrow \overleftarrow{NO}_2^* + X$	1.0×10^{-21}	(e26)
$\vec{NO} + NO^a \rightarrow \overleftarrow{NO}_2^* + N^a + X$	1.0×10^{-21}	(e27)
$\vec{O} + NO^a \rightarrow \overleftarrow{NO}_2^* + X$	1.0×10^{-21}	(e28)
$\vec{O} + O^a \rightarrow \overleftarrow{O}_2 + X$	4.5×10^{-20}	(e29)
Langmuir-Hinshelwood Reactions	**K^{lh}** [m^2]	
$O^a + N^a \rightarrow NO^a + X$	5.0×10^{-23}	(e30)
$N^a + N^a \rightarrow \overleftarrow{N}_2 + 2X$	5.0×10^{-23}	(e31)
$O^a + O^a \rightarrow \overleftarrow{O}_2 + 2X$	5.0×10^{-23}	(e32)
$O^a + NO^a \rightarrow \overleftarrow{NO}_2^* + 2X$	5.0×10^{-23}	(e33)

Chapter 7

Flow Field Results

While the ultimate goal of the present work is to calculate glow brightness and compare with experimental measurements, a wealth of other results is produced during the multi-step solution procedure. Analysis of these results allows for a better understanding of the precursor steps leading to glow production. Specifically, sensitivity to the various input conditions and controlling parameters is assessed. Examination of the precursor results is critical to understanding the strengths and weaknesses at each step of the simulation procedure.

The overlay DSMC method allows for the simulation of the rarefied flow field around ram surfaces that typically leads to glow production. This chapter examines the general structure of these flow fields through the study of macroscopic variables. Additionally, the microscopic structure of the flow fields is analyzed, with an examination of recorded distribution functions.

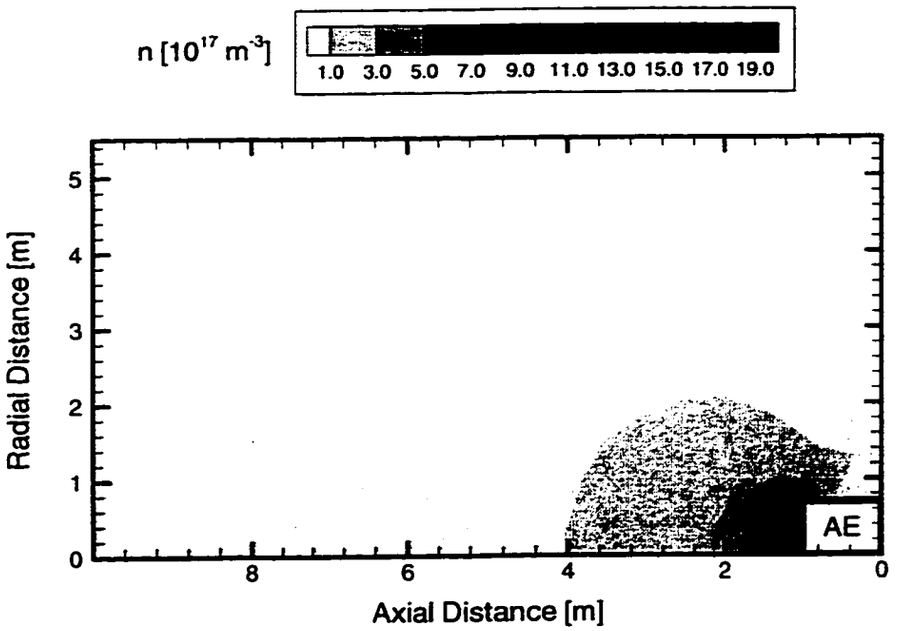

Figure 7.1. Bulk Species Number Density at 140 km

7.1 General Structure

From the previous discussions of the rarefied nature of the typical glow producing flow fields, large and diffuse structures are expected. The first altitude to be considered is 140 km, the lowest altitude of the studied range. Consistent with the assumption that allows for an overlay method in general, the behavior of the common species is assumed to determine the overall structure of the flow field. Figure 7.1 shows a contour plot of the number density of the bulk gas around the Atmosphere Explorer satellite at an altitude of 140 km. No evidence of a shock is visible. An increase of density by over an order of magnitude is present in front of the ram surface of the simulated AE geometry. Even in this region, the mean free

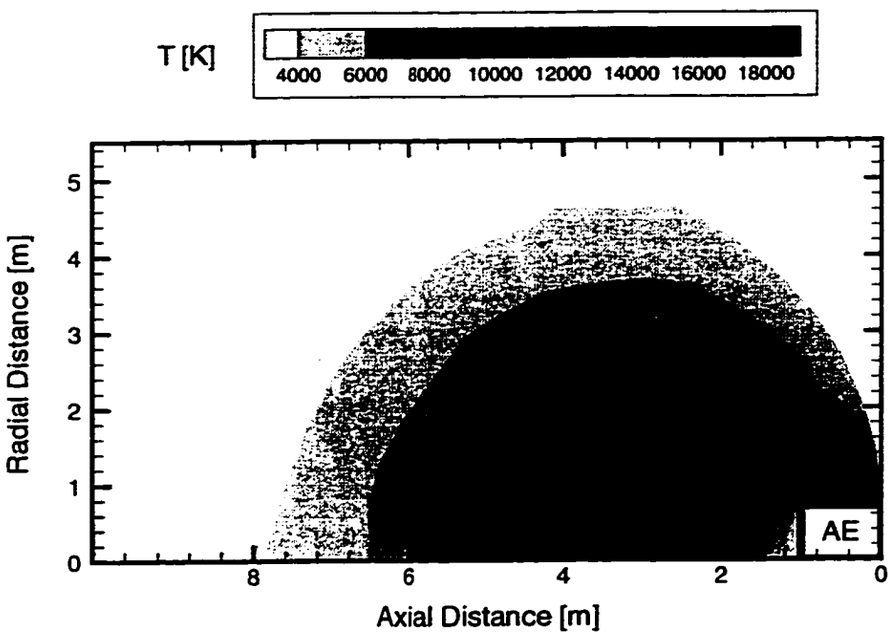

Figure 7.2. Bulk Species Translational Temperature Density at 140 km

path is large enough that collisions are relatively rare. Irregularities in the density contours are due to the coarseness of the grid. An increase in the number of cells would allow for smoother contours at the expense of computational effort. Accuracy to this degree is not required and therefore is not pursued to save computational cost.

A contour plot of the translational temperature for the same flow field at the same conditions is presented in Figure 7.2. The limited significance of temperature is discussed in Section 2.5.1. Regardless, several useful observations about the temperature structure can be made. First, compared to temperature shocks at continuum densities, the shock is extremely diffuse. There is not a sufficient number of collisions to define a sharp shock structure, as is expected in rarefied flows.

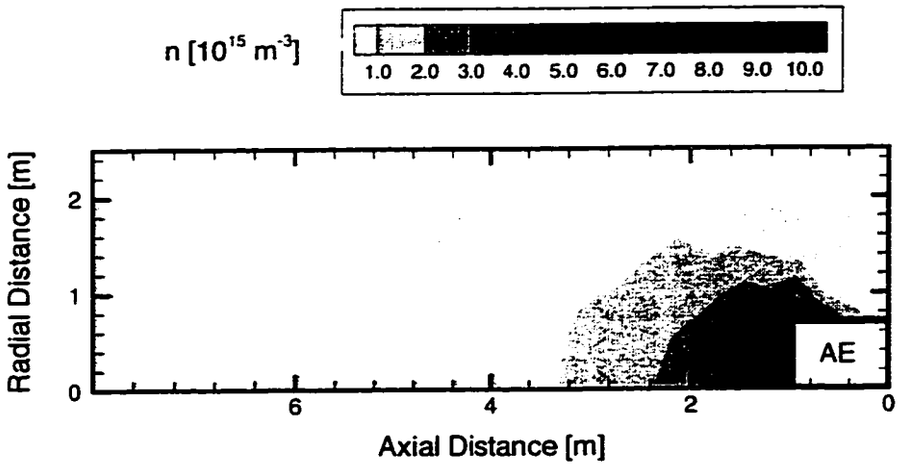

Figure 7.3. Bulk Species Number Density at 300 km

Second, the region of the highest temperature indicates the area of the flow field with the largest number of high energy collisions. This will become evident in an analysis of the velocity distribution functions in this region, presented in Section 7.2. It is in this region that a predominant portion of the source term chemistry occurs.

While similar in structure, the flow field at 300 km is included for completeness. This flow field represents the structure at the upper regime of the altitude range considered. As with the lower altitude, the macroscopic values for the bulk gas are used. Number density contours are given in Figure 7.3. The relative increase in density before the ram surface of the satellite is slightly less than in the lower altitude case. An increase of just under an order of magnitude is seen. Other than that difference, the general density structure at the two altitudes, and thus over the

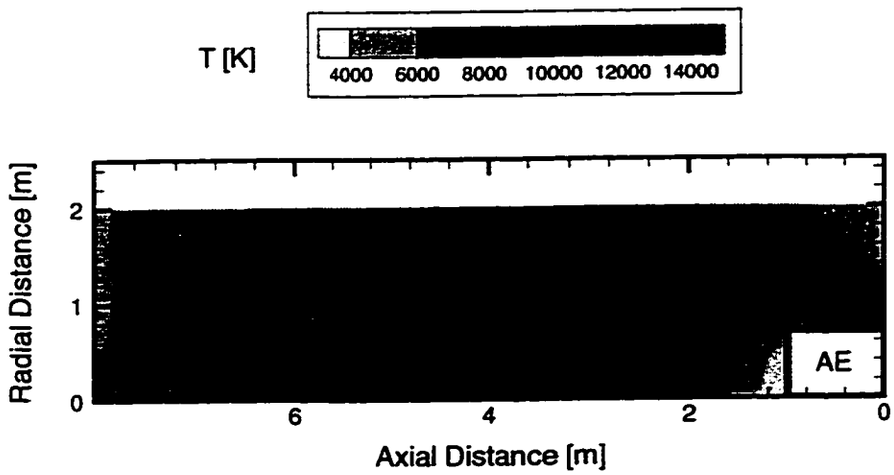

Figure 7.4. Bulk Species Translational Temperature at 300 km

entire range considered, is similar.

Translational temperature contours are shown in Figure 7.4. While visibly disparate, the behavior of the weak temperature shock is very similar at 300 km to the behavior at 140 km. The apparent difference is caused by the reduced spatial extent of the computational grid so that the top portion of the diffuse bow shock is not captured. The lack of this feature is of no importance, because that portion of the flow field has a negligible effect on the ram surface. The justification is that the flow field is essentially collisionless. What is viewed as a temperature shock is actually two families of particles passing by each other. Molecules that reflect off the ram surface have no opportunity to undergo a collision and interact again with the ram surface. Even production through source term chemistry is limited. In general,

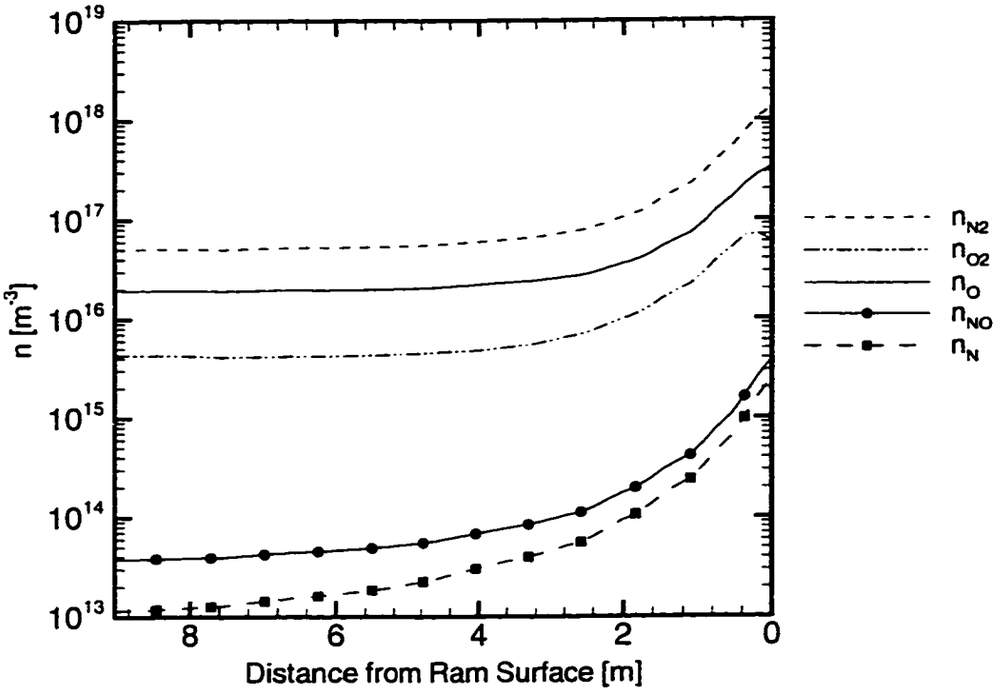

Figure 7.5. Number Density Variation Along the Stagnation Streamline at 140 km

molecules created via the source term chemistry have a velocity biased in the radial direction. Thus, the few particles created in the region of high collision energy that is above the portion included on the truncated grid, do not have sufficient radial velocities to impinge on the ram surface.

The previous plots of number density depict the behavior of the bulk gas. Trends of the number densities of the individual species are also of interest. Figure 7.5 shows the density variation of all species along the stagnation streamline at 140 km. At this altitude NO and N are the rare species. Accordingly, values for their density have been taken from the overlay simulation at 140 km. Their density curves are marked with symbols in order to distinguish them from the common species density. Throughout the entire range, the concentration of the rare species is indeed at least

twenty times less than the least abundant common species. Thus, the assumption that the rare species are rare throughout the flow field is a valid one. Two other features are of note. First, the rate of increase near the ram surface of the density of the rare species is greater than that of the common species. The difference is attributed to the creation of NO and N through the source term chemistry. Despite this additional source, the rare species remain rare even near the ram surface. This supports the assumption that chemical production does not affect the rarity of an individual species. Second, the density of O_2 decreases just before the ram surface. In this region, the overall density is higher, resulting in more collisions. The increased number of collisions leads to more dissociation reactions of molecular oxygen. The density of atomic oxygen is significantly greater than that of molecular oxygen, thus the effects of dissociation are not visible in the atomic oxygen density profile.

7.2 Velocity Distributions

An analysis of the microscopic behavior of the flow field is also insightful. The axial velocity distribution functions of nitric oxide are examined. Furthermore, the sensitivity to the different source term chemistry reaction cross-sections is studied (see Section 6.1.2). Comparison of the effects of the two reaction cross-sections tested is most appropriately studied at the lowest altitude considered, 140 km. At this altitude, the base flow field density is the highest, and therefore the effects of changing the cross-section are the most noticeable. Figures 7.6 – 7.9 compare the nitric oxide axial velocity distributions for two different cross-sections at 140 km at four points in the flow field. The four points chosen are: (1) the inflow cell along

the axis approximately 10 m from the front of the satellite; (2) a mid-flow field cell approximately 3 m from the surface on the axis; (3) the last cell before the wall on the axis; (4) and on the ram surface of the satellite itself.

Figure 7.6 compares the axial velocity distribution in the inflow cell along the axis. In both cases, two distinct groups of particles are evident. The group with the high, positive axial velocity represents free stream particles moving towards the satellite at orbital speeds. The other represents particles that have collided with the front face of the satellite and are moving away with a negative axial velocity. Given the extremely rarefied conditions, these particles travel throughout the entire flow field without undergoing collisions. Note that the relative frequency of particles in the rebounded group is larger with the second, larger cross-sections (σ_2). With the larger cross-section. more particles are created throughout the flow field due to the source chemistry. A majority of these particles also collide with the surface, rebound and are sampled in the inflow cell with a negative axial velocity.

A comparison of the axial velocity distributions in the mid-flow field cell on the axis is presented in Figure 7.7. The two groups evident in the inflow cell are also seen here. It is in this region that a majority of the source term chemistry occurs. The relative increase of the negative axial velocity group with the second cross-section is also apparent. In addition to these groups, two smaller groups are distinguishable. Noticeably smaller in magnitude than the first two groups, these can be seen at an axial velocity of about 5 km/s. These groups represent the particles created through the source term chemistry that have yet to collide with the AE satellite. The two peaks in this grouping show the difference in the center of mass velocity in the two source term reactions. When an N_2 molecule traveling at orbital speed collides with

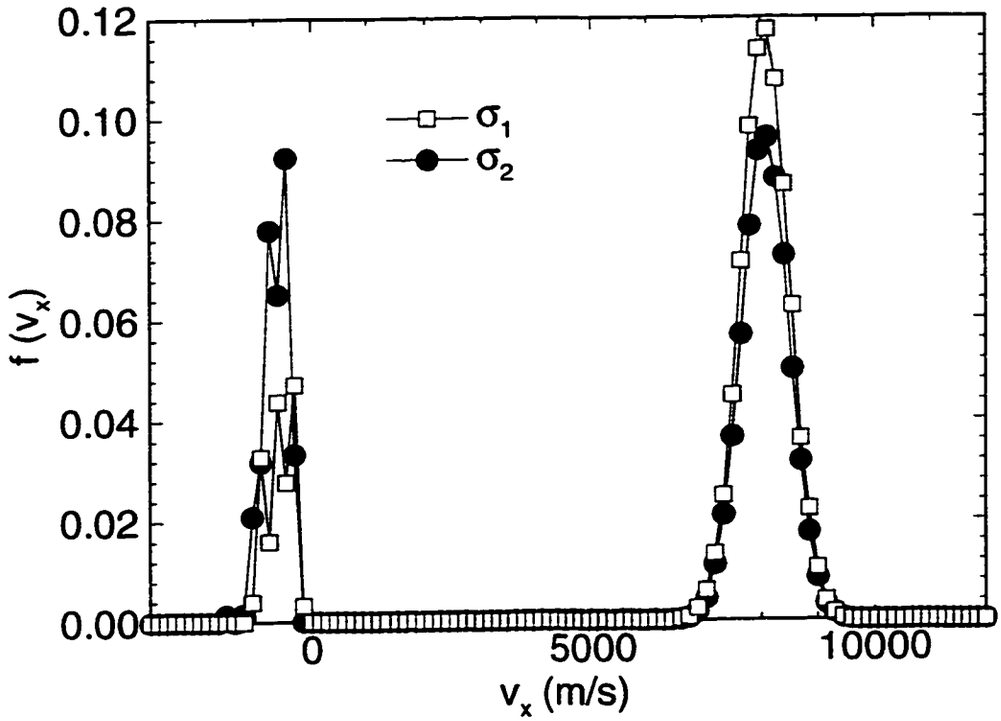

Figure 7.6. Axial Velocity Distribution Functions at the Inflow

a reflected oxygen atom, the center of mass velocity is larger than when the atomic oxygen is traveling at orbital speed and collides with a reflected N_2 molecule.

Near the wall, the comparison between the distributions is noticeably different. In both cases shown in Figure 7.8, the distribution is dominated by a group of reflected particles, moving in the negative axial direction with a relatively slow speed. The form of these distributions is consistent with the number density profiles. The magnitude of the velocity of the rebounding particles is relatively small, so that it will take a much longer time for these particles to leave the cell than it will for the high speed free stream particles in the opposite direction. Consequently, at any time there are many more reflected particles than free stream particles in cells near the surface. As was noted previously, due to a lack of gas-gas collisions, very few of

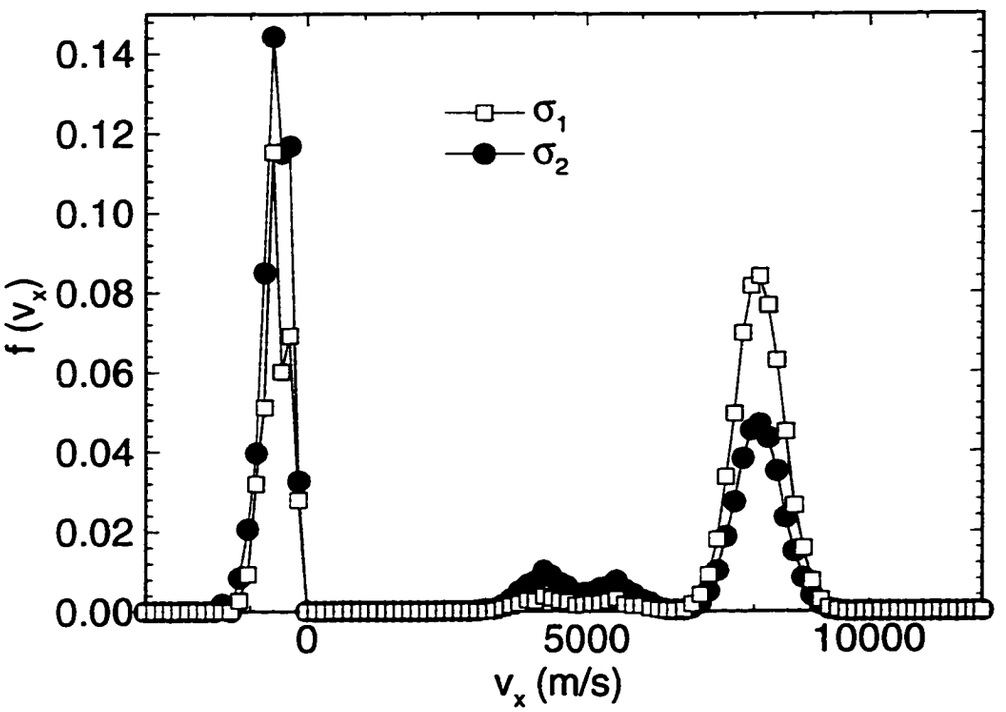

Figure 7.7. Axial Velocity Distribution Functions in the Middle Flow Field

these particles ever collide and strike the surface again.

The final comparison of the effects of changing the reaction cross-section is given in Figure 7.9 which shows distributions of the normal velocity component along the ram surface of particles striking the wall. The appearance of these distributions is remarkably different than those sampled near the wall. This is due to the absence of the peak representing the reflected particles that dominated the previous distributions. In the distributions for both of the cross-sections, the presence of source term NO as well as free stream NO is evident. Also distinguishable is the bimodal behavior of the source term particles. Once again, the increased importance of the source term chemistry is visible; the distribution obtained using the second set of cross-sections is heavily weighted towards these particles. The predominance of

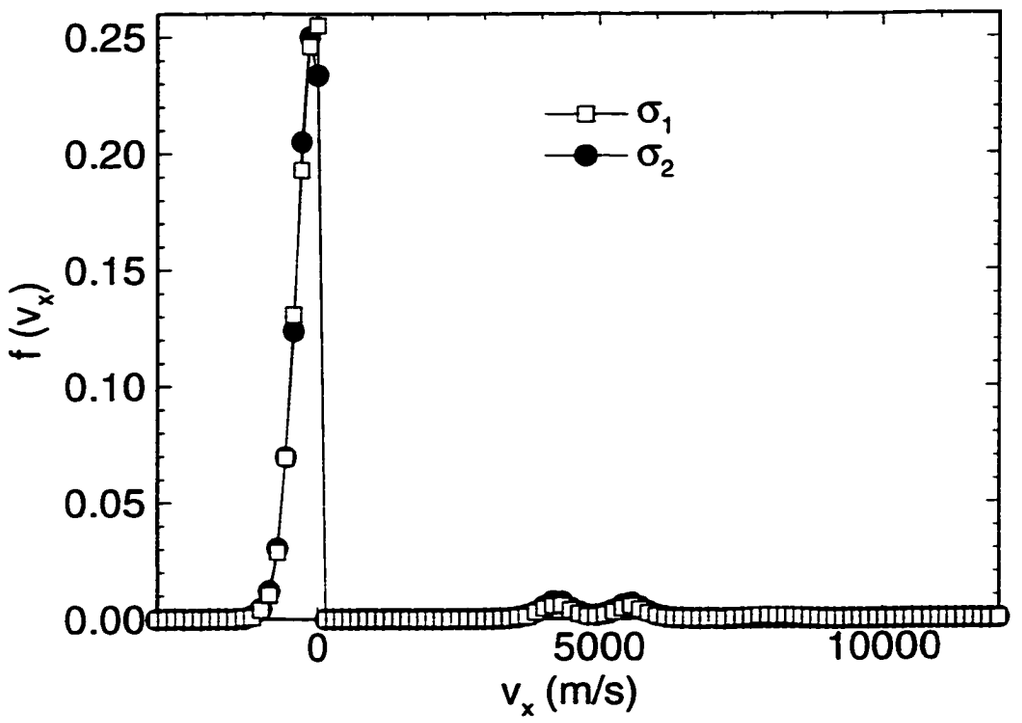

Figure 7.8. Axial Velocity Distribution Functions Near the Wall

source term particles is so large enough to greatly overshadow the free stream peak.

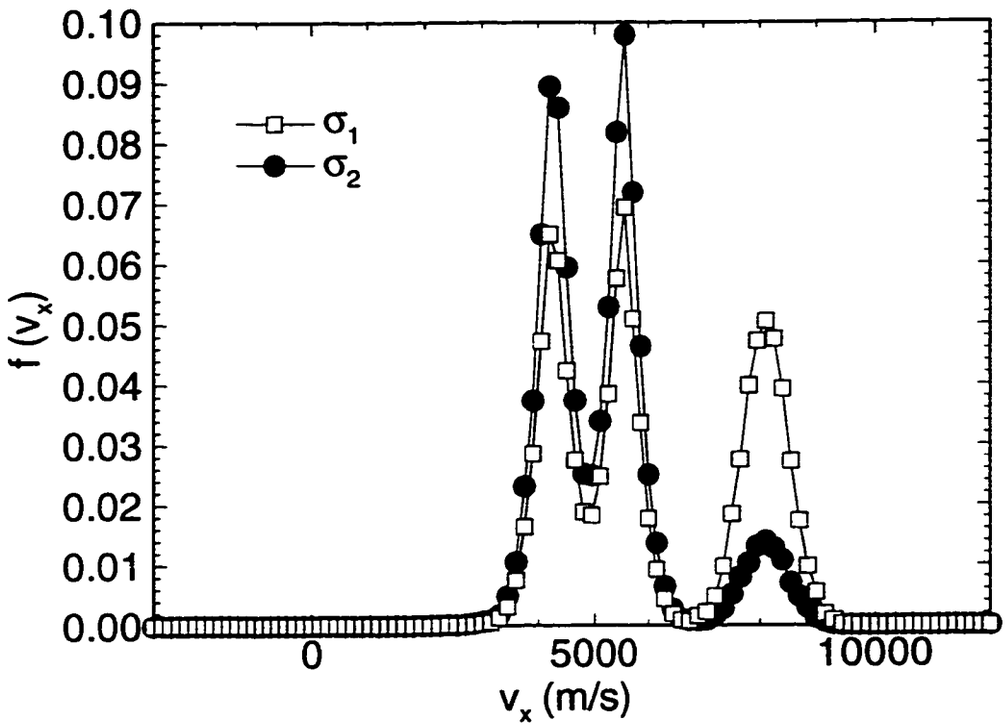

Figure 7.9. Axial Velocity Distribution Functions at the Ram Surface

Chapter 8

Surface Results

An understanding of the surface event phenomena is critical in interpreting glow brightness calculations. This chapter presents a variety of results detailing the physical behavior at the ram surface. First, an examination of the characteristics of the incident surface fluxes is presented. Second, representative cases are chosen and studied in detail, with particular emphasis being given to the effects of satellite rotation. Finally, the steady state behavior of surface coverages is shown, along with a comparison to the theoretical predictions.

8.1 Incident Fluxes

As discussed in Section 1.3, the flow field calculations and the surface concentration calculations are coupled via the incident surface fluxes. Along with the event parameters, these fluxes drive the behavior of the surface concentrations. Figure 8.1 shows the variation in the incident fluxes of the individual species with altitude. A general trend of decreased flux with altitude is noted. This is expected from the

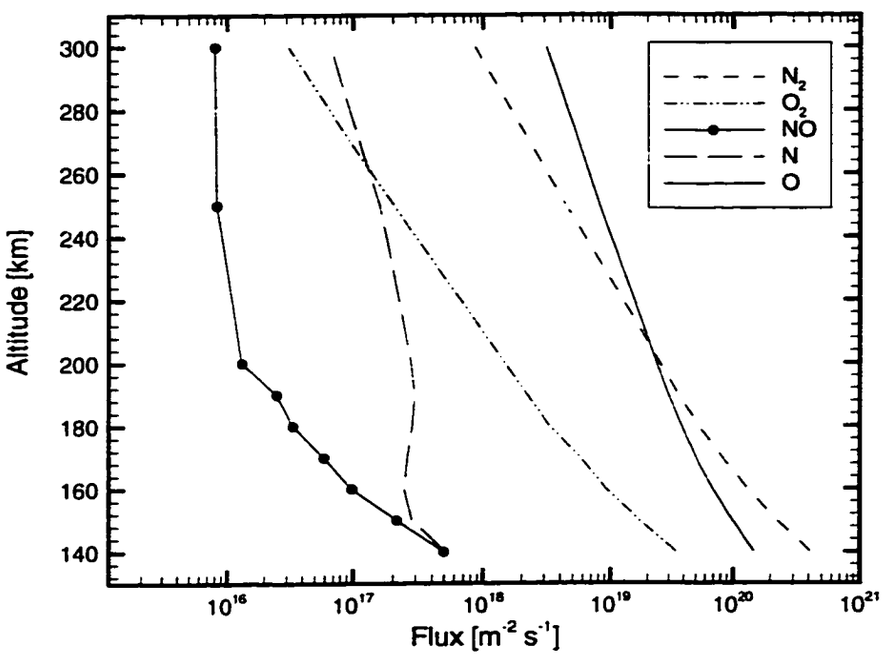

Figure 8.1. Variation of the Incident Surface Flux with Altitude

general decrease in ambient density with altitude. More importantly, the relative contribution to the total flux from each species changes with altitude. Specifically, NO, N and O contribute more to the total flux as altitude increases. Given that the relative composition of the atmosphere changes with altitude (see Figure 2.6), it follows that there will be variations in the relative importance of the fluxes of individual species.

The incident flux of nitric oxide that participates in the production of glow has two sources. Nitric oxide is found in limited concentrations in the ambient atmosphere. As was mentioned previously, these concentrations vary significantly due to solar activity, magnetic cycles, and other phenomena. Again, for this reason, the ambient concentrations of NO are taken from the NACE experiment. Nitric

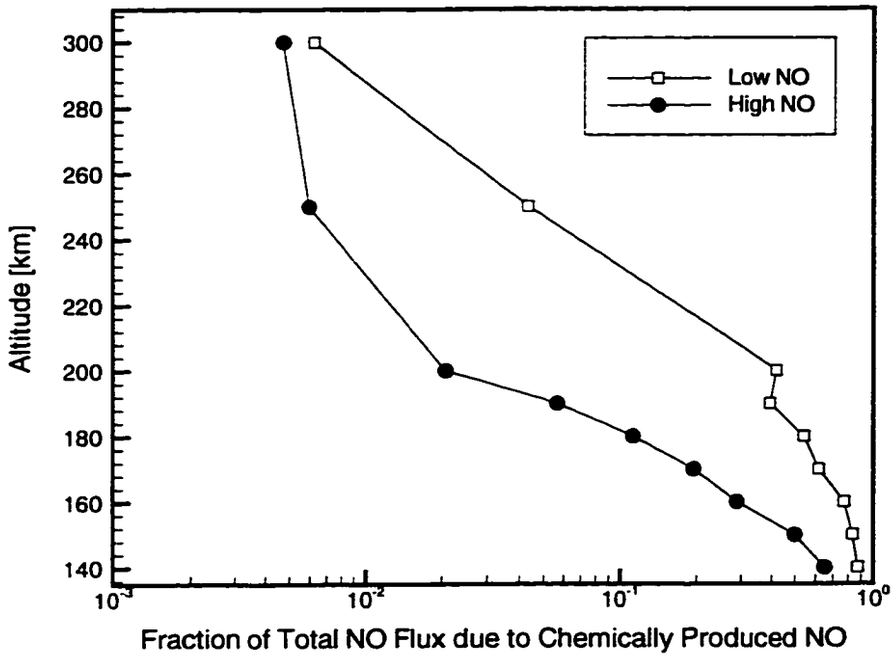

Figure 8.2. Contribution of Chemically Produced NO to Total Incident NO Flux

oxide is also produced chemically in the weak shock in front of the vehicle. At the higher altitudes, the flow is almost collisionless and the production of NO in the weak shock is negligible. Thus, almost all of the NO in the flow field is ambient NO. At the lower altitudes, a significant portion of the NO in the flow field is produced through gas-gas reactions. This behavior is quantified in Figure 8.2. The plot shows the fraction of the total incident NO flux that is chemically produced NO. Values for both the low and high ambient nitric oxide concentrations are plotted. As expected, this fraction decreases as altitude increases.

Figure 8.3 illustrates distributions of the normal velocity component of nitric oxide particles impacting the vehicle surface for the high ambient NO conditions. At 180 km, the majority of the particles striking the surface have a velocity centered

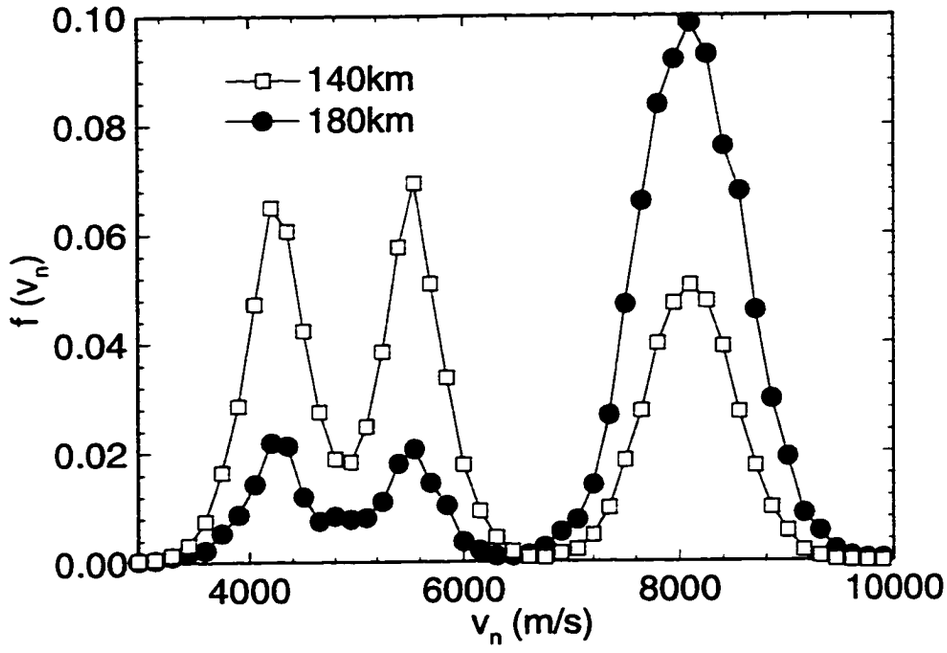

Figure 8.3. Variation of the Normal Velocity Distribution Functions at the Ram Surface with Altitude

around 8 km/s with a thermal spread corresponding to free stream conditions. This peak represents free stream particles that have reached the surface of the satellite without undergoing any collisions. The two other peaks in the 180 km distribution are representative of the nitric oxide particles created from source term reactions. The two distinct peaks are due to the different center of mass velocities of the two production reactions. The velocity distribution at 140 km shows a similar form. The main distinction lies in the relative importance of the source term NO to free stream NO. At 140 km, the majority of NO particles striking the surface are created in the flow field, as opposed to those present in the ambient atmosphere. It should also be noted that, due to the importance of the source term chemistry at the lower altitudes, the average velocity of the NO particles hitting the surface

is comparatively lower than at the higher altitudes. This becomes important when interpreting the variation of glow brightness with altitude.

8.2 Time Varying Behavior

The 140 km, high NO concentration and the 300 km, low NO concentration conditions are chosen as the representative cases. Given that the 140 km case has the highest ambient density of all of the conditions considered, chemical effects should be the most visible at this altitude. Conversely, the chemical effects should be at a minimum at 300 km. The initial surface coverage of all species at both altitudes is zero. While the assumption of a clean surface is certainly not to be expected for the real satellite surface, it provides a uniform starting condition. In all cases, the normal of the simulated surface is parallel with the velocity vector every 15 s. The incident fluxes are at a maximum at these times. A more complete discussion of the variation of fluxes with rotation is found in Section 2.1.1.

Surface coverages for all six species at 140 km are shown in Figures 8.4 and 8.5. As expected, all species show a cyclic variation in coverage with time. All species also show a truncated peak in coverage, an indication that the time scale of the system of governing differential equations is short enough at this altitude for the coverages to reach their steady state value. Furthermore, the time periods of peak coverage are offset from the times that the surface is directly perpendicular to the flow. Given the inherent time-scale of the surface phenomena, this is expected. It takes time for the surface coverages to increase as the flux increases. Similarly, it takes time for the coverages to decrease as the surface rotates away and the incident fluxes decrease. The disparate behavior of N_2 and O_2 is notable when compared to

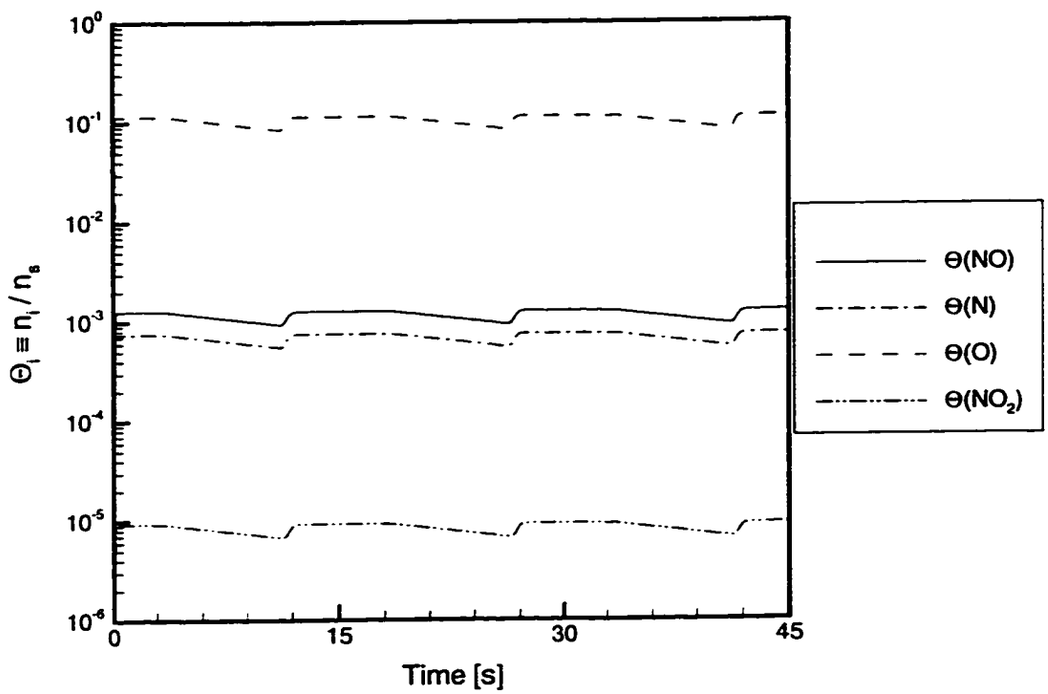

Figure 8.4. Effects of Satellite Rotation on Surface Concentrations of NO, N, O and NO_2

the other species. Both of these species have relatively low thermal desorption times. Thus when the surface is rotated away from the incident flux, their coverages drop rapidly, giving the extreme variability shown in Figure 8.5. For practical purposes, the surface coverage of molecular nitrogen and oxygen is zero during the time that the surface is in the shadow of the satellite. Finally, atomic oxygen is the dominant species, with a coverage an order of magnitude greater than N_2 and at least two orders of magnitude greater than all other species. However, the surface coverage even of atomic oxygen is only approximately 10%, indicating that the surface is primarily uncovered at this altitude.

For comparison, the surface coverages of all six species at 300 km is shown in

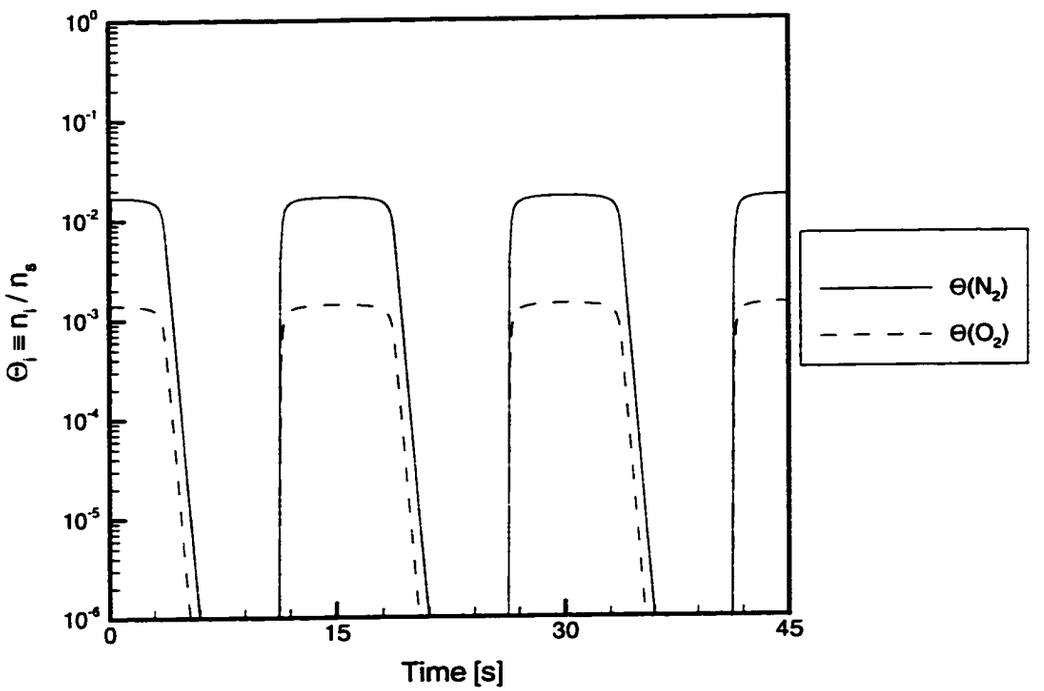

Figure 8.5. Effects of Satellite Rotation on Surface Concentrations of N_2 and O_2

Figure 8.6. While the general cyclic behavior of each species is similar, several specific differences are apparent. Notably, the peaks in coverage with each cycle are not truncated. The time scale of the system is longer at 300 km due to the lower total incident flux. Thus, there is not sufficient time for the surface coverages to reach their steady state values in each rotation. Also, there is a gradual increase in the average level of NO_2 over the first two cycles. Nitrogen dioxide exists in negligible quantities in the ambient atmosphere. None of the surface coverage is due to gaseous NO_2 that sticks to the surface. All of the adsorbed nitrogen dioxide is produced chemically on the surface. Consequently, it takes longer for levels to build up to equilibrium values on the surface. An additional difference between the two altitude cases is that the surface coverage of atomic oxygen is actually greater at

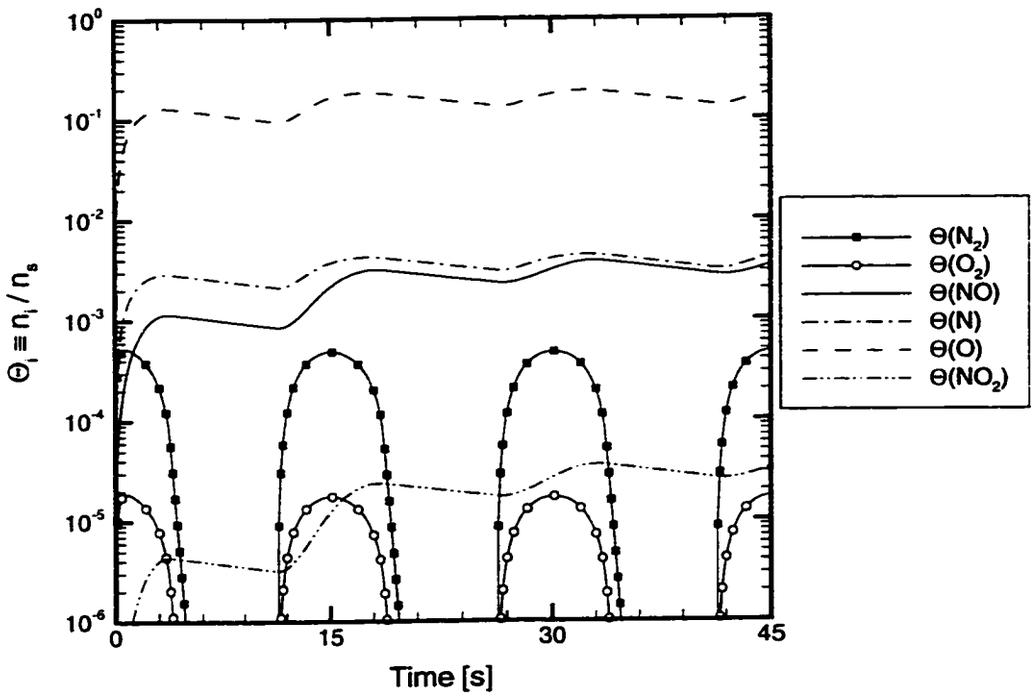

Figure 8.6. Species Surface Coverages at 300 km

the higher altitude, where it approaches peak values near 20%. The relative ambient concentration of atomic oxygen is greater at 300 km, despite the absolute incident flux being lower than the 140 km case. Thus, at high altitudes, O dominates the surface events and reaches a higher equilibrium value than at the lower altitudes.

More detailed direct comparisons of the time-accurate surface coverages at different altitudes are not particularly informative. It is more illustrative to compare relative peak surface concentrations of the species with altitude. Figure 8.7 shows this comparison. For clarity, molecular nitrogen and oxygen are shown with symbols. The relative surface concentration of these two species decreases with altitude. This follows directly from the lower ambient concentrations at the higher altitudes. Similarly, the increase in the surface coverages for atomic nitrogen and oxygen can

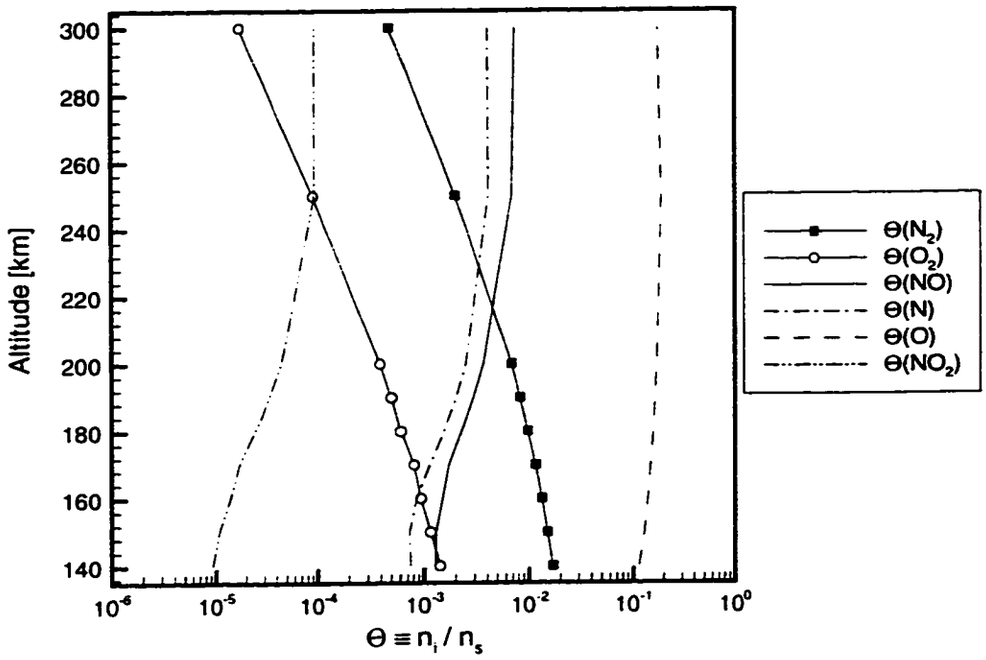

Figure 8.7. Variation of Surface Concentrations with Altitude

be explained from the higher atmospheric concentrations of these species at the higher altitudes. The increased coverages of N and O lead to the increased surface concentration of NO via the Eley-Rideal reactions (e19) and (e20). This, in turn, results in an increase in the concentration of NO_2 due to reactions (e24) and (e25).

8.3 Steady State Behavior

A number of analyses of the steady state characteristics of the system are presented in Section 5.2. The previous analysis of the time-accurate simulation shows that at the lower altitudes, the peak surface coverages are truncated, indicating that the steady state value has been reached. It is therefore insightful to investigate the

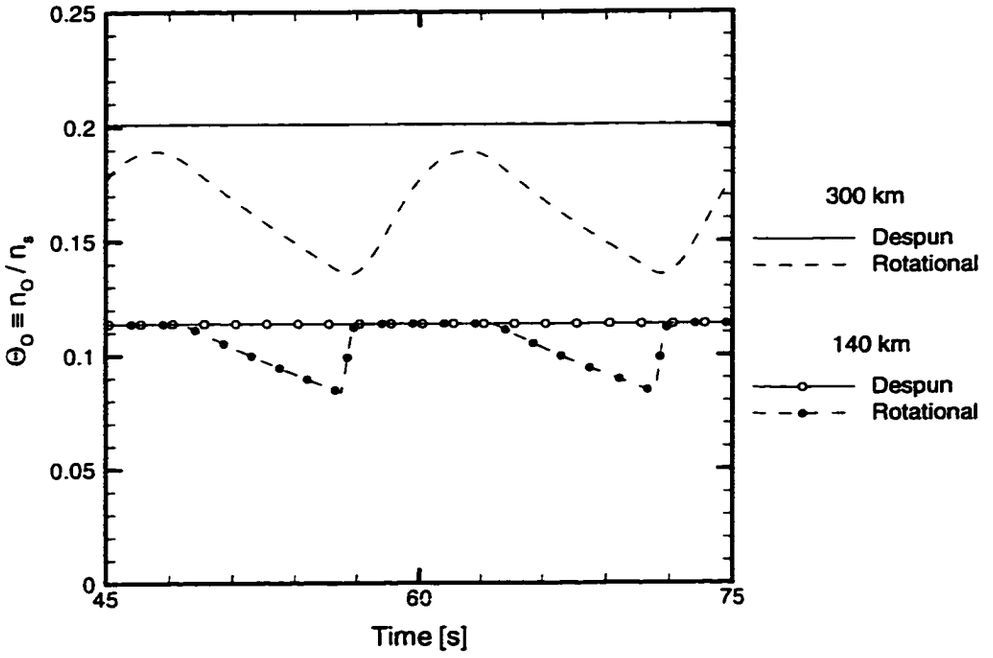

Figure 8.8. Comparison of the Surface Coverages of Atomic Oxygen under Despun and Rotational Conditions

steady state behavior of the system.

A comparison of surface coverage of atomic oxygen under despun and rotational conditions is given in Figure 8.8. The coverages at two extremes in altitude are considered. A time period several rotational periods after the start of the simulations is chosen. Any effects of the clean surface initial condition are no longer present during this time period. The despun curves represent results from simulations where the surface is exposed to the full incident fluxes for the entire length of the simulation. These curves closely approximate the steady state values for the chosen conditions. For the 140 km case, the peak coverage during rotation is seen to quickly reach a value equal to the despun value; this is the truncation effect seen in Figures 8.4–8.5. At 300 km, the peak coverage during rotation approaches but does

not reach the despun value. This difference in behavior is predicted by the time scale analysis presented in Section 5.2.2. The inherent time scale of the system of differential equations is found to vary inversely with the total, absolute flux. Thus, at 140 km, where the maximum flux is much greater, the time scale of the system is shorter and more quickly reacts to the increase in flux as the surface rotates into the incident flow. The time scale of the system under these conditions is short enough that the coverages actually reach their steady state values. At 300 km, the total flux is less, the time scale much greater, and there is no longer sufficient time for the coverage of atomic oxygen and the other species to reach their steady state values. Before this occurs, the surface rotates away from the incident flow and the coverages begin to decrease.

Simulation of the surface with constant incident flux allows the surface coverages to reach their steady state values. The steady state coverages calculated by the Runge-Kutta method may be compared to the theoretical steady state coverages obtained via the analytic analysis presented in Section 5.2. This serves as a means of validating the implementation of the Runge-Kutta scheme. Consistent with the assumptions of the theoretical analysis, no surface chemistry is included in any of the runs used for the comparison. Thermal desorption is included. Figure 8.9 graphically compares the theoretical results with the simulated results. As is evident, the two calculations agree exactly. Since both results are simulations of the same set of differential equations, this is expected. The exact agreement is taken as validation that the Runge-Kutta method is implemented properly.

Also included for completeness in Figure 8.9 are the rotational surface coverages calculated by the Runge-Kutta method. The forward-looking values are plotted,

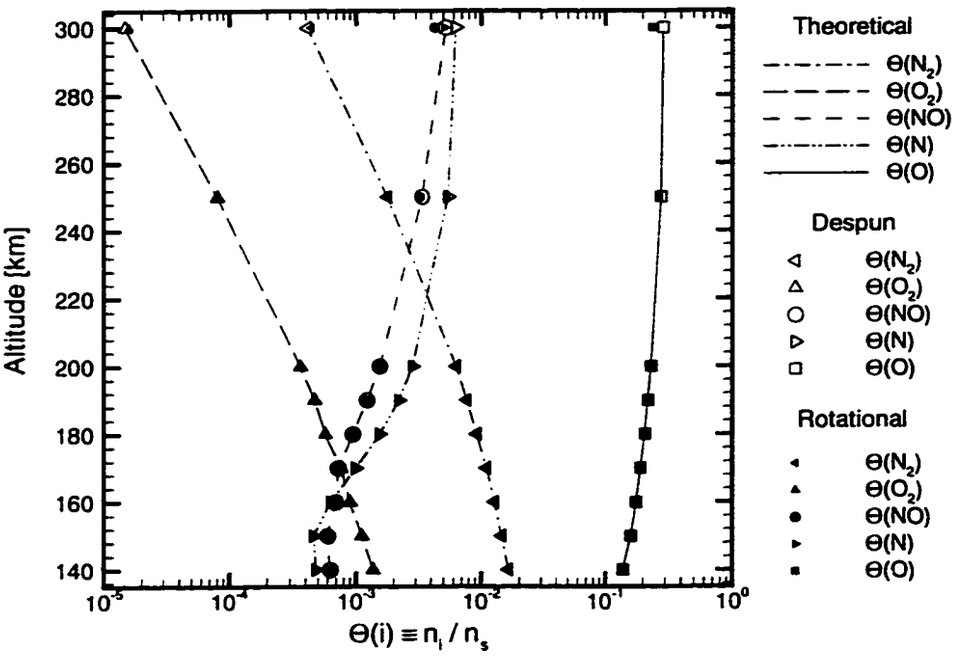

Figure 8.9. Comparison of the Theoretical and Runge-Kutta Calculation of Steady State Surface Coverages

where the surface coverages are at a maximum. Re-iterating the point of the previous discussion, the peak rotational values at the lower altitudes are equal to the steady state values. This is not the case at the upper altitudes. For the species with long thermal desorption times that dominate the surface coverage (NO, N, O), the peak rotational values are lower than the steady state values. As is previously explained, this is a direct result of the longer time scale of the system at the upper altitudes. The remaining species (N_2, O_2) actually show a peak rotational coverage greater than steady state. This is a result of the lower coverages of the more common species, allowing for greater rates of physical adsorption.

Chapter 9

Glow Results

The primary focus of the present work is to use a detailed simulation to calculate the production of glow in front of ram surfaces in low Earth orbit. This chapter presents a variety of glow brightness results. The ability to examine many aspects of glow production shows the benefits provided by the level of detail in the solution procedure. Specifically, the behavior of the glow brightness with time is presented and discussed. The sensitivity of the calculated glow brightness to the event parameters is assessed. From this sensitivity analysis, the critical glow production and precursor reactions are identified. A comparison is made between the simulated glow brightness and experimental measurements taken during flights of the AE satellite. Glow measurements taken during flights of the Space Shuttle are also compared to simulated values.

9.1 Sensitivity to Event Parameters

Given the large number of surface events, shown in Tables 6.3 and 6.4, it is useful to study the sensitivity of the glow brightness to the event parameters. From this sensitivity study, the important events are identified. For each event, the corresponding baseline value of the parameter is multiplied by the factors 0.1, 0.2, 0.5, 2, 5, and 10. Incidences where this multiplicative factor leads to unphysical values of the parameter are ignored. A complete surface event simulation is performed for each modified value. The low NO concentration DSMC simulation at 140 km is used to determine the incident fluxes.

An examination of all of the surface events shows that events (e26), (e27), (e28), and (e33) are the reactions that lead directly to the production of NO_2^*. These reactions are referred to as the production reactions. The only reactants in all of these reactions are NO and O. It is expected that the glow brightness will be most sensitive to parameters of events relating to these two species.

The sensitivity to the sticking coefficients of the free stream species is shown in Figure 9.1. Glow brightness is most sensitive to three of the coefficients—those for N_2, NO, and O. For atomic oxygen and nitric oxide, the brightness is proportional to the sticking coefficient. Increases in the surface coverages of these species enhances the production reactions. For molecular nitrogen, the brightness is inversely proportional to the sticking coefficient. Molecular nitrogen acts as an inhibitor because it is not a direct precursor to glow and adsorbed N_2 competes with precursors for free surface sites. It is an important inhibitor simply because it is the second most common species in the altitude range of interest.

The glow shows little sensitivity to the thermal desorption times. The primary

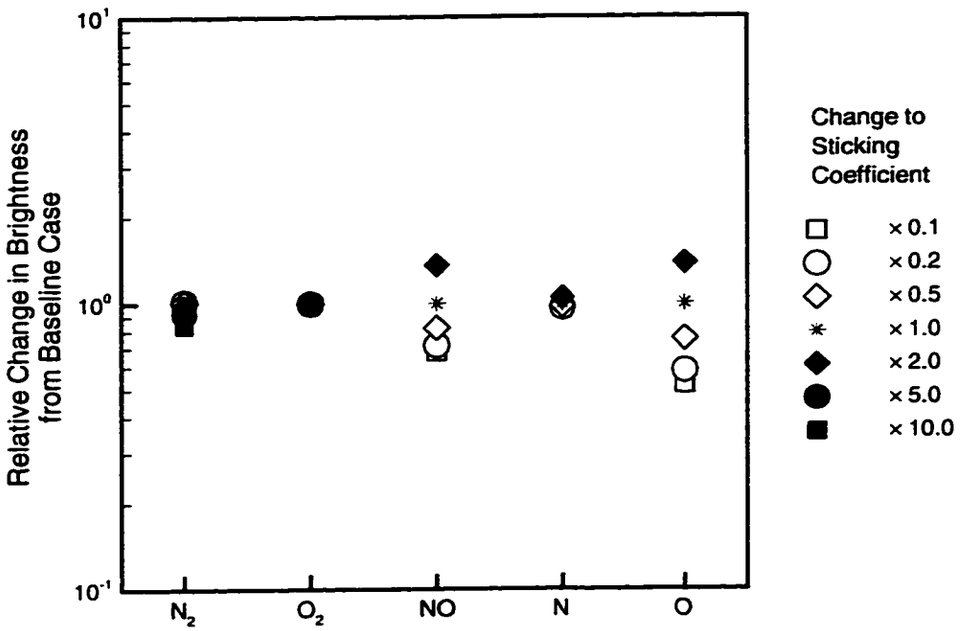

Figure 9.1. Sensitivity to Sticking Coefficients

effect of changing the desorption time is to change the overall behavior of the surface coverages. The disparate behavior of species with radically different thermal desorption times is discussed in Section 8.2. Figure 9.2 further demonstrates the effect. The figure shows the sensitivity of the surface coverage of NO to its desorption time at 140 km. A time of 25 s is the baseline value for NO; a value of 0.25 s is consistent with the values for molecular nitrogen and oxygen. With the shorter desorption time, the coverage of NO drops dramatically while the surface is in the shadow of the satellite body. The peak coverage values for both cases are comparable. In essence, the flux of NO is sufficient to build up its coverage to the steady state values regardless of the starting coverage at the beginning of each cycle. This effect is strongest at the lower altitudes. Importantly, this is not the case

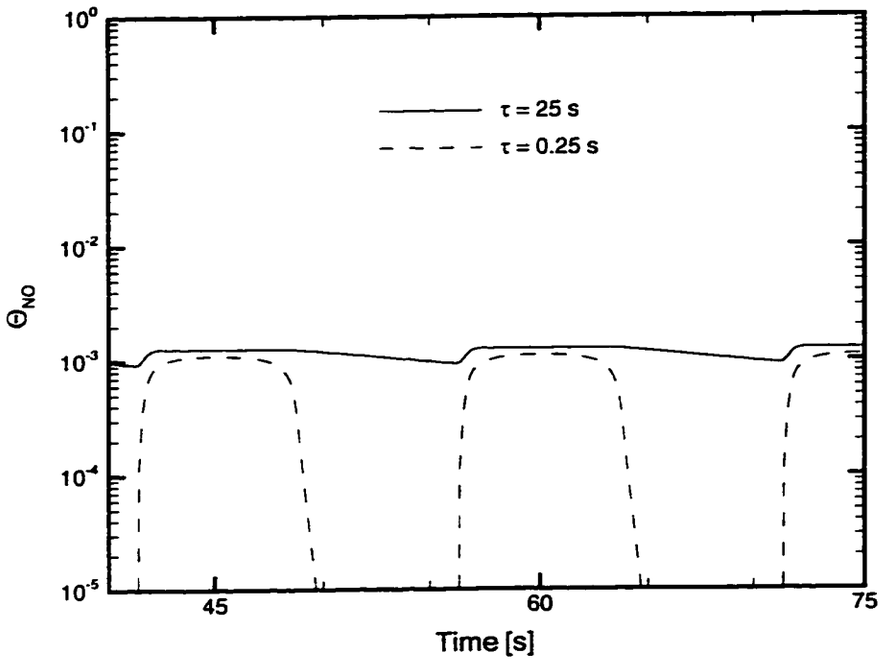

Figure 9.2. Effect of Thermal Desorption Time on NO Surface Coverage

for glow brightness measurements taken during the shadow half-period. Very little experimental data is available for this period, so this is not a focus of this sensitivity analysis. It is noted, however, that a decrease in thermal desorption time of critical species such as NO and O would result in a decrease in the shadow glow brightness.

The effect of varying the collisional desorption cross-sections is given in Figure 9.3. For these events, the glow production is sensitive to cross-sections for N, O, and in particular NO. All three species show that the glow is inversely proportional to the cross-sections. Given that NO and O are the only reactants of the production reactions, this sensitivity result is not surprising.

Figure 9.4 shows the sensitivity to the cross-sections for all of the Eley-Rideal

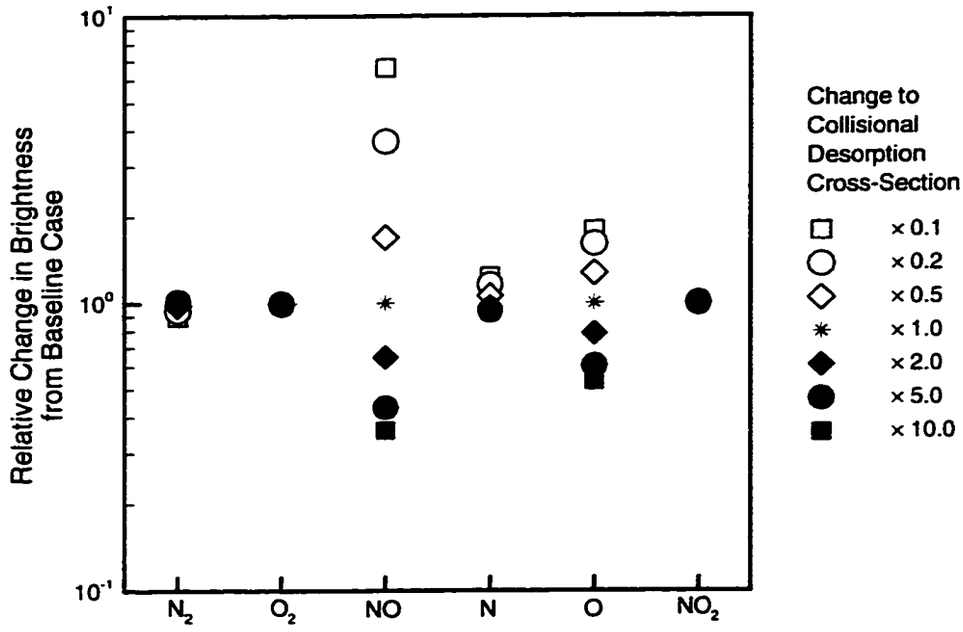

Figure 9.3. Sensitivity to Collisional Desorption Cross-Sections

reactions, events (e18–e29). The glow brightness is strongly sensitive to changes in cross-sections for events (e18), (e26), and (e28). The first two of these reactions lead to an increase in the surface coverage of nitric oxide. The last two of these reactions are production reactions that lead directly to the formation of NO_2^*. The magnitude of the sensitivity to event (e28) identifies it as the primary production reaction. The glow brightness is mildly sensitive to changes in cross-sections for events (e19), (e20), and (e29). Both (e19) and (e20) positively affect the surface coverage of NO, so an increase in the cross-sections for these events leads to an increase in glow. Event (e29) serves to remove atomic oxygen from the surface, thus glow brightness varies inversely with the cross-section of this event.

The calculated glow brightness shows little sensitivity to the Langmuir-Hinshel-

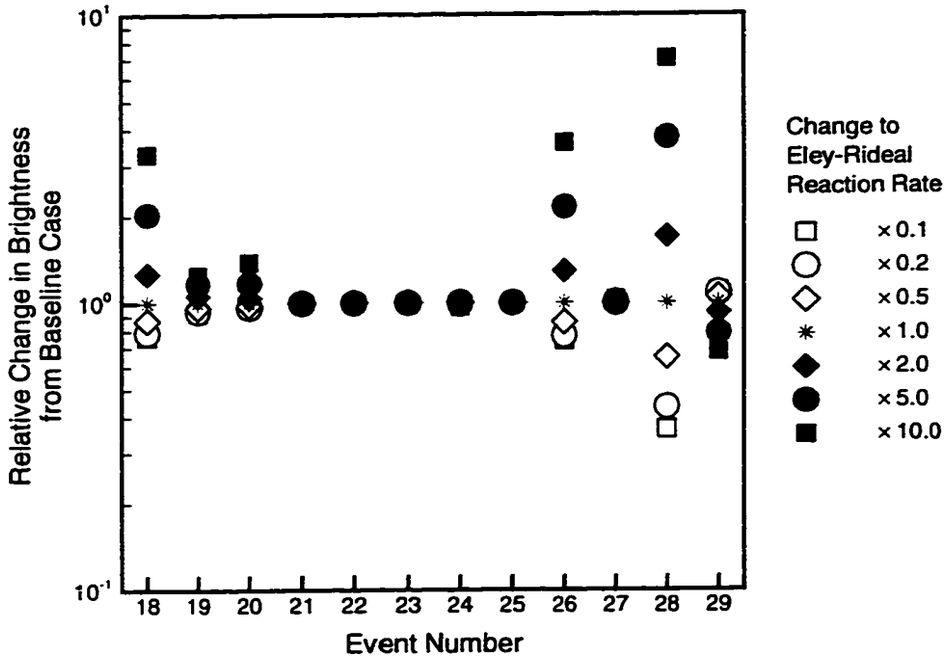

Figure 9.4. Sensitivity to Eley-Rideal Cross-Sections

wood reaction rates. This behavior is to be expected after an examination of the governing system of ODE's, Equation 5.6. The term corresponding to production from a surface-surface reaction contains the expression $\left(1-\epsilon_{ij}^{lh}\right) n_s K_{ij}^{lh} \Theta_i \Theta_j$. Given that n_s is $\mathcal{O}(10^{19})$, K is $\mathcal{O}(10^{-23})$, and all other terms are $\mathcal{O}(1)$, the magnitude of this term will be of $\mathcal{O}(10^{-4})$. A similar analysis of another term, e.g. the expression for collisional desorption, gives a magnitude as high as $\mathcal{O}(10^{-1})$. Therefore, it is not surprising that Langmuir-Hinshelwood reactions have a limited effect on the overall glow production.

The sensitivity study shows that parameters relating to nitric oxide and atomic oxygen are the most important values in determining the glow brightness. Again, this is to be expected, because NO and O are the only reactants in the production

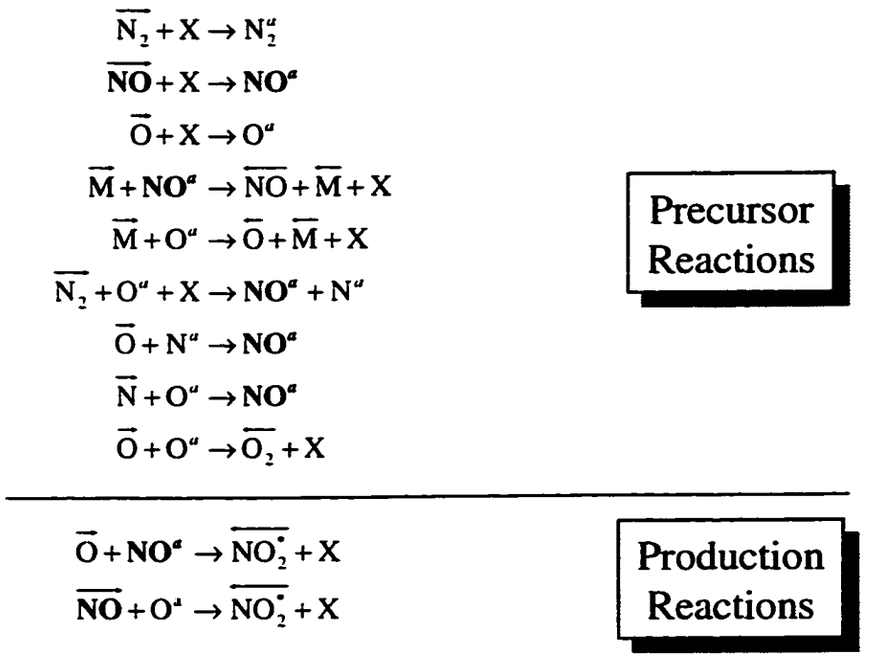

Figure 9.5. Important Precursor and Production Reactions

reactions. Specifically, the events (e1), (e3), (e5), (e14), (e16), (e18), (e19), (e20) and (e29) are identified as the critical precursor events. Furthermore, the Eley-Rideal reaction $\vec{O} + NO^a \rightarrow \overleftarrow{NO_2^*} + X$ (e28) is found to be the dominant production reaction. Reaction (e26) is found to be a secondary production reaction. For clarity, these reactions are listed in Figure 9.5. Nitric oxide, which participates in many of these reactions, is highlighted in the figure.

The above sensitivity analysis examined the behavior for the 140 km, high NO concentration conditions. The sensitivity at 300 km for low NO concentration conditions is also examined. The results of this examination are not different enough from the results at 140 km to warrant additional figures. There are three notable differences. First, the glow brightness becomes sensitive to changes in the thermal desorption time of nitric oxide. The flux of NO at 300 km with low ambient NO concentration is substantially lower than the flux at 140 km. Therefore, there is

not a sufficient level of flux to replace the nitric oxide if significant amounts are lost to thermal desorption. This is another consequence of the increased time scale of the system at higher altitudes. Second, events involving atomic nitrogen become more important—specifically adsorption, collisional desorption and the Eley-Rideal reactions (e19) and (e20). This is a direct consequence of the increase of the relative atomic nitrogen concentration at the upper altitudes. Third, the glow brightness is slightly sensitive to the Langmuir-Hinshelwood production reaction (e33) even during the forward-looking half-period. At the higher altitudes, the flux is lower and the surface concentrations are comparable if not higher, which explains the increased significance of surface-surface reactions compared to gas-surface reactions.

9.2 Temporal Variation in Glow Production

Figure 9.6 shows time-accurate results for glow brightness. Both despun and rotational predictions are shown for the 140 km and 300 km altitudes. Comparing the despun results for both altitudes shows that the brightness reaches its steady state value very quickly at 140 km, whereas at 300 km nearly 15 s is required. This is a direct consequence of the higher incident flux at 140 km. The rotational results exhibit the expected qualitative behavior, showing a cyclic variation with a period of 15 s. Two distinct phenomena are evident. For each half period corresponding to when the detector is exposed to the incoming flux, the brightness rises to a maximum value and then decreases. It may be noted that the peak value occurs slightly after the time of maximum flux due to the inherent time scale of the chemical processes which lead from incident fluxes to glow production. The other half-period shows a log-linear decrease in glow, corresponding to when the detector is in the

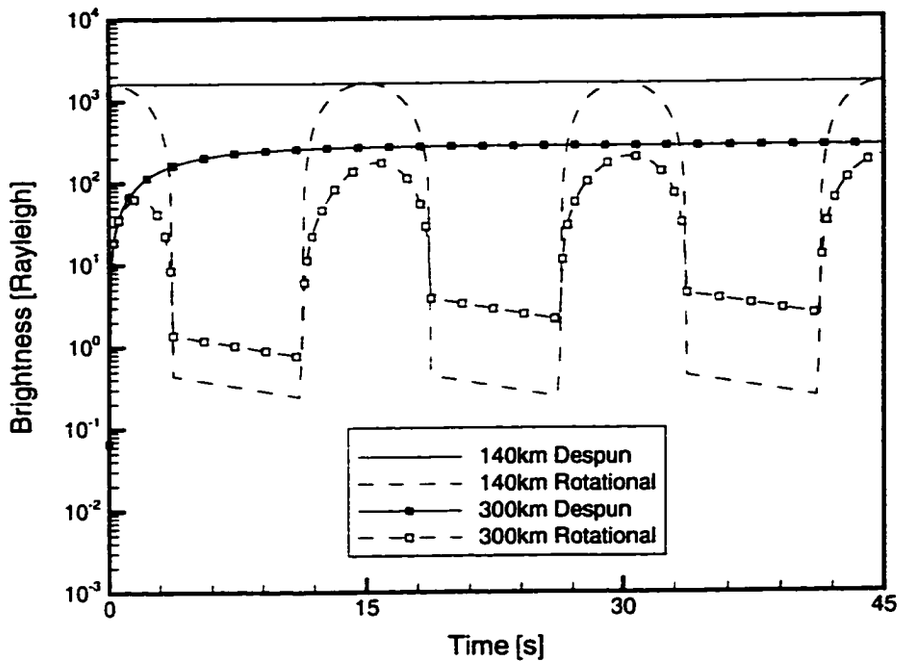

Figure 9.6. Effects of Satellite Rotation on Glow Brightness

shadow of the satellite and thermal desorption dominates. The peak glow values in the rotational case at 140 km match the despun steady state value. This is not the case at 300 km. Again, this is attributed to the lower flux at 300 km.

One counter-intuitive feature of the glow brightness behavior is that in the shadow region, the glow at 300 km is brighter than the glow at 140 km. To understand this behavior, it is helpful to examine the contribution of the various production reactions. The contribution of glow from the different production reactions at 140 km is shown in Figure 9.7. This figure shows the one full rotational period of the simulation, with two half-periods being identified. In the first half-period, glow production is found to be dominated by gas-surface reaction (e28). Thus, the magnitude of the incident flux controls glow production in this period. In the sec-

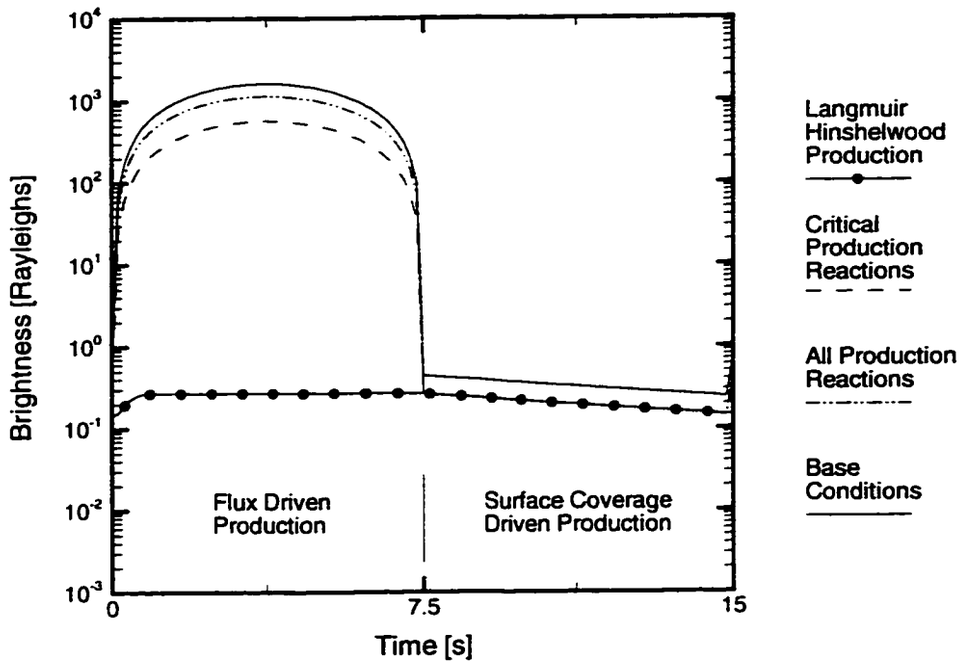

Figure 9.7. Contribution to Glow Brightness from the Production Reactions

ond half-period, the surface is in the shadow of the satellite and there is no flux to the surface. Therefore, the only production is through surface-surface reactions and surface coverages drive the glow production. The curve labeled 'Base Conditions' tracks the glow production with all reactions included and serves as a basis for comparison of the other cases. The next curve, labeled 'All Production Reactions' shows the time history of glow production with only the production reactions included. The difference between this case and the base case is attributed mainly to the increase of the surface concentration of nitric oxide from various precursor reactions, (e18–e21). The third curve of interest represents glow production with only the critical Eley-Rideal production (e28) and the Langmuir-Hinshelwood production reaction (e33) included. There is only a small difference in the first half-period

between the 'Critical Production' results and the 'All Production' result. This is further evidence of the degree to which reaction (e28) dominates forward-looking glow production. The fourth curve, 'Langmuir-Hinshelwood', shows the contribution to glow production due solely to the surface-surface reaction (e33). Given that all other production reactions rely on an incident flux, reaction (e33) accounts for all glow production for the half-period that the surface is in the shadow of the satellite. The level of production during this period depends only on the surface coverages of NO and O as the surface rotates into the shadow. This explains why the base case shows a slightly higher brightness during the shadow half-period. The additional chemistry in the base case results in a higher coverage of NO. This also explains why the glow in the shadow half-period is greater at 300 km than at 140 km, as shown in Figure 9.6. The surface coverages of both NO and O are greater at the higher altitudes, which is discussed in Section 8.2. These greater coverages result in greater glow production through reaction (e33).

As a final look into the representative case at 140 km, the orbital speed of the satellite in the DSMC simulation was lowered from 8 km/s to 7.2 km/s. This lower value may be more reasonable considering the co-rotation of the atmosphere[4]. Given this reduction of orbital velocity by 10%, the glow production behaves as expected, with reduction in peak glow brightness of approximately 11%. The small discrepancy is due to reduced gas-gas chemistry. This close correspondence also indicates that additional simulations with varied orbital speeds are unnecessary at any altitude.

9.3 Atmosphere Explorer Glow Brightness

The Atmosphere Explorer satellites provided a wealth of experimental glow measurements. This section compares calculated glow brightness values with selected experimental measurements. Some of the factors to which the calculated values are sensitive are examined and discussed.

9.3.1 Variation With Altitude

The forward-looking values for glow brightness at 656.3 nm for both ambient NO concentrations are compared to experimental data from the AE satellite in Figure 9.8. The experimental data are taken from Ref. [1]. The data from this source was calibrated from the photometer measurements using the assumption of a spectrum of discrete atomic lines. Given this erroneous assumption and other sources of error typical to measurements taken under orbital conditions, the estimate of error in the experimental data is taken to be around a factor of two. The slope of calculated values at the lower altitudes is shown to agree fairly well with the measured glow brightness. The magnitude of the calculated glow overpredicts the experimental data by approximately a factor of five at the lower altitudes. The overprediction is much greater at the upper altitudes. This is a substantial improvement over the previous results presented in Ref. [10]. The overprediction is attributed to uncertainties in both the control event parameters and the exact structure of the NO_2^* spectrum.

Furthermore, the sensitivity to the ambient concentration of NO is greater at the higher altitudes. This is a direct result of the chemically produced NO being less significant at the higher altitudes, which magnifies the importance of fluctuations

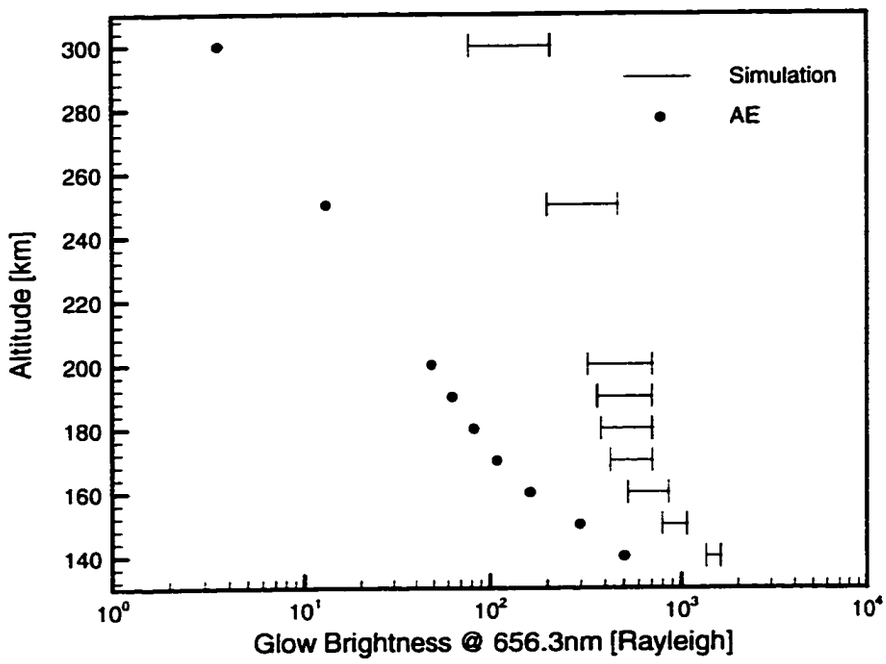

Figure 9.8. Comparison to Atmosphere Explorer Data at 656.3 nm

in the ambient concentrations. The magnitude of the variation in glow brightness (approximately 2.67) is not equal to the magnitude of the variation in the ambient concentration of NO (approximately 7.0). This is explained through consideration of the contribution of the different glow production reactions. At 300 km, for the low NO concentration case, reaction (e28) accounts for 85.9% of the glow, while reaction (e26) accounts for 11.5% of the glow. Reaction (e26) depends directly on the incident flux of nitric oxide. So this reaction would see a seven-fold increase as the NO flux increases. However, reaction (e28) depends on the surface coverage of nitric oxide. An analysis of the surface concentration results shows that the coverage of NO only increases by a factor of two in the highest NO concentration case. Weighting these changes to the production by the contribution of each reaction

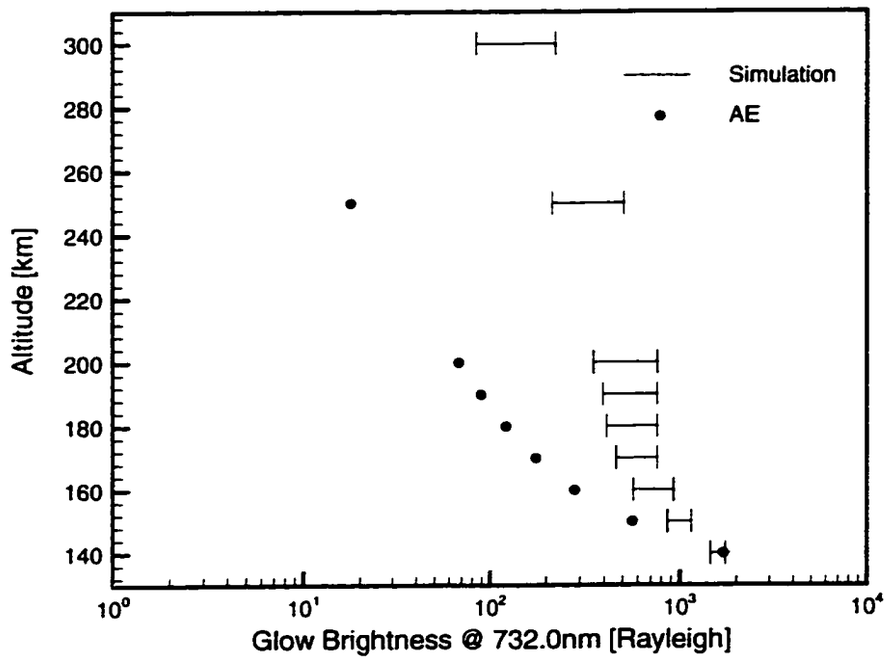

Figure 9.9. Comparison to Atmosphere Explorer Data at 732.0 nm

suggests a overall increase that agrees with the simulated value of 2.67.

Figure 9.9 compares the simulated values for glow brightness to the experimental measurements at the 732.0 nm wavelength. These data are taken from Ref. [5] and are subject to the same error estimates as the previous data. At this wavelength, the magnitude of the calculated values agrees better with the measurements than at the shorter wavelength. The slope of the calculated glow brightness with altitude is greater than the slope of the experimental data. At the upper altitudes there is an overprediction. Again, this is attributed to the uncertainties in determining the event parameters and the exact shape of the nitrogen dioxide structure. The sensitivity to the ambient NO concentration is also seen at this wavelength.

The sensitivity study of glow brightness to the event parameters identifies the

critical precursor reactions. An examination of the baseline set shows that the parameters for nitric oxide are similar to those of the atomic atmospheric species. Many of these parameters are based on experimental measurements of NO interaction with clean, metallic surfaces. These values are consistent with those for atomic species. However, the surfaces of a ram surface in orbit are likely to be covered with a monolayer of chemisorbed oxygen, as is discussed in Section 5.1. Another reasonable assumption is to use event parameters specific to NO that are consistent with the molecular species. Figure 9.10 show the glow brightness at 656.3 nm with the assumptions of a NO sticking coefficient of 0.03, a thermal desorption time of 0.25 s, and a collisional desorption cross-section of 10^{-19} m^{-2}. These values are identical to those of molecular nitrogen and oxygen. Furthermore, the cross-section for the primary production reaction (e28) is reduced by a factor of two. As is evident, the simulated glow brightness shows much better agreement than in the baseline case. The purpose of the figure is not to suggest that the modified values are better choices for nitric oxide and the system of equations. Rather, the results show how the calculated values are sensitive to the choices of the event parameters.

9.3.2 Effects of Rotation Direction

As discussed in Section 2.1.3, glow measurements taken perpendicular to the velocity vector show a variation with the direction of the rotation of the satellite. Figure 2.3 depicts two geometries that show a difference in measured glow brightness. The first of these points occurs after a one-quarter rotation of the satellite; the second point represents a three-quarter rotation. Figure 9.11 show the glow brightness for one period of rotation at 300 km. The one-quarter and three-quarter points

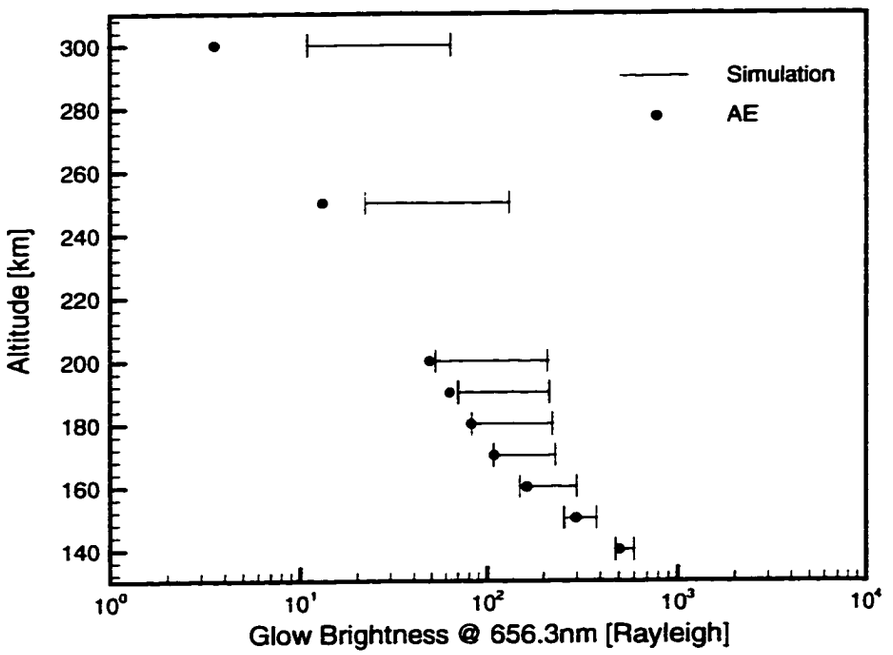

Figure 9.10. Comparison to Atmosphere Explorer Data at 656.3 nm with Modified NO Event Parameters

have been identified. Clearly, there is a difference in brightness between the two points. This is attributed to a reduction of NO and O surface coverages, which results in reduced glow production via event (e33). The calculated glow brightness at the one-quarter point is approximately 4.36 Rayleighs. At the three-quarter point, the glow brightness is approximately 2.46 Rayleighs. Thus, this represents a 43.6% reduction. However, this change is only 0.92% of the peak glow value of approximately 205 Rayleighs. These findings are consistent with unpublished experimental measurements[21].

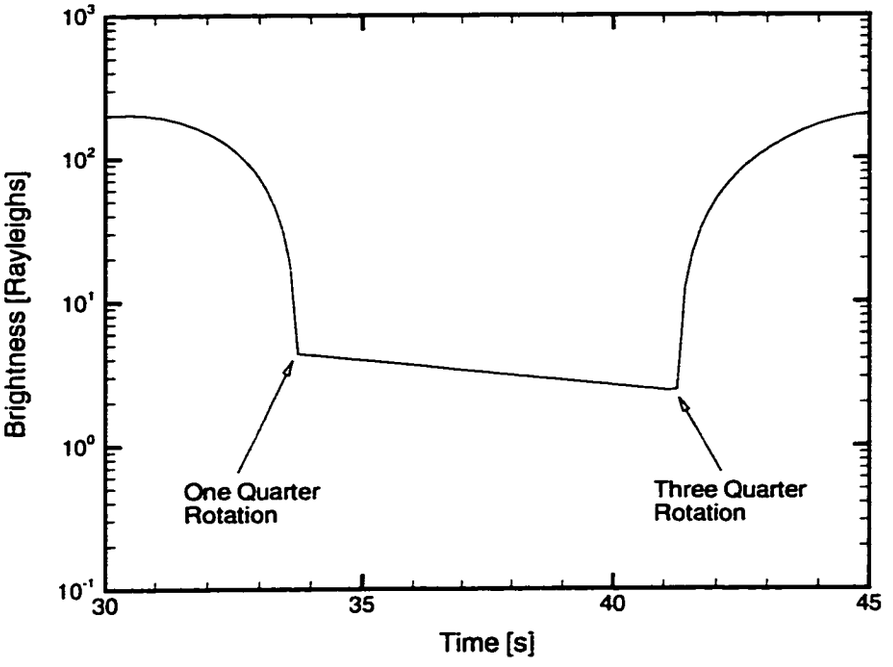

Figure 9.11. Effect of Rotation Direction on Glow Brightness

9.4 Space Shuttle Glow Brightness

The Space Shuttle is also a good source of experimental glow measurements. While fundamentally the same phenomenon, measurements from the Shuttle are generally distinct from Atmosphere Explorer measurements. First, Shuttle glow brightness is often reported in relative units—the structure of the brightness is focused on rather than the quantitative values. Second, measurements of the actual glow spectrum are available from the Shuttle experiments. The simple instruments on board the AE satellite do not allow for the spectrum to be specifically determined. Finally, the environment around the shuttle is more susceptible to contamination from external sources.

For simulations of the shuttle environment, the same axisymmetric cylinder used

Table 9.1. Variation of Incident Flux With Area

Species	Normal Area $[m^{-2}s^{-1}]$	Double Area $[m^{-2}s^{-1}]$	Change
N_2	8.62e+17	8.59e+17	+0.35%
NO_2	3.10e+16	3.16e+16	-1.94%
NO	5.62e+16	5.59e+16	+0.53%
N	6.72e+16	6.80e+16	+1.19%
O	3.12e+18	3.12e+18	0.00%

for the AE simulations is employed. As discussed in Section 6.1.3, the assumption is made that the flow field is rarefied enough that this gross approximation to the geometry is acceptable. To test the assumption, a flow simulation was performed using a cylinder with twice the cross-sectional area. Average values for the fluxes of the individual species for both the baseline and double area cases are given in Table 9.1. The change in flux is negligible for all species. The relatively small changes supports the use of a small cylinder to determine the incident fluxes.

As with the Atmosphere Explorer, the variation of glow brightness with altitude of the calculated and experimental values are compared. In this case, the relative brightness is shown. Therefore, it is the slope of the data that is important. The comparison is shown in Figure 9.12. The experimental data are taken from the flight of STS-62, as presented in Ref. [12]. Note the relatively wide range of slopes represented by the two bounding lines of the simulated data. Overall, the slope of the simulation data compares well with the Shuttle data. The slope of the experimental data falls within the range of slopes suggested by the simulation results.

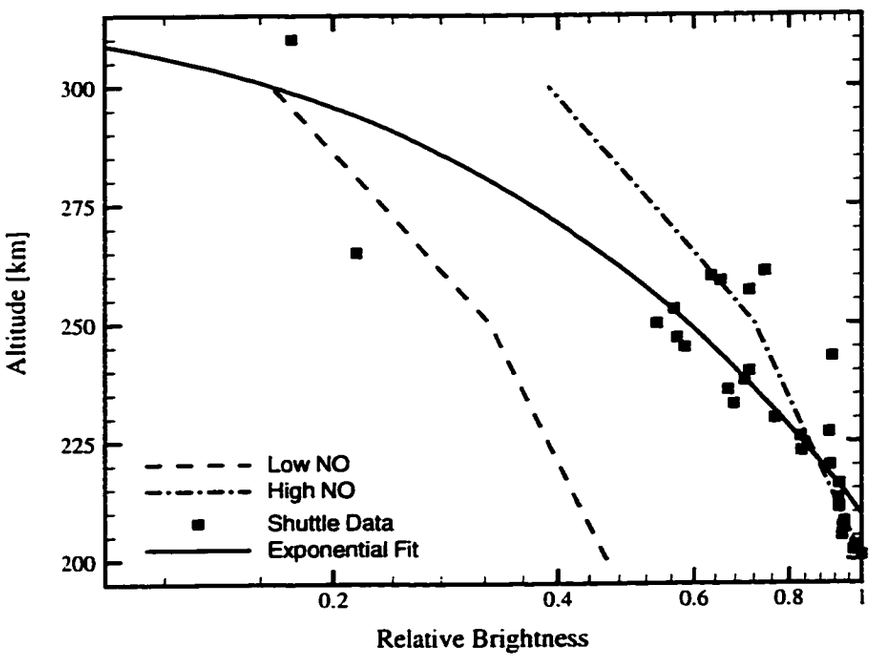

Figure 9.12. Variation of Relative Glow Brightness with Altitude

The ambient NO levels used for these simulation are again taken from experimental measurements by the AE satellite. In general, these NO concentrations show a steeper slope than the scale height of NO would suggest. Certainly, it is likely the Shuttle experienced different ambient conditions than did the AE satellite.

Chapter 10

Conclusions

Given the detailed nature of the solution procedure used to calculate spacecraft glow, it is helpful to review the findings of the comparisons between the simulations and experiments. The major goal of the review presented in this chapter is to put the results into context. A section discussing the possibilities for future work is also included.

10.1 Summary and Conclusions

For the results of any computational simulation to be meaningful, they must be validated through successful comparison with experimental measurements and analytical analyses. Through the comparisons presented in Chapters 7- 9, the solution procedure has been found to give reasonable agreement with experimental measurements. Quantitative agreement within a factor of five to Atmosphere Explorer data for the the lower altitude was achieved. Good agreement was shown between simulated values and Space Shuttle data for the variation of relative brightness with

altitude. Calculation of the steady state surface coverages was found to match the predictions of an analytical analysis. From a consideration of all of the comparisons, the multi-step solution procedure has been found to be a viable method to calculate spacecraft glow.

The structure of the flow field results was as expected. At the lower altitudes, a very diffuse weak shock was observed in front of the ram surface. At the upper altitudes, where the ambient density is lower, the flow fields exhibited free-molecular behavior. Under all conditions, the axial velocity distribution functions were non-Maxwellian and showed bimodal and more complex behaviors. The DSMC overlay method demonstrated its ability to simulate accurately the behavior of trace species in a rarefied flow. The assumption that certain species are rare throughout the flow field was found to be valid. There were not enough collisions in the rarefied flow field for chemistry to have a significant effect on the overall structure. The effects of gas-gas chemistry were primarily limited to a change in the concentrations of the rare species. Production of the rare species though chemistry was more important at the lower altitudes. Thus, the calculations were less sensitive to the ambient concentrations of the rare species at the lower altitudes. At the higher altitudes, virtually the only source of the rare species was the ambient atmosphere, and therefore these ambient concentrations had a larger effect on the final calculations.

The difficulty in determining the free stream concentration of ambient nitric oxide had implications throughout the entire solution procedure. To account for the variation in ambient concentration of NO, two different values were used, representing a range of reasonable values found in the Earth's atmosphere. Thus, a range of incident flux levels for NO was determined for use in the surface event calculations.

This, in turn, resulted in a range of the calculated glow brightness at each altitude. Furthermore, the values of NO concentration used were determined from experimental measurements of the Atmosphere Explorer satellite. In general, these values showed less of a decrease in altitude than the theoretical scale height would indicate. Given the complex mechanisms by which NO is created, this discrepancy was not taken as an indication of error in the experimental measurements. However, the net result was that the relative concentration of NO was greater at the upper altitudes. Ultimately, the increased relative importance of NO at the upper altitudes resulted in a higher glow production than might otherwise have been expected.

Steady state surface coverages calculated with the Runge-Kutta method matched those of an analytical analysis. The surface coverages of the different species were found to depend primarily on the relative distribution of the incident fluxes. The effect of the absolute level of flux was a secondary effect. This resulted in the somewhat counterintuitive behavior that, for most cases, the surface coverages increased as the overall flux level decreased. Thus, the surface coverages were higher at the higher altitudes, where the flow field densities and incident flux levels were lower.

As expected, the surface coverages of the species demonstrated strong cyclical variations with time during the rotational cases. Two distinct regions were identified in each cycle. For the first half-period, flux driven events dominated. Physical adsorption and collisional desorption balanced each other and together determined the surface coverages of the species. Glow production during this region was driven mainly by the gas-surface reaction (e28), in which gaseous atomic oxygen reacts with surface adsorbed nitric oxide. During the second half-period, the surface was in the shadow of the satellite body and, consequently, the incident fluxes were zero.

Thermal desorption controls the changes to the surface coverages during this half-period. In general, a log-linear decrease with time was seen. Glow is produced solely via the surface-surface reaction (e33), which has surface adsorbed atomic oxygen and nitric oxide as reactants.

Disparate behavior between species with different thermal desorption times was observed during the shadow half-period. For species with long thermal desorption times, surface coverages decreased slowly during the shadow period. Species with short desorption times exhibited a much greater rate of decrease of coverage during this time. The concentrations of these species on the surface quickly became negligible. With a shorter lifetime on the surface for these species and no flux to replace molecules that desorb, this dramatic decrease is not surprising. In general, atomic species have relatively longer thermal desorption times, and molecular species have shorter desorption times. For the base conditions, nitric oxide is assumed to have a long desorption time.

The analytical analysis of the system of differential equations that describes the surface events showed that the inherent time scale of the system varies inversely with the total incident flux. Thus, at the higher altitudes, where the flux levels are lower, the time scale of the system was found to be longer. As a result, surface coverages were slower to respond to changing conditions at the higher altitudes. A primary example of this was seen in the comparison of the peak rotational coverages and the steady state coverages. At the lower altitudes, the peak rotational coverage was equal to the steady state coverage. At the upper altitudes, the peak coverage failed to reach the steady state value. The time scale of the system of surface events was too long at the upper altitudes to allow the coverage to respond in time to the

increased flux levels as the surface rotated into the incident flow.

A sensitivity study of the glow brightness to the various input parameters was performed. From this analysis, the important precursor events to glow production were determined. The degree of sensitivity of the glow to a particular event varied with altitude. The variation was not significant enough to alter the identification of important events with altitude. In addition to the precursor reactions, the primary glow producing reaction, for forward-looking glow, was determined; reaction (e28) dominated all other reactions during the first half-period of the rotational cycle.

Overall, the calculated glow brightness values showed reasonable agreement with measurements from the Atmosphere Explorer satellite. At the lower altitudes, the calculated brightness overpredicted the experimental brightness by no more than a factor of five. The overprediction was greater at the higher altitudes. It was suggested that the poorer agreement at these altitudes was the result of the relatively high levels of ambient nitric oxide used in the initial conditions. These higher NO concentrations led directly to higher glow brightness. The level of agreement varied with the wavelength of the glow being considered. In general, the 732.0 nm brightness showed better agreement than the 656.3 nm brightness.

The variation of relative brightness with altitude determined from the simulations agreed well with experimental data from on-board Space Shuttle experiments. The experimental measurements themselves exhibited a wide degree of scatter. Uncertainty in the calculated values was due primarily to the lack of knowledge of the ambient nitric oxide concentrations.

10.2 Future Work

Comparisons between the simulations and experimental data have demonstrated that the prescribed solution method is capable of accurately simulating glow production around ram surfaces in low Earth orbit. In discussion of specifics of the method and of the results, numerous uncertainties and assumptions were detailed that limit the accuracy of the method. Further consideration of these limitations identifies areas for concentration of future work. Some of these areas are outlined in this section.

The uncertainty in determining the ambient nitric oxide concentration leads to additional uncertainties throughout the solution procedure. The development of models that can predict the number densities of trace species in the Earth's atmosphere is an area of active research in the atmospheric science community. Using more advanced models as they become available would reduce some of the uncertainties in the calculations. A different profile of NO density with altitude may also result in a more favorable comparison with AE data at the higher altitudes. Furthermore, the ability to accurately measure NO concentrations during flight is an important consideration for future vehicles designed to study space craft glow. While such measurements may not allow for prediction of NO concentrations for future flights, they would allow for a more accurate simulation of the specific flight of the test vehicle. These simulations could focus on other areas of glow production, rather than being concerned with the effect of variations in the assumed free stream NO density.

The DSMC overlay technique was successful in capturing the behavior of the rare species down to a microscopic level. However, the technique has a relatively

high computational cost compared to traditional DSMC simulations. There are two root causes for the increased cost. One, the requirement for two separate simulations to track the common and rare species, respectively. Two, the overhead of storing the large distribution functions that provide a linkage between the two simulations. A refinement of the overlay technique could eliminate both of these causes. The idea would be to run the base and common simulations simultaneously, with separate lists of common and rare particles being tracked in every cell. The concept of a concurrent overlay has a number of advantages. First, only one simulation needs to be performed. While this simulation would take somewhat longer to reach steady state than a traditional simulation, it would likely take less time than the base and overlay simulations used in the present procedure. Second, the velocity and energy distributions would not need to be recorded in every cell. The interaction between the base and overlay simulation would be similar in structure to the current implementation. Instead of creating temporary particles from recorded velocity distributions to collide with overlay particles, particles from the common list in each cell could be used. Third, the use of sample common particles eliminates the error inherent in creating particles from a recorded distribution function. There are a lot of technical details to consider before a concurrent overlay could be implemented. Specifically, the need for source term chemistry in some form would still be required. Regardless, the potential benefits of a concurrent overlay are large enough to strongly suggest investigation into its feasibility.

The surface model implemented considers five basic types of surface phenomena. While the types of events considered are diverse enough to allow for a detailed simulation of the surface coverages, there are additional types of events that may

have a noticeable effect. Specifically, events such as dissociative adsorption could be considered. Additionally, the formulations of the differential models of many of the surface phenomena implicitly assume a surface temperature. Modification to these formulations would allow the effects of surface temperature to be studied directly. Experimental data on temperature effects are available from flights of the Space Shuttle.

The conversion between emitted NO_2^* flux to glow brightness requires a detailed knowledge of the structure of the spectrum of nitrogen dioxide. The complex nature of this spectrum, coupled with the question of exactly how the spectrum shifts with surface-catalyzed reactions, limits the accuracy to which this spectrum is known. It is noted that a more accurate modeling of the spectrum would result in more accurate glow brightness calculations.

The Atmosphere Explorer satellite recorded a difference in glow brightness during the upleg and downleg of elliptical orbits. Simulations that would capture this effect would need to account for the changing atmospheric conditions with time. This suggests that an unsteady DSMC calculation would be required. While a significant undertaking given the complexity of DSMC overlay technique, the upleg/downleg data from the AE satellite does provide more data to which simulation values can be compared.

10.3 Final Thoughts

One of the stated motivations of the present work was a desire to gain a scientific understanding of the complex physics involved in glow production. Through the analysis of the results of the glow production simulation, a number of general trends

were observed and are noted here. The lower altitudes are characterized by a higher density, relatively more collisions and a short inherent time scale of the production events. The short time scale along with increased chemical effects made the results at the lower altitudes less sensitive to variations in the input conditions. Conversely, the upper altitudes had a lower density, almost no collisions and a longer time scale. Consequently glow production was more sensitive to variations in the input parameters at the upper altitudes. Overall, chemistry effects in the flow field had little effect on the structure of the bulk gas in flow field. Again, chemical effects were limited to the rare species. Surface chemistry was dominated by gas-surface reactions when any incident flux was present; surface-surface reactions were only important when there was no incident flux. While this observation may not be surprising, it is not often stated clearly in current literature. Chemical surface events were generally overshadowed by non-reacting physical surface events.

The primary goal of this work was to simulate in detail the processes leading to the production of spacecraft glow. In this regard, the effort has been successful. As discussed in the previous section, there exist portions of the procedure that could be improved. Overall, however, the processes leading to glow production have been simulated in detail. The modeling procedure has been found to be very adaptive to the large variety and number of input parameters. This characteristic is important. Given the large number of uncertainties involved in modeling glow production, the ability to test the sensitivity of the system to variations in the event parameters is essential. The detailed nature of the simulation procedure allows the system to incorporate more accurate input parameters as they become available. This feature is deemed more important than the agreement of a particular set of results with

experimental values. With the large number of input parameters, it is relatively easy to make adjustments to force better agreement. More importantly, the present effort has developed a means by which the glow phenomenon can be effectively studied.

Bibliography

[1] Yee, J. H. and Abreu, V. J., "Visible Glow Induced by Spacecraft-Environment Interaction," *Geophysical Research Letters*, Vol. 10, No. 2, 1983, pp. 126–129.

[2] Murad, E., "The Shuttle Glow Phenomenon," *Annual Review of Physical Chemistry*, Vol. 49, 1998, pp. 73–98.

[3] Swenson, G. R., Leone, A., Holtzclaw, K. W., and Caledonia, G. E., "Spatial and Spectral Characterization of Laboratory Shuttle Glow Simulations," *Journal of Geophysical Research*, Vol. 96, No. A5, 1991, pp. 7603–7612.

[4] Murad, E., "Spacecraft Interaction with Atmospheric Species in Low Earth Orbit," *Journal of Spacecraft and Rockets*, Vol. 33, No. 1, 1996, pp. 131–136.

[5] Yee, J. H., Abreu, V. J., and Dalgarno, A., "The Atmosphere Explorer Optical Glow Near Perigee Altitudes," *Geophysical Research Letters*, Vol. 12, No. 10, 1985, pp. 651–654.

[6] Kofsky, I. L. and Barrett, J. L., "Spacecraft Glows From Surface Catalyzed Reactions," *Planetary Space Science*, Vol. 34, No. 8, 1986, pp. 665–681.

[7] Kitto, A.-M. N. and Harrison, R. M., "Nitrous and Nitric Acid Measurements at Sites in South-East England," *Atmospheric Environment, Part A*, Vol. 26A, No. 2, 1992, pp. 235–241.

[8] Garret, H. B., Chutjian, A., and Gabriel, S., "Space Vehicle Glow and Its Impact on Spacecraft Systems," *Journal of Spacecraft and Rockets*, Vol. 25, No. 5, 1988, pp. 321–340.

[9] Bird, G. A., *Molecular Gas Dynamics and the Direct Simulation of Gas Flows*, Clarendon Press, Oxford, 2nd ed., 1994.

[10] Karipides, D. P., Boyd, I. D., and Caledonia, G. E., "Development of a Monte Carlo Overlay Method with Application of Spacecraft Glow," *Journal of Thermophysics and Heat Transfer*, Vol. 12, No. 1, 1998, pp. 30–37.

[11] Ahmadjian, M. and Jennings, D. E., "Analysis of STS-39 Space Shuttle Glow Measurements," *Journal of Spacecraft and Rockets*, Vol. 32, No. 3, 1995, pp. 507–513.

[12] Swenson, G. R., Rairden, R. L., Jennings, D. E., and Ahmadjian, M., "Vehicle Glow Measurements on the Space Transportation System Flight 62," *Journal of Spacecraft and Rockets*, Vol. 33, No. 2, 1996, pp. 240–249.

[13] Burgess, E. and Torr, D., *Into the Thermosphere: The Atmosphere Explorers*, National Aeronautics and Space Administration, Washington, D.C., 1987.

[14] Dalgarno, A., Hanson, W. B., Spencer, N. W., and Schmerling, E. R., "The Atmosphere Explorer Mission," *Radio Science*, Vol. 8, No. 4, 1973, pp. 263–266.

[15] Hays, P. B., Carignan, G., and Kennedy, B. C., "The Visible-Airglow Experiment on Atmosphere Explorer," *Radio Science*, Vol. 8, No. 4, 1973, pp. 369–377.

[16] Mende, S. B., Swenson, G. R., Geller, S. P., Viereck, R. A., Murad, E., and Pike, C. P., "Limb View Spectrum of the Earth's Airglow," *Journal of Geophysical Research*, Vol. 98, No. A11, 1993, pp. 19,117–19,125.

[17] Pelz, D. T., Reber, C. A., and Hedin, A. E., "A Neutral-Atmosphere Composition Experiment for the Atmosphere Explorer-C, -D and -E," *Radio Science*, Vol. 8, No. 4, 1973, pp. 277–285.

[18] Nier, A. O., Potter, W. E., Hickman, D. R., and Mauersberger, K., "The Open-Source Neutral-Mass Spectrometer on Atmosphere Explorer-C, -D, and -E," *Radio Science*, Vol. 8, No. 4, 1973, pp. 271–276.

[19] Yee, J. H., Abreu, V. J., and Dalgarno, A., "Characteristics of the Spacecraft Optical Glow," *Geophysical Research Letters*, Vol. 11, No. 12, 1984, pp. 1192–1194.

[20] Yee, J. H., Abreu, V. J., Skinner, W. R., and Gu, Z. G., "Optical Glow Observed on Atmosphere Explorer," *Proceedings of the 1991 Vehicle-Enviornment Interactions Conference*, John Hopkins Univesity, Applied Physics Lab, 1991, pp. 76–92.

[21] Yee, J. H., Private Communication, 1996.

[22] Viereck, R. A., Mende, S. B., Murad, E., Swenson, G. R., Pike, C. P., Culbertson, F. L., and Springer, R. C., "Spectral Characteristics of Shuttle Glow," *Geophysical Research Letters*, Vol. 19, No. 12, 1992, pp. 1219–1222.

[23] Swenson, G. and Rairden, R., "Spacecraft Glow, Visible Analysis amd Modeling," AIAA Paper 96-0372, January 1996.

[24] Swenson, G. R., Mende, S. B., and Llewellyn, E. J., "The Effect of Temperature on Shuttle Glow," *Nature*, Vol. 323, No. 9, 1986, pp. 519–522.

[25] Viereck, R. A., Murad, E., Green, B. D., Joshi, P., Pike, C. P., Hieb, R., and Harbaugh, G., "Origin of the Shuttle Glow," *Nature*, Vol. 354, 1991, pp. 48–50.

[26] Levin, D. A., Candler, G. V., Boyd, I. D., Howlett, L. C., and Erdman, P. W., "In-Situ Measurements of Translational and Continuum Flow and UV Radiation from Small Satellite Platforms," AIAA Paper 94-0248, January 1994.

[27] Levin, D. A., Candler, G. V., Collins, R., Erdman, P. W., Zipf, E., Epsy, P., and Howlett, L. C., "Comparison of Theory and Experiment for the Bow Shock Ultraviolet Rocket Flight," *Journal of Thermophysics and Heat Transfer*, Vol. 7, No. 1, 1993, pp. 30–36.

[28] Levin, D. A., Candler, G. V., Collins, R., Erdman, P. W., Zipf, E., and Howlett, L. C., "Examination of Ultraviolet Radiation Theory for Bow Shock Rocket Experiments," *Journal of Thermophysics and Heat Transfer*, Vol. 8, No. 32, 1994, pp. 447–452.

[29] Boyd, I. D., Karipides, D. P., Candler, G. V., and Levin, D. A., "Effect of Dissociation Modeling in Strongly Nonequilibrium Flows at High Altitude," AIAA Paper 95-0709, January 1995.

[30] Caledonia, G. E., Krech, R. H., and Oakes, D. B., "Laboratory Studies of Fast Oxygen Atom Interactions with Materials," *Proceedings of the Sixth International Symposium on Materials in a Space Environment, ESTEC*, Noordwijk, The Netherlands, 1994, pp. 285–290.

[31] Greer, W. A. D., Pratt, N. H., and Stark, J. P. W., "Spacecraft Glows and Laboratory Luminescence: Evidence for a Common Reaction Mechanism," *Geophysical Research Letters*, Vol. 20, No. 8, 1993, pp. 731–734.

[32] Ardebili, M. H. P., Grice, R., Hughes, C. J., and Whitehead, J. C., "Time-Dependent Chemiluminescence from the Surface-Catalysed Recombination of O and NO on Polycrystalline Ni," *Journal of the Chemical Society. Faraday Transactions*, Vol. 87, No. 18, 1991, pp. 2877–2885.

[33] Orient, O. J., Martus, K. E., Chutjian, A., and Murad, E., "Recombination of 5-eV $O(^3P)$ Atoms with Surface-Adsorbed NO: Spectra and Their Dependence

on Surface Material and Temperature," *Physiccl Review A*, Vol. 45, No. 5, 1992, pp. 2998–3003.

[34] Arnold, G. S. and Colemann, D. J., "Surface-Mediated Chemiluminescent Reaction of O and NO," *Chemical Physics Letters*, Vol. 177, No. 3, 1991, pp. 279–282.

[35] Cravens, T. E., Gerard, J.-C., LeCompte, M., Stewart, A. I., and Rusch, D. W., "The Global Distribution of Nitric Oxide in the Thermosphere as Determined by the Atmosphere Explorer D Satellite," *Journal of Geophysical Research*, Vol. 90, No. A10, 1985, pp. 9862–9870.

[36] Stewart, A. I. and Cravens, T. E., "Diurnal and Seasonal Effects in E Region Low-Latitude Nitric Oxide," *Journal of Geophysical Research*, Vol. 83, No. A6, 1978, pp. 2453–2456.

[37] Fuller-Rowell, T. J., "Modeling the Solar Cycle Change in Nitric Oxide in the Thermosphere and Upper Mesosphere," *Journal of Geophysical Research*, Vol. 98, No. A2, 1993, pp. 1559–1570.

[38] Siskind, D. E. and Rusch, D. W., "Nitric Oxide in the Middle to Upper Thermosphere," *Journal of Geophysical Research*, Vol. 97, No. A3, 1992, pp. 3209–3217.

[39] Hedin, A. E., "The Atmospheric Model in the Region 90 to 2000km," *Advances in Space Research*, Vol. 8, No. 5–6, 1988, pp. 9–25.

[40] Wayne, R. P., *Chemistry of Atmospheres*, Claredon Press, Oxford, 2nd ed., 1991.

[41] Torr, D. G. and Torr, M. R., "Chemistry of the Thermosphere and Ionosphere," *Journal of Atmospheric and Terrestrial Physics*, Vol. 41, 1979, pp. 797–839.

[42] Bounsanto, M. J., "A Study of the Daytime E-F_1 Region Ionosphere at Mid-Latitudes," *Journal of Geophysical Research*, Vol. 95, No. A6, 1990, pp. 7735–7747.

[43] Rusch, D. W., Gerard, J.-C., and Fesen, C. G., "The Diurnal Variation of NO, N(^{2}D), and Ions in the Thermosphere: A Comparison of Satellite Measurements to a Model," *Journal of Geophysical Research*, Vol. 96, No. A7, 1991, pp. 11,331–11,339.

[44] Gerard, J.-C., Roble, R. G., Rusch, D. W., and Stewart, A. I., "The Global Distribution of Thermospheric Odd Nitrogen for Solstice Conditions During Solar Cycle Minimum," *Journal of Geophysical Research*, Vol. 89, No. A3, 1984, pp. 1725–1738.

[45] Gerard, J.-C. and Noel, C. E., "AE-D Measurements of the NO Geomagnetic Latitudinal Distribution and Contamination by $N^+(^5S)$ Emission," *Journal of Geophysical Research*, Vol. 91, No. A9, 1986, pp. 10,136–10,140.

[46] Gerard, J.-C., Fesen, C. G., and Rusch, D. W., "Solar Cycle Variation of Thermospheric Nitric Oxide at Solstice," *Journal of Geophysical Research*, Vol. 95, No. A8, 1990, pp. 12,235–12,242.

[47] Barth, C. A., Tobiska, W. K., and Siskind, D. E., "Solar-Terrestrial Coupling: Low-Latitude Thermospheric Nitric Oxide," *Geophysical Research Letters*, Vol. 15, No. 1, 1988, pp. 92–94.

[48] Siskind, D. E., Barth, C. A., and Cleary, D. D., "The Possible Effect of Solar Soft X Rays on Thermospheric Nitric Oxide," *Journal of Geophysical Research*, Vol. 95, No. A4, 1990, pp. 4311–4317.

[49] Siskind, D. E., Stickland, D. J., Meier, R. R., Majeed, T., and Eparvier, F. G., "On the Relationship Between Solar Soft X Ray Flux and Thermospheric Nitric Oxide: An Update with an Improved Photoelectron Model," *Journal of Geophysical Research*, Vol. 100, No. A10, 1995, pp. 19,687–19,694.

[50] Siskind, D. E., Barth, C. A., and Roble, R. G., "The Response of Thermospheric Nitric Oxide to an Auroral Storm 1. Low and Middle Latitudes," *Journal of Geophysical Research*, Vol. 94, No. A12, 1989, pp. 16,885–16,898.

[51] McCoy, R. P., "Thermospheric Odd Nitroden 1. NO, $N(^4S)$, and $O(^3P)$ Densities from Rocket Measurements of the NO δ and γ Bands and the O_2 Herzberg I Bands," *Journal of Geophysical Research*, Vol. 88, No. A4, 1983, pp. 3197–3205.

[52] Eparvier, F. G. and Barth, C. A., "Self-Adsorption Theory Applied to Rocket Measurements of the Nitric Oxide (1, 0) γ Band in the Daytime Thermosphere," *Journal of Geophysical Research*, Vol. 97, No. A9, 1992, pp. 13,723–13,731.

[53] Torr, D. G. and Torr, M. R., "Chemistry of the Thermosphere and Ionosphere," *Journal of Atmospheric and Terrestrial Physics*, Vol. 41, No. 7–8, 1979, pp. 797–839.

[54] Crowley, G., "Dynamics od the Earth's Thermosphere: A Review," Reviews of Geophysics, Supplement, April 1991.

[55] Boyd, I. D. and Gokcen, T., "Computation of Axisymmetric and Ionized Hypersonic Flows Using Particle and Continuum Methods," *American Institute of Aeronautics and Astronautics Journal*, Vol. 32, No. 9, 1994, pp. 1828–1835.

[56] Carlson, A. B. and Hassan, H. A., "Radiation Modeling with Direct Simulation Monte Carlo," *Journal of Thermophysics and Heat Transfer*, Vol. 6, No. 5, 1992, pp. 631–636.

[57] Boyd, I. D., Candler, G. V., and Levin, D. A., "Dissociation Modeling in Low Density Hypersonic Flows of Air," *Physics of Fluids*, Vol. 7, No. 7, 1995, pp. 1757–1763.

[58] VanGilder, D. B., Font, G. I., and Boyd, I. D., "Hybrid Monte Carlo – Particle-in-Cell Simulation of an Ion Thruster Plume," IEPC Paper 97-182, July 1997.

[59] Oh, D. Y., Hastings, D. E., Marrese, C. M., Haas, J. M., and Gallimore, A. D., "Modeling of Stationary Plasma Thruster-100 Thruster Plumes and Implications for Satellite Design," *Journal of Propulsion and Power*, Vol. 15, No. 2, 1999, pp. 345–357.

[60] Hargus, W. A. and Cappelli, M. A., "The Structure of an Expanding Hydrogen Arcjet Plasma," *Physics of Plasmas*, Vol. 5, No. 12, 1998, pp. 4488–4497.

[61] Font, G. I. and Boyd, I. D., "Numerical Study of the Effects of a Reactor Geometry on a Chlorine Plasma Helicon Etch Reactor," *Journal of Vacuum Science & Technology A-Vacuum Surfaces and Films*, Vol. 15, No. 2, 1997, pp. 313–319.

[62] Chen, G., Boyd, I. D., Roadman, S. E., and Engstrom, J. R., "Monte Carlo Analysis of a Hyperthermal Silicon Deposition Process," *Journal of Vacuum Science & Technology A-Vacuum Surfaces and Films*, Vol. 16, No. 2, 1998, pp. 689–699.

[63] Oh, C. K., Oran, E. S., and Cybyk, Z. C., "Microchannel Flow Computed with the DSMC-MLG," AIAA Paper 95-2090, June 1995.

[64] Boyd, I. D., "Conservative Species Weighting Scheme for the Direct Simulation Monte Carlo Method," *Journal of Thermophysics and Heat Transfer*, Vol. 10, No. 4, 1996, pp. 579–585.

[65] Kannenberg, K. C., *Computational Methods for the Direct Simulation Monte Carlo Technique with Application to Plume Impingement*, Ph.D. thesis, Cornell University, Ithaca, New York, 1998.

[66] Dietrich, S. and Boyd, I. D., "Scalar and Parallel Optimized Implementation of the Direct Simulation Monte Carlo Method," *Journal of Computational Physics*, Vol. 126, No. 2, 1996, pp. 328–342.

[67] Baganoff, D. and McDonald, J. D., "A Collision-Selection Rule for a Particle Simulation Method Suited to Vector Computers," *Physics of Fluids*, Vol. 2, No. 7, 1990, pp. 1248–1259.

[68] Koura, K. and Matsumoto, H., "Variable Soft Sphere Molecular-Model for Air Species," *Physics of Fluids*, Vol. 4, No. 5, 1992, pp. 1083–1085.

[69] Meiburg, E., "Comparison of Molecular Dynamics Method and the Direct Simulation Monte Carlo Technique for Flows around Simple Geometries," *Physics of Fluids*, Vol. 29, No. 10, 1986, pp. 3107–3113.

[70] Bird, G. A., "Direct Simulation of High-Vorticity Gas Flows," *Physics of Fluids*, Vol. 30, No. 2, 1986, pp. 364–366.

[71] Boyd, I. D., "Rotational-Translational Energy Transfer in Rarefied Nonequilibrium Flows," *Physics of Fluids A*, Vol. 2, No. 3, 1990, pp. 447–452.

[72] Boyd, I. D., "Analysis of Vibrational-Translational Energy Transfer Using the Direct Simulation Monte Carlo Method," *Physics of Fluids A*, Vol. 3, No. 7, 1991, pp. 1785–1791.

[73] Abe, T., "Inelastic Collision Model for Vibrational-Translational and Vibrational-Vibrational Energy Transfer in the Direct Simulation Monte Carlo Method," *Physics of Fluids*, Vol. 6, No. 9, 1994, pp. 3175–3179.

[74] Boyd, I. D., "A Threshold Line Dissociation Model for the Direct Simulation Monte Carlo Method," *Physics of Fluids*, Vol. 8, No. 5, 1996, pp. 1293–1300.

[75] Gang, C. and Boyd, I. D., "Statistical Error Analysis for the Direct Simulation Monte Carlo Technique," *Journal of Computational Physics*, Vol. 126, No. 2, 1996, pp. 434–448.

[76] Boyd, I. D., Candler, G. V., and Levin, D. A., "Effect of Dissociation Modeling in Strongly Nonequilibrium Flows at High Altitude," AIAA Paper 95-0709, January 1995.

[77] Karipides, D. P., Boyd, I. D., and Levin, D. A., "Prediction of Ultraviolet Emissions in Rarefied Hypersonic Flow," AIAA Paper 95-2091, June 1995.

[78] VanGilder, D. B. and Boyd, I. D., "Particle Simulation of the SPT-100 Plume," AIAA Paper 98-3797, July 1998.

[79] Anderson, J. D., *Hypersonic and High Temperature Gas Dynamics*, McGraw-Hill, New York, 1989.

[80] Hurlbut, F. C., "Particle Surface Interaction in the Orbital Context: A Survey," *Progress in Astronautics and Aeronautics*, edited by E. Muntz, Vol. 116 of *Rarefied Gas Dynamics*, AIAA, Washington, D.C., 1989, pp. 419–450.

[81] Boyd, I. D., Bose, D., and Candler, G. V., "Monte Carlo Modeling of Nitric Oxide Formation Based on Quasi-Classical Trajectory Calculations," *Physics of Fluids*, Vol. 9, No. 4, 1997, pp. 1162–1170.

[82] Dogra, V. K., Collins, R. J., and Levin, D. A., "Modeling of Spacecraft Rarefied Environments Using a Proposed Surface Model," *American Institute of Aeronautics and Astronautics Journal*, Vol. 37, No. 4, 1999, pp. 443–452.

[83] Gorelev, K., Karabadzhak, G., Kireev, A., Nikolsky, V., Plastin, Y., and Yegorov, I., "Modeling of NO, N_2, NO_2 Molecules Band Emission in Shock Layers," TSNIIMASH Contract Report A935-21, 1995.

[84] Sharpe, R. G. and Bowker, M., "The Adsorption and Decomposition of NO on Pd(110)," *Surface Science*, Vol. 360, No. 1–3, 1996, pp. 21–30.

[85] Bowker, M., Guo, Q., and Joyner, R. W., "NO Adsorption on Rh(110)," *Surface Science*, Vol. 257, No. 1–3, 1991, pp. 33–40.

[86] Wartnaby, C. E., Stuck, A., Yeo, Y. Y., and King, D. A., "Microcalorimetric Heats of Adsorption for CO, NO and Oxygen on Pt(110)," *Journal of Physical Chemistry*, Vol. 100, No. 30, 1996, pp. 12,483–12,488.

[87] Luo, M., Zhong, Y., Zhu, B., Yuan, X., and Zheng, X., "Temperature-Programmed Desorption Study of NO and CO_2 over CeO_2 and ZrO_2," *Applied Surface Science*, Vol. 115, No. 2, 1997, pp. 185–189.

[88] Artsyukhovich, A., Ukraintsev, V., and Harrison, I., "Low Temperature Sticking and Desorption Dynamics of Oxygen on Pt(111)," *Surface Science*, Vol. 347, No. 3, 1996, pp. 303–318.

[89] de Mongeot, F. B., Rocca, M., Cupolillo, A., Valbusa, U., Kreuzer, H. J., and Payne, S. H., "Sticking and Thermal Desorption of O_2 on Ag(001)," *Journal of Chemical Physics*, Vol. 106, No. 2, 1997, pp. 711–718.

[90] Butler, D. A., Sanders, J. B., Raukema, A., Kleyn, A. W., and Frenken, J. W. M., "Oxygen Dissociation on Ag(110): a Ruin Game," *Surface Science*, Vol. 375, No. 2–3, 1997, pp. 141–149.

[91] Pazzi, V. I. and Tantardini, G. F., "Dynamical Simulations of the Oxygen Adsorption on the Ag(110) Surface," *Journal of Molecular Catalysis, A: Chemical*, Vol. 119, No. 1–3, 1996, pp. 289–297.

[92] Pazzi, V. I. and Tantardini, G. F., "Dynamics of Oxygen Adsorption on Ag(110): Surface Motion Effects," *Surface Science*, Vol. 337–379, No. 1–3, 1996, pp. 572–577.

[93] Sjovall, P. and Uvdal, P., "Oxygen Sticking on Pd(111): Double Precursors, Corrigation and Substrate Temperature Effects," *Chemical Physics Letters*, Vol. 282, No. 5–6, 1998, pp. 355–360.

[94] He, J.-W. and Norton, P., "Thermal Desorption of Oxygen From a Pd(110) Surface," *Surface Science*, Vol. 204, No. 1–2, 1988, pp. 26–34.

[95] Dietrich, H., Geng, P., Jacobi, K., and Ertl, G., "Sticking Coefficient for Dissociative Adsorption of N_2 on Ru Single-Crystal Surfaces," *Journal of Chemical Physics*, Vol. 104, No. 1, 1996, pp. 375–381.

[96] Press, W. H., Teukolsky, S. A., Vetterling, W. T., and Flannery, B. P., *Numerical Recipes in FORTRAN*, Cambridge University Press, Cambridge, 2nd ed., 1992.

[97] Arfken, G., *Mathematical Methods for Physicists*, Academic Press, San Diego, 3rd ed., 1985.

[98] Pattern, K. O., Burley, J. D., and Johnston, H. S., "Radiative Lifetimes of Nitrogen-Dioxide for Excitation Wavelengths from 400nm to 750nm," *Journal of Physical Chemistry*, Vol. 94, No. 20, 1990, pp. 7960–7969.

[99] Yee, J. H. and Dalgarno, A., "Radiative Lifetime Analysis of Shuttle Optical Glow," *Journal of Spacecraft and Rockets*, Vol. 23, No. 6, 1986, pp. 635–640.

[100] Caledonia, G. E., Holtzclaw, K. W., Krech, R. H., and Sonnenfroh, D. M., "Mechanistic Investigations of Shuttle Glow," *Journal of Geophysical Research*, Vol. 98, No. A3, 1993, pp. 3725–3730.

[101] Chu, A.-L., Reeves, R. R., and Halstead, J. A., "Surface-Catalyzed Formation of Electronically Excited Nitrogen Dioxide and Oxygen," *Journal of Physical Chemistry*, Vol. 90, No. 3, 1986, pp. 466–471.

[102] Kenner, R. D. and Ogryzlo, E. A., "Orange Chemiluminescence from NO_2," *Journal of Chemical Physics*, Vol. 80, No. 1, 1984, pp. 1–6.

[103] Upschulte, B. L., Oakes, D. B., Caledonia, G. E., and Blumberg, W. A. M., "Infared Emissions Arising from the Reactions of Fast O/O^+ with N_2," *Geophysical Research Letters*, Vol. 19, No. 10, 1992, pp. 993–996.

[104] Peraire, J., Vahdati, M., Morgan, K., and Zienkiewicz, O. C., "Adaptive Remeshing for Compressible Flow Computations," *Journal of Computational Physics*, Vol. 72, No. 2, 1987, pp. 449–466.

[105] Dietrich, S. and Boyd, I. D., "Scalar and Parallel Optimized Implementation of the Direct Simulation Monte Carlo Method," *Journal of Computational Physics*, Vol. 126, No. 2, 1996, pp. 328–342.